High-Precision Automotive Radar Target Simulation

Zur Erlangung des akademischen Grades eines

DOKTORS DER INGENIEURWISSENSCHAFTEN (Dr.-Ing.)

von der KIT-Fakultät für Elektrotechnik und Informationstechnik des Karlsruher Instituts für Technologie (KIT)

angenommene

DISSERTATION

von

M.Sc. Axel Diewald

Tag der mündlichen Prüfung: 09.03.2023

Hauptreferent: Prof. Dr.-Ing. Dr. h.c. Thomas Zwick
Korreferent: Prof. Dr.-Ing. Thomas Walter

Zusammenfassung

Automobil-Radarsensoren spielen eine wichtige Rolle bei der aktuellen Entwicklung des autonomen Fahrens. Ihre Fähigkeit, Objekte auch unter widrigen Witterungsverhältnisse zu erkennen, macht sie unverzichtbar für die Umgebungserfassung in autonomen Fahrzeugen. Da ihre Funktionalität direkt am Einsatzort validiert werden muss, ist ein vollständig integriertes Testsystem erforderlich. Radarzielsimulatoren (RZS) haben in letzter Zeit sowohl in der Forschung als auch im kommerziellen Bereich viel Aufmerksamkeit erregt. Sie sind in der Lage, ein zu prüfendes Radargerät zu täuschen, indem sie eine künstliche Umgebung erschaffen, die aus virtuellen Radarzielen besteht. Dazu empfängt ein RZS das vom zu testenden Radar ausgestrahlte Signal, modifiziert es im Hinblick auf die gewünschten Zieleigenschaften und sendet es zurück an das Radar. Damit diese virtuelle Umgebung so glaubwürdig und realistisch wie möglich ist, müssen die virtuellen Radarziele hinsichtlich ihrer Eigenschaften möglichst präzise erzeugt werden.

Die meisten atuellen RZS simulieren die Winkelposition eines virtuellen Ziels durch Multiplexen des künstlichen Radarechos zwischen mehreren lateral verteilten Antennen. Dies ermöglicht jedoch nur Ziele an diskreten Winkelpositionen zu simulieren und führt zwangsläufig zu nicht vernachlässigbaren Diskrepanzen zwischen Soll- und Ist-Winkel. In dieser Arbeit wird eine neue Methodik vorgestellt, die es ermöglicht, virtuelle Ziele an beliebiger Winkelposition zu simulieren, indem die künstlichen Radarechos benachbarter RZS-Antennen überlagert werden. Dies ermöglicht nicht nur die durchgehende Simulation von lateral bewegten Zielen, sondern reduziert auch den auftretenden Winkelfehler drastisch.

Die Entfernung eines virtuellen Ziels wird simuliert, indem das eintreffende Radarsignal künstlich verzögert wird. Aufgrund der internen Architektur derzeitiger RZS kann diese Verzögerung und damit auch die Zielentfernung nur in bestimmten Schrittweiten eingestellt werden. In dieser Arbeit wird eine weitere neue Methodik vorgestellt, die eine stufenlose Einstellung der

Verzögerung und damit einhergehend die Simulation von virtuellen Zielen in beliebiger Entfernung ermöglicht. Damit lassen sich sehr kleine Entfernungsänderungen und somit sogar die Bewegung virtueller Ziele innerhalb des Messzyklus eines Radars simulieren, so dass auch nicht-ideale Ziele mit realistischen Eigenschaften wie Entfernungs- und Geschwindigkeitsmigration erzeugt werden können.

Abstract

Automotive radar sensors play a major role in the current development of autonomous driving. Their ability to detect objects even under adverse weather conditions makes them indispensable for environment-sensing tasks in autonomous vehicles. Since their functional operation must be validated in-place, a fully integrated test system is required. Radar target simulators (RTSs) have recently drawn a lot of attention both in research and in the commercial sector. They deceive a radar under test (RuT) by creating an artificial environment consisting of virtual radar targets. To achieve this, an RTS system receives the radar signal emitted by the RuT, modifies it with regard to the intended target characteristics and re-transmits it towards the RuT. In order for this environment to be as credible and realistic as possible, the virtual radar targets must be generated as accurate as possible with regard to their characteristics.

In most current RTS systems, the angle of arrival (AoA) of a virtual target is simulated by multiplexing the artificial radar echo between multiple laterally distributed RTS front ends (FEs). However, this only allows the simulation of virtual targets at discrete angular positions and inevitably leads to non-negligible discrepancies between set and detected AoA. In this work, a new technique is presented that enables virtual targets to be simulated at an arbitrary AoA by superimposing the artificial radar echoes of adjacent FEs. It not only permits the continuous simulation of lateral moving targets, but also drastically reduces the occurring angular error.

The range of a virtual target is simulated by applying an artificial delay to the incoming radar signal before re-transmission. Due to the internal architecture of current RTS systems, the delay and thus also the target range can only be set in certain increments. In this work, yet another new technique is presented, which enables a seamless adjustment of the delay and the simulation of virtual targets at arbitrary range. This allows to simulate very small range changes and thus even the movement of virtual targets within the measurement cycle of a radar

enabling the creation of non-ideal targets that feature realistic characteristics such as range and Doppler migration.

Acknowledgement

This thesis was written during my time as a research associate at the Institute of Radio Frequency Engineering and Electronics (IHE) at the Karlsruhe Institute of Technology (KIT).

First of all, I would like to thank Prof. Dr.-Ing. Dr. h.c. Thomas Zwick not only for giving me the opportunity to write this thesis, but also granting me the scientific freedom and encouragement to follow my own ideas. I would like to extend my sincere thanks to Prof. Dr.-Ing. Thomas Walter for his interest in my work and for willingly accepting the co-lecture.

I would like to express my deepest appreciation to Dr.-Ing. Benjamin Nuß who supervised and guided my scientific work from the very beginning. I would like to truly thank him for his openness to all my questions and his invaluable support. I am grateful to Georg Gramlich, with whom I had the pleasure of sharing an office and the duties of Erasmus coordinator. I would also like to thank Sören Marahrens, Christian Bohn and Alexander Quint for the jointly supervision of the Student Innovation Lab and the *Grundlagen der Hochfrequenztechnik* lecture. Many thanks go to Theresa Antes and Johannes Galinsky, who contributed significantly to this work with their master theses and proofread the manuscript. Furthermore, I would like to thank Thomas Henauer, Marius Kretschmann and Daniel Gil Gaviria for sharing the same interests and leisure activities, and providing the necessary distraction. In general, I would like to express my sincere gratitude to all my colleagues for making my time at the institute so very enjoyable and memorable.

My very special and personal thanks go to my parents, my brothers and my friends, who supported me unconditionally over the past three decades. Above all, I would like to thank Katrin Mohr for being the person she is and for simply everything.

Karlsruhe, August 2022
Axel Diewald

Table of Contents

Abbrevations and Variables

Abbrevations

ADAS	Advanced driver assistance systems
ADC	Analog-to-digital converter
AXI	Advanced eXtensible Interface
AoA	Angle of arrival
BAW	Bulk acoustic wave
BRAM	Block Random-Access Memory
DAC	Digital-to-analog converter
DDC	Digital down-converter
DDR	Double Data Rate
DDS	Direct digital synthesis
DSP	Digital signal processor
DUC	Digital up-converter
FE	Front end
FF	Flip-flop
FFT	Fast Fourier transform
FIFO	First-in-first-out

FIR	Finite impulse response
FMCW	Frequency-Modulated Continuous Wave
FoV	Field of view
FPGA	Field programmable gate array
HIL	Hardware-in-the-Loop
IF	Intermediate frequency
IHP	Leibniz Institute for High Performance Microelectronics
IQ	In-phase and quadrature
LNA	Low-noise amplifier
LO	Local oscillator
LPF	Low-pass filter
LUT	Lookup table
lwIP	lightweight Internet Protocol
MIL	Model-in-the-Loop
MIMO	Multiple-input multiple-output
MMIC	Monolithic microwave integrated circuit
PA	Power amplifier
PCB	Printed circuit board
PL	Programmable logic
PLL	Phased-locked loop
PS	Processing system
RAM	Random-Access Memory

RCS	Radar cross section
RFSoC	Radio frequency system on chip
RTS	Radar target simulator
RuT	Radar under test
SAR	Synthetic-aperture radar
SAW	Surface acoustic wave
SIL	Software-in-the-Loop
SMA	SubMiniature version A
SMD	Surface mount device
SNR	Signal-to-noise ratio
SP	Superposition
TCP	Transmission Control Protocol
UDP	User Datagram Protocol
VCO	Voltage-controlled oscillator
VGA	Variable gain amplifier
VIL	Vehicle-in-the-Loop
VuT	Vehicle under test
VVE	Virtual vehicle environment

Constants

$c_0 = 299\,792\,458\,\mathrm{m/s}$	Speed of light
$e = 2.71828\ldots$	Euler's number
$\mathrm{j} = \sqrt{-1}$	Imaginary unit
$\pi = 3.14159\ldots$	Pi

Latin Symbols and Variables

Lower Case Letters

b_{1D}	One-dimensional beamsteering vector
b_{2D}	Two-dimensional beamsteering vector
d_A	Virtual antenna array element spacing
d_{rx}	Receive antenna element spacing
d_{tx}	Transmit antenna element spacing
f_A	Spatial frequency
f_{bb}	Baseband frequency
f_{cr}	Carrier frequency
f_D	Doppler frequency
f_{lo}	Local oscillator frequency
f_{rts}	RTS carrier frequency
$f_{s,rts}$	RTS sample frequency
f_{rx}	Receive signal frequency
f_s	Sampling frequency
f_{tx}	Transmit signal frequency
k	Range-FFT index
m	Doppler-FFT index

n_{A}	Antenna element index
n_{c}	Chirp index
n_{rts}	RTS sample index
n_{rx}	Receive antenna index
n_{s}	Sample index
n_{tx}	Transmit antenna index
p	Virtual antenna position
p_{az}	Antenna azimuth position
p_{el}	Antenna elevation position
s_{b}	Beat signal
q	RTS channel index
s_{D}	Signal after Doppler estimation
s_{R}	Signal after range estimation
s_{rx}	Receive signal
s_{tx}	Transmit signal
t	Time
v	Target velocity
v_{sim}	Simulated target velocity
x	Input signal
y	Output signal

Upper Case Letters

A_q	RTS attenuation
A_{W}	Effective antenna aperture
B	Bandwidth
DR	Dynamic range
G_{fe}	RTS FE antenna gain
G_{rts}	Simulated signal gain

N_A	Number of virtual antenna elements
N_c	Number of chirps
N_{rx}	Number of receive antennas
N_s	Number of samples
N_{tx}	Number of transmit antennas
P_{rx}	Radar receive power
R	Target range
R_0	Initial target range
R_c	Physical distance between RTS FEs and RuT
R_{sim}	Simulated target range
T_c	Chirp repetition time
T_m	Measurement time
T_s	Chirp time
S_{tx}	Transmit power density

Greek Symbols and Variables

α	Azimuth angle
β	Elevation angle
θ	Target azimuth angle
θ_{rx}	RTS receiver azimuth angle
θ_{tx}	RTS transmitter azimuth angle
λ	Wavelength at carrier frequency
η_{rts}	RTS sample delay
τ	Signal delay
τ_0	Initial signal delay
τ_{c}	Free space signal delay
τ_{rts}	RTS internal signal delay
φ_{A}	Signal phase after AoA estimation
φ_{b}	Beat signal phase
φ_{rx}	Receive signal phase
φ_{tx}	Transmit signal phase
Φ	Random phase offset
σ	Target radar cross section
σ_{sim}	Simulated target radar cross section
ψ	Target elevation angle
ψ_{rx}	RTS receiver elevation angle
ψ_{tx}	RTS transmitter elevation angle

1 Introduction

1.1 Motivation

In recent years, the development of advanced driver assistance systems (ADASs) and autonomous driving has reached new levels of sophistication. ADASs use environment-sensing technologies such as camera, ultrasound, light detection and ranging (lidar) and radio detection and ranging (radar) to monitor the surroundings of the vehicle, detect possible obstacles nearby and react accordingly. In order to ensure proper operation and thus the safety of all traffic participants involved, autonomous driving functions and the sensors on which they rely must be validated thoroughly. Due to their weather robustness and long-range capability, radar sensors play a key role in a large share of such systems, and must be tested in particular.

The validation procedure is divided into multiple successive stages and carried out in parallel with the development process. During the design and concept phase, the radar sensor is verified using so-called Model-in-the-Loop (MIL) tests; later in the implementation phase, Software-in-the-Loop (SIL) and Hardware-in-the-Loop (HIL) tests are employed [FKJ+19]. Finally, during the integration phase, field tests are conducted on the road, where the sensor and ADAS function are deployed in the vehicle. These field tests are highly labor-intensive and require a great deal of effort, as distances in the order of several million kilometers must be covered in order to ensure the proper functioning of the system [KP16, MGLW15, Sch17b, KW16]. Moreover, these tests are not repeatable, since real-world traffic scenarios are unique, and thus they must be reiterated whenever the system undergoes any design changes.

For this reason, there have been attempts to find test solutions that complement road tests and thereby reduce the amount of work required. Virtual vehicle environment (VVE) simulations emulate a digital clone of the car and are able to replicate entire traffic scenarios, including the physical

and electromagnetic behavior of the vehicle itself as well as its surroundings [FFFG20, DWCP21, SRGD21]. The propagation, reflection and diffraction of the electromagnetic waves emitted by the virtual radar sensor are simulated using ray tracing technology [AHHD20, Sei21]. Although this methodology represents an unprecedented level of accuracy in virtualized testing, it is nonetheless based on software models that can only to a certain degree mimic the exact behavior and interactions of real-world components such as antenna array and bumper. Hence, sheer software simulations are not realistic enough and cannot be used solely for the validation of safety-relevant driving functions.

As a consequence, a new testing paradigm is on the rise: Vehicle-in-the-Loop (VIL) testing [WHLS19, GMS+18, WMN+20, AVL22]. It enables thorough integrative validation of ADAS functions in a controllable laboratory environment. As can be deducted from the name, the car is tested as a whole, for which a vehicle under test (VuT) is mounted on a roller dynamometer or power train test bench that is connected to a VVE simulation [DKK+21]. The torque, steering, pitch and roll forces to which the digital car clone is subjected in the simulation are applied to the VuT on the test bench through electric motors, and its behavioral response is fed back into the VVE simulation.

In addition to the mechanical-dynamic components, the various sensors of the vehicle, including the radar, must also be stimulated and tested. This is one of the reasons why radar target simulator (RTS) systems have recently drawn a lot of attention, both in research and the commercial sector, as they are able to deceive a radar under test (RuT) by creating an artificial environment consisting of virtual radar targets. To accomplish this task, RTS systems receive the radar signal emitted by the RuT and send back a modified version of it. The modifications correspond to the virtual target characteristics that are to be simulated, namely range, velocity, radar cross section (RCS) and angle of arrival (AoA). They are realized by applying a delay, Doppler frequency shift and attenuation to the return signal and controlling the angular position from where it is re-transmitted. The basic idea of integrated radar target simulation is illustrated in Fig. 1.1.

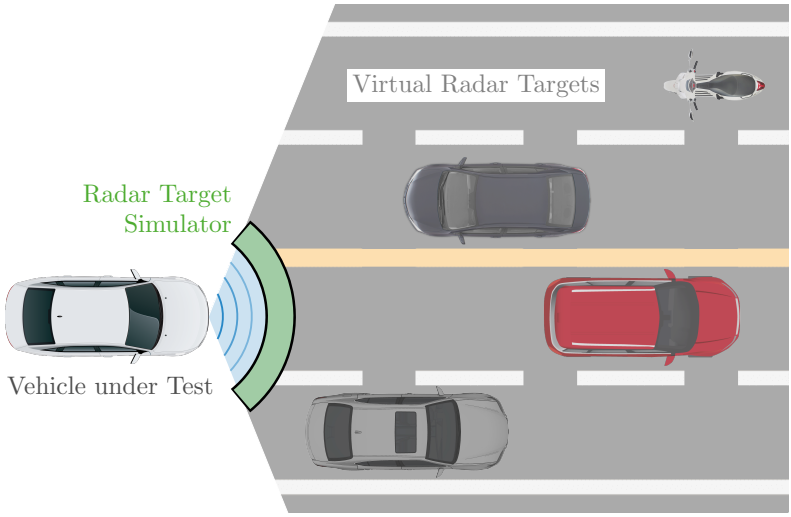

Figure 1.1: Operating principle of integrated RTS-VIL testing

1.2 State of the Art

As a matter of fact, RTSs have been around for some time, but have mainly been used in other applications, especially in end-of-line testing as part of the quality assurance process of radar sensor manufacturers [Roh21a, Key17, dSP20, Kon17b, Ros16]. In this context, RTS systems support the calibration and functional verification of the sensor after its final assembly and are only required to create a single digit number of virtual targets. As the focus now shifts towards ADAS validation and VIL testing, the demands on RTSs increase drastically as they must now be able to simulate complex traffic scenarios that comprise a multitude of radar targets.

There have been numerous approaches to design multi-target RTS systems, using different methods to create the virtual radar targets. The artificial radar echo can be generated either by applying a true-time delay [GGS+17, EPB16, LEWW14] or a frequency shift [SSGW21, RH20, RISW22] to the incoming transmit signal from the RuT, or analyzing & re-synthesizing it [DMW18, WMN+20]. In addition, the realization of the selected method can

be done using either an analog [EPB16, GGS+17, SJM+21, IMSW19] or digital implementation topology [SN20, WMN+20, SP21, JLH21]. It turns out that neither implementation concept, analog or digital, is clearly superior to the other, as they both have their advantages and disadvantages. The same applies to the target generation method, whose selection in combination with the implementation topology has major implications on the capabilities and performance of the RTS system.

Creating virtual radar targets with the frequency shift or analysis & re-synthesis method is only applicable to radar sensors that employ a chirp sequence modulation scheme and it requires prior knowledge of the exact waveform parameters of the transmit signal. This presents an issue because firstly, this kind of information can only be obtained by extraction, as it is not made publicly available by the manufacturers, and secondly, because future radars sensors will potentially employ all-digital modulation schemes [GdONA+22, WS14, SGR+21]. Therefore, it can be concluded that only the true-time delay target generation method meets the requirements of future-proof RTS systems capable of validating autonomous driving functions.

Analog RTS systems that utilize the true-time delay method are able to create virtual targets in close vicinity to the RuT, but are restricted in their scalability, since the generation of each virtual target is assigned to its individual signal path within the RTS, which in turn is implemented using dedicated hardware components. Evidently, this circumstance prevents any reconfiguration of the system at run-time or even post-production and permits the generation of only a predefined and limited number of targets. In contrast, digital RTS systems are highly flexible due to the reprogrammability of their target generation unit and can create a large number of virtual targets. Nevertheless, due to inevitable signal delays caused by the conversion to and from the digital domain, the minimum simulatable range of a virtual target generated by a digital RTS system cannot fall below a certain limit, usually of the order of 20 to 30 m. In order to combine the benefits of both implementation topologies, a hybrid system can be proposed that splits the incoming radar signal and feeds it into an analog and digital RTS in parallel [GSG+18]. Subsequent to the signal modifications of the respective target generation units, the signal can be recombined and transmitted back to the RuT. More detailed deliberations concerning the implementation topologies and the target generation methods can be found in chapter 3.

The simulation of the angular position of the virtual target is performed independently of the previous remarks. The angle from which the artificial radar echo is sent back to the RuT is controlled by multiplexing between multiple spatially distributed RTS front ends (FEs) that are arranged in a semi-circular formation around the RuT.

1.3 Objectives and Structure of the Work

The objective of this work is to design and implement an RTS system that is capable of performing sophisticated ADAS validation tests. For this, it must not only be able to simulate complex traffic scenarios that consist of a multitude of radar targets, but also be compatible with current and upcoming commercial radar sensors. As the validation tests are to be carried out integratively and in-place, the sensors and their debug interfaces cannot be probed, and no prior knowledge of the waveform can be assumed. The system should work with all popular modulation schemes and be able to simulate virtual targets that can be controlled independently in range, velocity, RCS and AoA. Based on these requirements and the previously mentioned considerations, a digital system topology and a true-time delay target generation approach were chosen. This represents the only solution that not only covers all modulation types, but also enables a flexible simulation of a large number of virtual targets.

As mentioned before, the AoA of virtual targets is simulated by multiplexing the artificial radar echo between lateral distributed RTS FEs, which only allows for targets at discrete angular positions, inevitably leading to non-negligible deviations between set-point and actual AoA. Given the long range capability of modern radar sensors, even small angular errors can lead to a preceding vehicle being detected in the wrong lane, which can have severe consequences for the vehicle occupants. Hence, an RTS system for ADAS validation must be designed to minimize the angular error, which is why in this work a new technique is presented that enables the generation of virtual radar targets at an arbitrary AoA. The basic concept is to superimpose the artificial radar echoes of adjacent RTS FEs and control the AoA with the amplitude attenuations of the corresponding echoes. This allows to reduce the number of RTS channels required and thereby cuts the hardware cost, while at the same time drastically decreases the angular error and increases the accuracy with which the

virtual targets are created. This new technique overcomes the rasterization and discontinuity limitations of the angle simulation when using distributed FEs.

A similar rasterization applies to the delay that is applied to the incoming radar signal. In the digital domain, a true-time delay is induced by buffering the incoming samples for a specified number of clock cycles, before they are passed on. Since only an integer number of samples can be buffered, the resulting signal delay and thus also the target range can only be adjusted in certain increments. This determines the range accuracy of the RTS, which must satisfy not only the range resolution capability of modern radar sensors, that are on the verge to be improved using greater bandwidths, but also the even finer range accuracy of the sensors. In this work, yet another new technique is presented, which enables a stepless adjustment of the delay so that virtual targets can be created at arbitrary range without the restrictions of a rasterization. The application of a gridless signal delay is made possible using all-pass fractional delay filters whose group delay can be controlled via the filter coefficients. This technique also bears the potential to simulate the movement of virtual targets within the measurement cycle of a radar allowing to create non-ideal targets that feature realistic characteristics such as range and Doppler migration.

In the following, first the radar fundamentals are explained that are necessary for the comprehension of the subsequent elaborations. Next, an overview of the state of the art of radar target simulation is given, before the RTS system that was built in the course of this work is presented. Thereupon, the two newly developed techniques are discussed that overcome the rasterization of range and angle, thus enabling the simulation of virtual radar targets at arbitrary positions. Finally, a conclusion that summarizes the achievements of this work is given.

2 Radar Principles

This chapter addresses the theoretical fundamentals of radar technology including the analog and digital signal processing, which are necessary for the comprehension of the following chapters. First, the universal radar range equation is derived before subsequently the generic signal model of a chirp sequence radar is developed. Next, the digital signal processing steps which enable the estimation of the range, velocity and angle of arrival (AoA) of a radar target are elaborated. In the end, analytical remarks concerning the resolution and unambiguous measurement region of a radar are given.

2.1 Radar Range Equation

In order to detect an object with a monostatic radar system, a signal with the power of P_{tx} is radiated from a transmitter via an antenna with the antenna gain G. At the distance R from the antenna the power density is therefore

$$S_{\mathrm{tx}} = \frac{P_{\mathrm{tx}} G}{(4\pi) R^2} \tag{2.1}$$

The object located at the distance R from the radar sensor reflects the impinging electromagnetic wave according to its radar cross section (RCS) σ [Sko90]. The signal travels back to the sensor, where it is received by the radar with its effective antenna aperture of

$$A_{\mathrm{W}} = \frac{G \lambda^2}{4\pi} \tag{2.2}$$

resulting in the receive power at the receiver of the radar of [Gö11]

$$P_{\mathrm{rx}} = \frac{P_{\mathrm{tx}} G^2 \sigma \lambda^2}{(4\pi)^3 R^4} \tag{2.3}$$

The equation is only applicable if the far-field condition is met [Lud13].

2.2 Chirp Sequence Radar

Although the RTS system implemented as well as the methods presented in the course of this work are not limited to a specific radar modulation scheme, the subsequent analytical descriptions in this work are based on a chirp sequence radar since it represents the current de facto standard in automotive radar applications [Rob22, Con21].

The radar transmits a continuous signal, consisting of multiple chirps, each of which has a linear frequency slope. The signal propagates through free space, is reflected by a potentially dynamic target and returns to the sensor with a time shift τ. Thereupon, it is mixed with the transmit signal to form the so-called beat signal, which is subsequently low-pass filtered and discretized. The range of the target can be estimated by determining the frequency of the beat signal

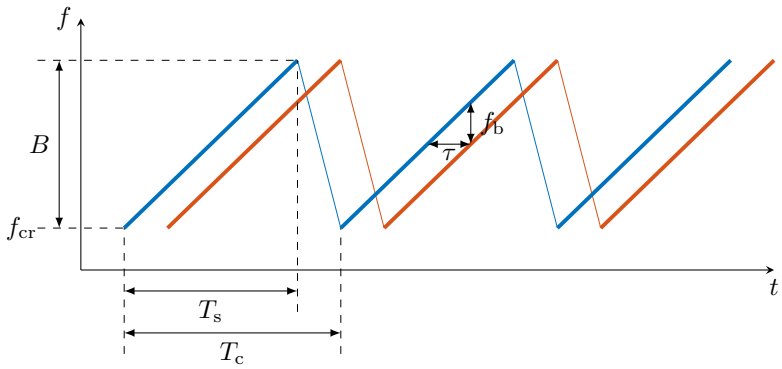

Figure 2.1: Chirp sequence radar transmit (blue) and receive (red) signal

which corresponds to the difference of the instantaneous frequencies between the transmit and receive signal and hence to the time delay. The potential velocity of the target can be estimated by analyzing the relative phase shift among the chirps. More detailed explanations concerning the radar signal processing can be found in 2.3. An illustration of the transmit and receive signal of a chirp sequence radar can be seen in Fig. 2.1.

2.2.1 Signal Model

In the following, the signal model of a chirp sequence radar sensor is developed. The model is kept generic and will be extended in the subsequent chapter for the respective applications. For the sake of simplicity and clarity, it focuses primarily on the signal phase in order to facilitate the comprehension of the approaches developed in chapter 5 and 6 and their limitations.

The radar sensor transmits a chirp signal whose frequency increases linearly over time and can be described by

$$f_{\mathrm{tx}}(t) = f_{\mathrm{cr}} + \frac{B}{T_{\mathrm{s}}} \cdot t \ , \qquad t \in [0, T_{\mathrm{s}}] \tag{2.4}$$

where f_{cr} denotes the start frequency of the chirp, B the bandwidth and T_{s} the duration of the chirp. The phase of the signal can by derived by forming the integral over the signal frequency

$$\varphi_{\mathrm{tx}}(t) = 2\pi \int_0^t f(t') \cdot dt' = 2\pi \left[f_{\mathrm{cr}} \cdot t + \frac{B}{2T_{\mathrm{s}}} \cdot t^2 \right] \tag{2.5}$$

which ultimately enables the deduction of the time signal

$$s_{\mathrm{tx}}(t) = \exp\left\{ \mathrm{j}\varphi_{\mathrm{tx}}(t) \right\} = \exp\left\{ \mathrm{j}2\pi \left[f_{\mathrm{cr}} \cdot t + \frac{B}{2T_{\mathrm{s}}} \cdot t^2 \right] \right\} \tag{2.6}$$

neglecting the amplitude. For a single measurement, the radar transmits N_c chirps, whose phase and corresponding signal can be expressed as

$$\varphi_\mathrm{tx}(t, n_\mathrm{c}) = 2\pi \left[f_\mathrm{cr} \cdot t + \frac{B}{2T_\mathrm{s}} \cdot t^2 \right] + \Phi(n_\mathrm{c}) \,, \qquad n_\mathrm{c} \in [0, N_\mathrm{c} - 1] \tag{2.7}$$

$$s_\mathrm{tx}(t, n_\mathrm{c}) = \exp\left\{ \mathrm{j}\varphi_\mathrm{tx}(t, n_\mathrm{c}) \right\} = \exp\left\{ \mathrm{j}2\pi \left[f_\mathrm{cr} \cdot t + \frac{B}{2T_\mathrm{s}} \cdot t^2 \right] + \Phi(n_\mathrm{c}) \right\} \tag{2.8}$$

$\Phi(n_\mathrm{c})$ describes the random start phase of the chirp which is caused by resetting the frequency back to f_cr in between the chirps. As stated before, the receive signal and its phase can be described as a time shifted version of the transmit counterparts

$$s_\mathrm{rx}(t, n_\mathrm{c}) = s_\mathrm{tx}(t - \tau, n_\mathrm{c}) \tag{2.9}$$

$$\varphi_\mathrm{rx}(t, n_\mathrm{c}) = \varphi_\mathrm{tx}(t - \tau, n_\mathrm{c}) \tag{2.10}$$

The mixing of the transmit and receive signal, i.e. the de-chirping, can be expressed either as the multiplication of the transmit signal with the complex conjugate of the receive signal

$$\begin{aligned} s_\mathrm{b}(t) &= s_\mathrm{tx}(t, n_\mathrm{c}) \cdot {s_\mathrm{rx}}^*(t, n_\mathrm{c}) \\ &= \exp\left\{ \mathrm{j}2\pi \left[f_\mathrm{cr}\tau + \frac{B}{2T_\mathrm{s}} \left(2\tau \cdot t - \tau^2 \right) \right] \right\} \end{aligned} \tag{2.11}$$

or as the difference of their respective phases

$$\begin{aligned} \varphi_\mathrm{b}(t) &= \varphi_\mathrm{tx}(t, n_\mathrm{c}) - \varphi_\mathrm{rx}(t, n_\mathrm{c}) \\ &= 2\pi \left[f_\mathrm{cr}\tau + \frac{B}{2T_\mathrm{s}} \left(2\tau \cdot t - \tau^2 \right) \right] \end{aligned} \tag{2.12}$$

The instantaneous range of a target which is initially located at a distance of R_0 and features a radial velocity of v throughout a radar measurement can be expressed as

$$R = R_0 + v(t + n_\mathrm{c} T_\mathrm{c}) \tag{2.13}$$

where T_c denotes the chirp repetition period. Thus, the resulting instantaneous delay of the receive signal can be described by

$$\tau = \frac{2R}{c_0} = \tau_0 + \frac{2v(t + n_c T_c)}{c_0} \tag{2.14}$$

where τ_0 represents the initial signal delay. Substituting the delay in (2.12) yields the beat signal phase of a dynamic target of

$$\begin{aligned}\varphi_b(t, n_c) = 2\pi \Bigg[& \underbrace{\left(\frac{B}{T_s} \tau_0 \left(1 - \frac{2v}{c_0}\right) + \overbrace{f_{cr} \frac{2v}{c_0}}^{\text{Range-Doppler coupling}} \right) \cdot t}_{\text{Range estimation}} + \underbrace{\left(\frac{2v}{c_0} \left(f_{cr} - \frac{B}{T_s} \tau_0 \right) \right) \cdot n_c T_c}_{\text{Velocity estimation}} \\ & + \left(\frac{B}{T_s} \frac{2v}{c_0} \left(1 - \frac{v}{c_0}\right) \right) \cdot t^2 - \left(\frac{B}{T_s} \frac{2v^2}{c_0^2} \right) \cdot (n_c T_c)^2 \\ & + \underbrace{\left(\frac{B}{T_s} \frac{2v}{c_0} \left(1 - \frac{2v}{c_0}\right) \right) \cdot t \cdot n_c T_c}_{\text{Range-Doppler migration}} + \underbrace{\tau_0 \left(f_{cr} - \frac{B}{2T_s} \tau_0 \right)}_{\text{Angle of arrival estimation}} \Bigg]\end{aligned} \tag{2.15}$$

The first term has a linearly increasing phase along time t, whose slope mainly depends on the initial time delay τ_0 of the associated target. This can be used in the next step to estimate the range of the object. The term also incorporates a share that is proportional to the velocity of the target. This part is known as range-Doppler coupling and leads to a small error in the range estimation caused by a dynamic object, which can be compensated after the Doppler estimation. The second term features a linear phase slope along chirp index n_c, which is related to the Doppler shift

$$f_D = \frac{2v}{c_0} f_{cr} \tag{2.16}$$

that the signal experiences and which can be utilized for the velocity estimation. The fifth term takes into account that not only the range of a moving target changes during a radar measurement, but also the induced Doppler shift is dependent on the instantaneous carrier frequency which in turn changes during the transmission of a chirp. This so-called range-Doppler migration plays an important role in radar signal processing as will be further elaborated in chapter

5. The last term describes the phase offset of the beat signal which will later be derived as antenna-element-specific and which can be used for the estimation of the AoA of the target when multiple antennas are employed.

2.3 Signal Processing

For the subsequent radar signal processing, the beat signal phase from (2.15) is simplified with regard to the terms needed for the range and Doppler estimation, since only the basic principle of the detection process shall be shown. More detailed and mathematically complete derivations can be found in chapter 5.2 and 6.2. In addition, by taking advantage of the relations

$$v \ll c_0 \tag{2.17}$$

$$B \ll f_{\mathrm{cr}} \tag{2.18}$$

$$\tau_0 \ll T_{\mathrm{s}} \tag{2.19}$$

the phase of the beat signal can be further streamlined to

$$\varphi_{\mathrm{b}}(t, n_{\mathrm{c}}) = 2\pi \left[\frac{B}{T_{\mathrm{s}}} \tau_0 \cdot t + \frac{2v}{c_0} f_{\mathrm{cr}} \cdot n_{\mathrm{c}} T_{\mathrm{c}} \right] \tag{2.20}$$

The analog-to-digital converter (ADC) of the radar sensor discretizes the beat signal with the sample frequency of f_{s} and thereby substitutes the time-continuous variable t with the time-discrete sample index n_{s}

$$t \rightarrow \frac{n_{\mathrm{s}}}{f_{\mathrm{s}}} \tag{2.21}$$

resulting in a time-discrete beat signal phase of

$$\varphi_{\mathrm{b}}(n_{\mathrm{s}}, n_{\mathrm{c}}) = 2\pi \left[\frac{B}{N_{\mathrm{s}}} \tau_0 \cdot n_{\mathrm{s}} + \frac{2v}{\lambda} T_{\mathrm{c}} \cdot n_{\mathrm{c}} \right] \tag{2.22}$$

where $N_{\mathrm{s}} = T_{\mathrm{s}} f_{\mathrm{s}}$ describes the number of samples per chirp.

2.3.1 Range Estimation

For the range estimation of the target, first, a fast Fourier transform (FFT) is applied to the sampled beat signal which corresponds to sample-wise multiplication with a complex exponential term and summation over all samples N_s

$$\begin{aligned} s_\mathrm{R}(k, n_\mathrm{c}) &= \sum_{n_\mathrm{s}=0}^{N_\mathrm{s}-1} s_\mathrm{b}(n_\mathrm{s}, n_\mathrm{c}) \cdot \exp\left\{-\mathrm{j}2\pi \frac{k \cdot n_\mathrm{s}}{N_\mathrm{s}}\right\} \\ &= \exp\left\{\mathrm{j}2\pi \left[\frac{2v}{\lambda} T_\mathrm{c} \cdot n_\mathrm{c}\right]\right\} \cdot \sum_{n_\mathrm{s}=0}^{N_\mathrm{s}-1} \exp\left\{j2\pi \left[B\tau_0 - k\right] \cdot \frac{n_\mathrm{s}}{N_\mathrm{s}}\right\} \end{aligned} \tag{2.23}$$

where $k \in [0, N_\mathrm{s} - 1]$ describes the bin index of the newly formed value-discrete range spectrum. The expression can be reformulated using the partial sum of a geometrical series [BSMM01] and Euler's formula [Kön13] to

$$\begin{aligned} \sum_{n_\mathrm{s}=0}^{N_\mathrm{s}-1} \exp\left\{j2\pi \left[B\tau_0 - k\right] \cdot \frac{n_\mathrm{s}}{N_\mathrm{s}}\right\} &= \frac{1 - \exp\left\{\mathrm{j}2\pi \left[B\tau_0 - k\right]\right\}}{1 - \exp\left\{\mathrm{j}2\pi \left[B\tau_0 - k\right] \frac{1}{N_\mathrm{s}}\right\}} \\ &= \frac{\exp\left\{\mathrm{j}\pi \left[B\tau_0 - k\right]\right\}}{\exp\left\{\mathrm{j}\pi \left[B\tau_0 - k\right] \frac{1}{N_\mathrm{s}}\right\}} \\ &\quad \cdot \frac{\exp\left\{\mathrm{j}\pi \left[B\tau_0 - k\right]\right\} - \exp\left\{-\mathrm{j}\pi \left[B\tau_0 - k\right]\right\}}{\exp\left\{\mathrm{j}\pi \left[B\tau_0 - k\right] \frac{1}{N_\mathrm{s}}\right\} - \exp\left\{-\mathrm{j}\pi \left[B\tau_0 - k\right] \frac{1}{N_\mathrm{s}}\right\}} \\ &= \exp\left\{\mathrm{j}\pi \left[B\tau_0 - k\right] \left(1 - \frac{1}{N_\mathrm{s}}\right)\right\} \cdot \frac{\sin\left(\pi \left[B\tau_0 - k\right]\right)}{\sin\left(\pi \left[B\tau_0 - k\right] \frac{1}{N_\mathrm{s}}\right)} \end{aligned} \tag{2.24}$$

For $\left|\pi \left[B\tau_0 - k\right] \frac{1}{N_\mathrm{s}}\right| \ll 1$, the sine function in the denominator can be substituted with its argument, forming a sinc-function

$$\frac{\sin\left(\pi \left[B\tau_0 - k\right]\right)}{\sin\left(\pi \left[B\tau_0 - k\right] \frac{1}{N_\mathrm{s}}\right)} \approx N_\mathrm{s} \cdot \mathrm{sinc}\left(B\tau_0 - k\right) \tag{2.25}$$

Replacing the sum in (2.23) with these equations allows to simplify the expression to

$$s_{\mathrm{R}}(k, n_{\mathrm{c}}) = N_{\mathrm{s}} \cdot \operatorname{sinc}(B\tau_0 - k) \cdot \exp\left\{\mathrm{j}2\pi\left[\frac{2v}{\lambda}T_{\mathrm{c}} \cdot n_{\mathrm{c}} + \frac{B\tau_0 - k}{2}\left(1 - \frac{1}{N_{\mathrm{s}}}\right)\right]\right\} \tag{2.26}$$

The maximum of the sinc-function can be detected as

$$k_{\mathrm{det}} = B\tau_0 \tag{2.27}$$

which in turn enables the estimation of the range of the target to

$$R_{\mathrm{det}} = k_{\mathrm{det}} \cdot \frac{c_0}{2B} = R_0 \tag{2.28}$$

2.3.2 Velocity Estimation

The estimation of the velocity of the target proceeds similar to the range estimation. A second FFT is applied to the output of the first one, resulting in

$$\begin{aligned} s_{\mathrm{D}}(k, m) &= \sum_{n_{\mathrm{c}}=0}^{N_{\mathrm{c}}-1} s_{\mathrm{R}}(k, n_{\mathrm{c}}) \cdot \exp\left\{-\mathrm{j}2\pi\frac{m \cdot n_{\mathrm{c}}}{N_{\mathrm{c}}}\right\} \\ &= N_{\mathrm{s}} \cdot \exp\left\{\mathrm{j}2\pi\left[\frac{B\tau_0 - k}{2}\left(1 - \frac{1}{N_{\mathrm{s}}}\right)\right]\right\} \cdot \operatorname{sinc}(B\tau_0 - k) \\ &\quad \cdot \sum_{n_{\mathrm{c}}=0}^{N_{\mathrm{c}}-1} \exp\left\{j2\pi\left[\frac{2v}{\lambda}T_{\mathrm{m}} - m\right] \cdot \frac{n_{\mathrm{c}}}{N_{\mathrm{c}}}\right\} \end{aligned} \tag{2.29}$$

where $T_{\mathrm{m}} = T_{\mathrm{c}}N_{\mathrm{c}}$ denotes the complete measurement time and $m \in [0, N_{\mathrm{c}} - 1]$ describes the bin index of the Doppler spectrum. In the same manner as in

(2.23), the expression can be reformulated using the partial sum of a geometric series and Euler's formula to

$$\sum_{n_\mathrm{c}=0}^{N_\mathrm{c}-1} \exp\left\{ j2\pi \left[\frac{2v}{\lambda} T_\mathrm{m} - m \right] \cdot \frac{n_\mathrm{c}}{N_\mathrm{c}} \right\} = \frac{1 - \exp\left\{ \mathrm{j}2\pi \left[\frac{2v}{\lambda} T_\mathrm{m} - m \right] \right\}}{1 - \exp\left\{ \mathrm{j}2\pi \left[\frac{2v}{\lambda} T_\mathrm{m} - m \right] \frac{1}{N_\mathrm{c}} \right\}} \tag{2.30}$$

$$= \frac{\exp\left\{ \mathrm{j}\pi \left[\frac{2v}{\lambda} T_\mathrm{m} - m \right] \right\}}{\exp\left\{ \mathrm{j}\pi \left[\frac{2v}{\lambda} T_\mathrm{m} - m \right] \frac{1}{N_\mathrm{c}} \right\}} \cdot \frac{\exp\left\{ \mathrm{j}\pi \left[\frac{2v}{\lambda} T_\mathrm{m} - m \right] \right\} - \exp\left\{ -\mathrm{j}\pi \left[\frac{2v}{\lambda} T_\mathrm{m} - m \right] \right\}}{\exp\left\{ \mathrm{j}\pi \left[\frac{2v}{\lambda} T_\mathrm{m} - m \right] \frac{1}{N_\mathrm{c}} \right\} - \exp\left\{ -\mathrm{j}\pi \left[\frac{2v}{\lambda} T_\mathrm{m} - m \right] \frac{1}{N_\mathrm{c}} \right\}}$$

$$= \exp\left\{ \mathrm{j}\pi \left[\frac{2v}{\lambda} T_\mathrm{m} - m \right] \left(1 - \frac{1}{N_\mathrm{c}} \right) \right\} \cdot \frac{\sin\left(\pi \left[\frac{2v}{\lambda} T_\mathrm{m} - m \right] \right)}{\sin\left(\pi \left[\frac{2v}{\lambda} T_\mathrm{m} - m \right] \frac{1}{N_\mathrm{c}} \right)}$$

Similar to before, the sine function in the denominator can be approximated with its argument for $\left| \pi \left[\frac{2v}{\lambda} T_\mathrm{m} - m \right] \frac{1}{N_\mathrm{c}} \right| \ll 1$, forming a sinc-function

$$\frac{\sin\left(\pi \left[\frac{2v}{\lambda} T_\mathrm{m} - m \right] \right)}{\sin\left(\pi \left[\frac{2v}{\lambda} T_\mathrm{m} - m \right] \frac{1}{N_\mathrm{c}} \right)} \approx N_\mathrm{c} \cdot \mathrm{sinc}\left(\frac{2v}{\lambda} T_\mathrm{m} - m \right) \tag{2.31}$$

which together with (2.30) can substitute for the sum in (2.29) leading to

$$s_\mathrm{D}(k, m) = N_\mathrm{s} N_\mathrm{c} \cdot \mathrm{sinc}\left(B\tau_0 - k \right) \cdot \mathrm{sinc}\left(\frac{2v}{\lambda} T_\mathrm{m} - m \right) \tag{2.32}$$

$$\cdot \exp\left\{ \mathrm{j}\pi \left[\left(B\tau_0 - k \right) \left(1 - \frac{1}{N_\mathrm{s}} \right) + \left(\frac{2v}{\lambda} T_\mathrm{m} - m \right) \left(1 - \frac{1}{N_\mathrm{c}} \right) \right] \right\}$$

The maximum of the second sinc-function can be detected as

$$m_\mathrm{det} = \frac{2v}{\lambda} T_\mathrm{m} \tag{2.33}$$

from which the Doppler frequency and the velocity of the target can be derived to

$$f_{\mathrm{D,det}} = \frac{m_{\mathrm{det}}}{T_{\mathrm{m}}} = \frac{2v}{\lambda} \tag{2.34}$$

$$v_{\mathrm{det}} = m_{\mathrm{det}} \cdot \frac{\lambda}{2T_{\mathrm{m}}} = \frac{f_{\mathrm{D}}}{2}\lambda = v \tag{2.35}$$

2.4 Angle of Arrival Estimation

In order to determine the exact position of the target, in addition to the range information, the angle of incidence of the back-reflected electromagnetic wave must also be measured. For the case of a single transmit and multiple receive antennas, the radar sensor takes advantage of the fact that the impinging wave is received at the receive antenna elements with a relative phase offset of

$$\Delta\varphi_{\mathrm{rx}} = 2\pi \frac{d_{\mathrm{rx}} \sin(\theta)}{\lambda} \cdot n_{\mathrm{rx}} \,, \qquad n_{\mathrm{rx}} \in [0, N_{\mathrm{rx}} - 1] \tag{2.36}$$

where d_{rx} describes the lateral distance between the antenna elements, $\theta \in [-90°, 90°]$ the incident angle of the reflected wave, n_{rx} the receive antenna element index and N_{rx} the number of receive antennas. The phase offset, in turn, translates to an element-specific signal delay of

$$\tau = \tau_0 + \frac{d_{\mathrm{rx}} \sin(\theta)}{c_0} \cdot n_{\mathrm{rx}} \tag{2.37}$$

which can later be exploited to estimate the AoA.

2.4.1 Virtual Antenna Array

In the case of multiple transmit and receive antennas, a virtual antenna array can be formed. The principle of a virtual antenna array is based on the simulation of a virtual receive array in the digital domain, whose number of channels is greater than the number of physically existing transmit (N_{tx}) and receive antennas (N_{rx}). The combination of a transmit and a receive antenna forms a channel, the corresponding relative phase offset of which behaves as if a larger array of only

one transmit but $N_{\mathrm{tx}} \cdot N_{\mathrm{rx}}$ receive antennas existed. A prerequisite for this is that the signals of the different transmitters can be separated unambiguously at each receiver. For this, the multiple-input multiple-output (MIMO) method can be employed which uses orthogonal or uncorrelated signals for the separation. It allows to clearly define a transmit-receive antenna pair to be assigned to each of the orthogonal signals in the receiver after their separation, which in turn corresponds to one of the elements in the virtual antenna array. This creates a virtual antenna array with $N_{\mathrm{A}} = N_{\mathrm{tx}} \cdot N_{\mathrm{rx}}$ antenna elements that is larger in its lateral dimensions when compared to the actual, physical array, hence enables a better angular resolution and a larger unambiguous angle region [Nus21]. The relative phase among the virtual antenna elements is

$$\Delta\varphi_{\mathrm{A}} = 2\pi \frac{d_{\mathrm{A}} \sin(\theta)}{\lambda} \cdot n_{\mathrm{A}} \,, \qquad n_{\mathrm{A}} \in [0, N_{\mathrm{A}} - 1] \tag{2.38}$$

where d_{A} describes the lateral element spacing and $n_{\mathrm{A}} = n_{\mathrm{rx}} + N_{\mathrm{rx}} \cdot n_{\mathrm{tx}}$ the element index. The phase progression corresponds to an element-specific signal delay of

$$\tau = \tau_0 + \frac{d_{\mathrm{A}} \sin(\theta)}{c_0} \cdot n_{\mathrm{A}} \tag{2.39}$$

2.4.2 Digital Beamforming

In order to extract the angle information from the relative phase offset among antenna elements of the impinging radar wave, digital beamforming can be applied. This process operates similar to a Fourier transform insofar that it creates a (pseudo) spectrum that enables to determine the signal's spatial frequency. In this case, it is a spatial spectrum that results from the lateral distribution of the antenna elements and which correlates with the incidence angle. Digital beamforming can theoretically be applied either before or after the range-Doppler processing, as it is compatible with time and frequency sampling, but is often performed after the range-Doppler detection to save precious hardware resources [Sit17].

For the subsequent processing steps, the phase of the beat signal from (2.15) is adjusted to take into account the antenna-element-specific delay in (2.39). As

only the basic principle of the digital beamforming process shall be shown, the expression is reduced to the angle-dependent terms

$$\varphi_\mathrm{b}(n_\mathrm{A}) = 2\pi \left[\left(f_\mathrm{cr} - \frac{B}{T_\mathrm{s}}\tau_0 \right) \frac{d_\mathrm{A}\sin(\theta)}{c_0} \cdot n_\mathrm{A} + \frac{B}{2T_\mathrm{s}} \left(\frac{d_\mathrm{A}\sin(\theta)}{c_0} \cdot n_\mathrm{A} \right)^2 + \tau_0 \left(f_\mathrm{cr} - \frac{B}{2T_\mathrm{s}}\tau_0 \right) \right] \tag{2.40}$$

which in turn can be further simplified using the relations in (2.18) and (2.19) to

$$\varphi_\mathrm{b}(n_\mathrm{A}) = 2\pi \left[\frac{d_\mathrm{A}\sin(\theta)}{\lambda} \cdot n_\mathrm{A} + \tau_0 f_\mathrm{cr} \right] \tag{2.41}$$

$$s_\mathrm{b}(n_\mathrm{A}) = \exp\left\{ \mathrm{j}\varphi_\mathrm{b}(n_\mathrm{A}) \right\} \tag{2.42}$$

To estimate the AoA of the target, the one-dimensional beamsteering vector

$$b_\mathrm{1D}(n_\mathrm{A}, \alpha) = \exp\left\{ -\mathrm{j}2\pi \frac{d_\mathrm{A}\sin(\alpha)}{\lambda} \cdot n_\mathrm{A} \right\} \tag{2.43}$$

where $\alpha \in [-90°, 90°]$ describes all evaluation angles to be considered and can be discretized arbitrarily. The vector can be used to apply a Fourier beamforming to the beat signal from (2.42)

$$\begin{aligned} s_\mathrm{A}(\alpha) &= \sum_{n_\mathrm{A}=-\frac{N_\mathrm{A}-1}{2}}^{\frac{N_\mathrm{A}-1}{2}} s_\mathrm{b}(n_\mathrm{A}) \cdot \exp\left\{ -\mathrm{j}2\pi \frac{d_\mathrm{A}\sin(\alpha)}{\lambda} \cdot n_\mathrm{A} \right\} \\ &= \sum_{n_\mathrm{A}=0}^{N_\mathrm{A}-1} s_\mathrm{b}(n_\mathrm{A}) \cdot \exp\left\{ -\mathrm{j}2\pi \frac{d_\mathrm{A}\sin(\alpha)}{\lambda} \left(n_\mathrm{A} - \frac{N_\mathrm{A}-1}{2} \right) \right\} \\ &= \exp\left\{ \mathrm{j}2\pi \left[\tau_0 f_\mathrm{cr} + \frac{d_\mathrm{A}\sin(\alpha)}{\lambda} \frac{N_\mathrm{A}-1}{2} \right] \right\} \\ &\quad \cdot \sum_{n_\mathrm{A}=0}^{N_\mathrm{A}-1} \exp\left\{ \mathrm{j}2\pi \left[\frac{d_\mathrm{A}}{\lambda} \left(\sin(\theta) - \sin(\alpha) \right) \cdot n_\mathrm{A} \right] \right\} \end{aligned} \tag{2.44}$$

The remaining sum can, as in the cases of the range and velocity estimation, be reformulated using the partial sum of a geometric series and Euler's formula to

$$\begin{aligned}
&\sum_{n_\mathrm{A}=0}^{N_\mathrm{A}-1} \exp\left\{\mathrm{j}2\pi\left[\frac{d_\mathrm{A}}{\lambda}\left(\sin(\theta)-\sin(\alpha)\right)\cdot n_\mathrm{A}\right]\right\} \qquad (2.45)\\
&= \frac{1-\exp\left\{\mathrm{j}2\pi\frac{d_\mathrm{A}}{\lambda}\left[\sin(\theta)-\sin(\alpha)\right]N_\mathrm{A}\right\}}{1-\exp\left\{\mathrm{j}2\pi\frac{d_\mathrm{A}}{\lambda}\left[\sin(\theta)-\sin(\alpha)\right]\right\}}\\
&= \frac{\exp\left\{\mathrm{j}\pi\frac{d_\mathrm{A}}{\lambda}\left[\sin(\theta)-\sin(\alpha)\right]N_\mathrm{A}\right\}}{\exp\left\{\mathrm{j}\pi\frac{d_\mathrm{A}}{\lambda}\left[\sin(\theta)-\sin(\alpha)\right]\right\}}\\
&\quad\cdot\frac{\exp\left\{\mathrm{j}\pi\frac{d_\mathrm{A}}{\lambda}\left[\sin(\theta)-\sin(\alpha)\right]N_\mathrm{A}\right\}-\exp\left\{-\mathrm{j}\pi\frac{d_\mathrm{A}}{\lambda}\left[\sin(\theta)-\sin(\alpha)\right]N_\mathrm{A}\right\}}{\exp\left\{\mathrm{j}\pi\frac{d_\mathrm{A}}{\lambda}\left[\sin(\theta)-\sin(\alpha)\right]\right\}-\exp\left\{-\mathrm{j}\pi\frac{d_\mathrm{A}}{\lambda}\left[\sin(\theta)-\sin(\alpha)\right]\right\}}\\
&= \exp\left\{\mathrm{j}\pi\frac{d_\mathrm{A}}{\lambda}\left[\sin(\theta)-\sin(\alpha)\right]\left(N_\mathrm{A}-1\right)\right\}\cdot\frac{\sin\left(\pi\frac{d_\mathrm{A}}{\lambda}\left[\sin(\theta)-\sin(\alpha)\right]N_\mathrm{A}\right)}{\sin\left(\pi\frac{d_\mathrm{A}}{\lambda}\left[\sin(\theta)-\sin(\alpha)\right]\right)}
\end{aligned}$$

As before, the sine function in the denominator can be substituted with its argument for $\left|\pi\frac{d_\mathrm{A}}{\lambda}\left[\sin(\theta)-\sin(\alpha)\right]\right| \ll 1$, forming a sinc-function

$$\frac{\sin\left(\pi\frac{d_\mathrm{A}}{\lambda}\left[\sin(\theta)-\sin(\alpha)\right]N_\mathrm{A}\right)}{\sin\left(\pi\frac{d_\mathrm{A}}{\lambda}\left[\sin(\theta)-\sin(\alpha)\right]\right)} \approx N_\mathrm{A}\cdot\operatorname{sinc}\left(\frac{d_\mathrm{A}}{\lambda}\left[\sin(\theta)-\sin(\alpha)\right]N_\mathrm{A}\right) \qquad (2.46)$$

which together with (2.45) can replace the sum in (2.44) resulting in

$$\begin{aligned}
s_\mathrm{A}(\alpha) = N_\mathrm{A}\cdot\operatorname{sinc}&\left(\frac{d_\mathrm{A}}{\lambda}\left[\sin(\theta)-\sin(\alpha)\right]N_\mathrm{A}\right) \qquad (2.47)\\
&\cdot\exp\left\{\mathrm{j}2\pi\left[\tau_0 f_\mathrm{cr}+\frac{d_\mathrm{A}\sin(\theta)}{\lambda}\frac{N_\mathrm{A}-1}{2}\right]\right\}
\end{aligned}$$

From this, the AoA of the target can be detected as

$$\sin(\alpha_{\text{det}}) = \sin(\theta) \tag{2.48}$$

$$\alpha_{\text{det}} = \theta \tag{2.49}$$

Two-dimensional Digital Beamforming

Modern radar sensors tend to have a two-dimensional distribution of their transmit and receive antennas, which enables them to resolve targets in the azimuth and elevation domain simultaneously. The horizontal and vertical positions of the virtual antenna elements can be described exemplarily as follows

$$p_{\text{az}} = d_{\text{az,tx}} \cdot n_{\text{tx}} + d_{\text{az,rx}} \cdot n_{\text{rx}} \tag{2.50}$$

$$p_{\text{el}} = d_{\text{el,tx}} \cdot n_{\text{tx}} + d_{\text{el,rx}} \cdot n_{\text{rx}} \tag{2.51}$$

where $d_{\text{az/el,tx/rx}}$ denotes the horizontal/vertical spacing of the transmit/receive antennas, respectively. With this, the relative phase offset of the virtual receive antenna elements can be described as

$$\Delta\varphi_{\text{A}} = 2\pi \frac{\sin(\theta)\cos(\psi) \cdot p_{\text{az}} + \sin(\psi) \cdot p_{\text{el}}}{\lambda} \tag{2.52}$$

where $\psi \in [-90°, 90°]$ is the incidence angle of the reflected wave in the elevation plane. This in turn results in an element-specific signal delay of

$$\tau = \tau_0 + \frac{\sin(\theta)\cos(\psi) \cdot p_{\text{az}} + \sin(\psi) \cdot p_{\text{el}}}{c_0} \tag{2.53}$$

For the subsequent processing steps, the phase of the beat signal from (2.15) is adjusted to take into account the two-dimensional, antenna-element-specific delay in (2.53). Similar to before, only the basic principle of the digital beam-

forming process shall be shown, which is why the expression is reduced to the angle-dependent terms

$$\varphi_{\mathrm{b}}(n_{\mathrm{A}}) = 2\pi \left[\left(f_{\mathrm{cr}} - \frac{B}{T_{\mathrm{s}}} \tau_0 \right) \frac{\sin(\theta)\cos(\psi) \cdot p_{\mathrm{az}} + \sin(\psi) \cdot p_{\mathrm{el}}}{c_0} \right. \tag{2.54}$$
$$\left. + \frac{B}{2T_{\mathrm{s}}} \left(\frac{\sin(\theta)\cos(\psi) \cdot p_{\mathrm{az}} + \sin(\psi) \cdot p_{\mathrm{el}}}{c_0} \right)^2 + \tau_0 \left(f_{\mathrm{cr}} - \frac{B}{2T_{\mathrm{s}}} \tau_0 \right) \right]$$

Considering that in conventional radar sensors the transmit and receive antennas are each distributed in only one spatial dimension [Sys21, Har14], the position of the virtual elements can be simplified to

$$p_{\mathrm{az}} = d_{\mathrm{rx}} \cdot n_{\mathrm{rx}} \tag{2.55}$$
$$p_{\mathrm{el}} = d_{\mathrm{tx}} \cdot n_{\mathrm{tx}} \tag{2.56}$$

and thus the beat signal and its phase, also taking into account the relations in (2.18) and (2.19), can be reduced to

$$\varphi_{\mathrm{b}}(n_{\mathrm{tx}}, n_{\mathrm{rx}}) = 2\pi \left[\frac{\sin(\theta)\cos(\psi) d_{\mathrm{rx}} \cdot n_{\mathrm{rx}} + \sin(\psi) d_{\mathrm{tx}} \cdot n_{\mathrm{tx}}}{\lambda} + \tau_0 f_{\mathrm{cr}} \right] \tag{2.57}$$
$$s_{\mathrm{b}}(n_{\mathrm{tx}}, n_{\mathrm{rx}}) = \exp\left\{ \mathrm{j} \varphi_{\mathrm{b}}(n_{\mathrm{A}}) \right\} \tag{2.58}$$

With the two-dimensional beamsteering vector

$$b_{\mathrm{2D}}(n_{\mathrm{tx}}, n_{\mathrm{rx}}, \alpha, \beta) = \exp\left\{ -\mathrm{j} \frac{2\pi}{\lambda} \left[d_{\mathrm{rx}} \sin(\alpha)\cos(\beta) \cdot n_{\mathrm{rx}} + d_{\mathrm{tx}} \sin(\beta) \cdot n_{\mathrm{tx}} \right] \right\} \tag{2.59}$$

a two-dimensional Fourier beamforming can be applied, leading to

$$
\begin{aligned}
s_{\mathrm{A}}(\alpha,\beta) &= \sum_{n_{\mathrm{tx}}=-\frac{N_{\mathrm{tx}}-1}{2}}^{\frac{N_{\mathrm{tx}}-1}{2}} \sum_{n_{\mathrm{rx}}=-\frac{N_{\mathrm{rx}}-1}{2}}^{\frac{N_{\mathrm{rx}}-1}{2}} s_{\mathrm{b}}(n_{\mathrm{tx}},n_{\mathrm{rx}}) \cdot b_{\mathrm{2D}}(n_{\mathrm{tx}},n_{\mathrm{rx}},\alpha,\beta) \qquad (2.60)\\
&= \exp\left\{\mathrm{j}2\pi\left[\tau_0 f_{\mathrm{cr}} + \frac{d_{\mathrm{rx}}}{\lambda}\sin(\alpha)\cos(\beta)\frac{N_{\mathrm{rx}}-1}{2} + \frac{d_{\mathrm{tx}}}{\lambda}\sin(\beta)\frac{N_{\mathrm{rx}}-1}{2}\right]\right\}\\
&\quad\cdot \sum_{n_{\mathrm{tx}}=0}^{N_{\mathrm{tx}}-1}\sum_{n_{\mathrm{rx}}=0}^{N_{\mathrm{rx}}-1} \exp\left\{\mathrm{j}\frac{2\pi}{\lambda}\left[d_{\mathrm{rx}}\left(\sin(\theta)\cos(\psi)-\sin(\alpha)\cos(\beta)\right)\cdot n_{\mathrm{rx}}\right.\right.\\
&\qquad\qquad \left.\left. + d_{\mathrm{tx}}\left(\sin(\psi)-\sin(\beta)\right)\cdot n_{\mathrm{tx}}\right]\right\}
\end{aligned}
$$

The two sums can be simplified individually utilizing the same procedure as before, resulting in

$$
\begin{aligned}
s_{\mathrm{A}}(\alpha,\beta) = N_{\mathrm{A}} \cdot \exp&\left\{\mathrm{j}2\pi\left[\tau_0 f_{\mathrm{cr}} + \frac{d_{\mathrm{rx}}}{\lambda}\sin(\theta)\cos(\psi)\frac{N_{\mathrm{rx}}-1}{2}\right.\right. \qquad (2.61)\\
&\qquad\left.\left. + \frac{d_{\mathrm{tx}}}{\lambda}\sin(\psi)\frac{N_{\mathrm{rx}}-1}{2}\right]\right\}\\
&\cdot \operatorname{sinc}\left(\frac{d_{\mathrm{rx}}}{\lambda}\left[\sin(\theta)\cos(\psi)-\sin(\alpha)\cos(\beta)\right]N_{\mathrm{rx}}\right)\\
&\cdot \operatorname{sinc}\left(\frac{d_{\mathrm{tx}}}{\lambda}\left[\sin(\psi)-\sin(\beta)\right]N_{\mathrm{tx}}\right)
\end{aligned}
$$

From this, the azimuth and elevation AoA of the target can be detected as

$$\sin(\alpha_{\mathrm{det}})\cos(\beta_{\mathrm{det}}) = \sin(\theta)\cos(\psi) \qquad (2.62)$$

$$\sin(\beta_{\mathrm{det}}) = \sin(\psi) \qquad (2.63)$$

$$\alpha_{\mathrm{det}} = \theta \qquad (2.64)$$

$$\beta_{\mathrm{det}} = \psi \qquad (2.65)$$

2.5 Limitations

Depending on the parameterization of a radar sensor, different limitations arise with regard to its achievable resolutions and unambiguous measurement regions.

2.5.1 Resolution

In radar applications, it is important to distinguish between resolution and accuracy. The resolution of a radar describes its ability to discriminate two objects and cannot be improved through sheer signal processing, whereas the accuracy represents the precision with which the parameters of a target can be estimated which can be improved, for example, by zero padding or interpolation methods [RSSH10].

Range Resolution

The range resolution of a radar specifies how close together two point targets with identical velocity and RCS can be in order to still be perceived as two separate objects. It follows from the consideration that the resolution of the beat signal frequency is equal the inverse of the sampling time [PL15]

$$\Delta f_\mathrm{b} = \frac{1}{T_\mathrm{s}} \tag{2.66}$$

which together with the relation of the constant frequency slope of

$$\frac{B}{T_\mathrm{s}} = \frac{f_\mathrm{b}}{\tau} \tag{2.67}$$

yields the range resolution of

$$\Delta R = \frac{c_0}{2B} \tag{2.68}$$

Velocity Resolution

Similar to the range resolution, the definition of the velocity resolution follows the consideration that the resolution of the Doppler frequency is equal to the inverse of the measurement time

$$\Delta f_{\mathrm{D}} = \frac{1}{T_{\mathrm{m}}} \tag{2.69}$$

which can be substituted in (2.16) to give the velocity resolution of

$$\Delta v = \frac{c_0}{2 f_{\mathrm{cr}} T_{\mathrm{m}}} \tag{2.70}$$

Angular Resolution

Proceeding in the same manner as before, the spatial frequency along the spatial sample points, i.e. the antenna elements, can be set in relation to the AoA of the target by deriving the relative phase in (2.38) according to the spatial sample index

$$f_{\mathrm{A}} = \frac{1}{2\pi} \frac{\partial \varphi_{\mathrm{A}}}{\partial (d_{\mathrm{A}} n_{\mathrm{A}})} = \frac{\sin(\theta)}{\lambda} \tag{2.71}$$

The frequency resolution is again defined by the inverse of the (spatial) sampling period

$$\Delta f_{\mathrm{A}} = \frac{1}{d_{\mathrm{A}} N_{\mathrm{A}}} \tag{2.72}$$

This allows to express the analytical angular resolution as

$$\Delta \alpha_{\mathrm{ana}} = \arcsin\left(\frac{\lambda}{d_{\mathrm{A}} N_{\mathrm{A}}}\right) \tag{2.73}$$

All of the above definitions for the respective resolutions are to be regarded as theoretical statements only. Due to hardware imperfections and the influence of noise, they cannot be achieved in practice. For the range and velocity resolution,

this circumstance is not decisive, since they are quite fine and factorial deviations have only a negligible impact.

Of greater importance, however, is the precise estimation of the angular resolution, which is why two adapted definitions can be found in literature. Both are based on considerations concerning the sinc-function that arises after the beamforming process in (2.47). The first one states that two targets can be resolved in the angular domain, if the maxima of the corresponding sinc-functions are separated by at least twice the half-power beamwidth [Bal15]. The half-power beamwidth, in turn, can be found by solving

$$\operatorname{sinc}\left(x_{\mathrm{hp}}\right) = \frac{1}{\sqrt{2}} \tag{2.74}$$

numerically which results in $x_{\mathrm{hp}} = 0.443$. With this and $\sin(x) \approx x$, the first literature angular resolution definition can be expressed as

$$\Delta\alpha_{\mathrm{hp}} = \frac{0.886\lambda}{d_{\mathrm{A}} N_{\mathrm{A}}} \tag{2.75}$$

The second definition is based on the Rayleigh criterion and determines the angular resolution for the case that the maximum of the first sinc-function coincides with the first minimum of the second [Hec12, HTS+12] which leads to

$$\Delta\alpha_{\mathrm{rc}} = \frac{1.22\lambda}{d_{\mathrm{A}} N_{\mathrm{A}}} \tag{2.76}$$

A common constraint for both definitions is that the two targets to be resolved are incoherent in regards of the phase of their corresponding radar echoes. This means that the superposition of their reflected radar signals occurs only in accordance to the signal powers, not the phases [RSSH10]. Moreover, the definitions are only accurate for targets at the antenna array's broadside at $\theta = 0°$ and worsen with increasing AoA, since the sinc-function broadens.

2.5.2 Unambiguity

The unambiguity regions indicate up to which maximum range, velocity or angle of an object the radar sensor can still estimate its parameters correctly. Beyond this limit, the target can still be detected – except for the AoA – if the sensor is not limited by noise, but then the estimated value no longer corresponds to the actual one. This is ultimately due to the fact that if the sampling theorem is violated, the detection which lies above the maximum value is folded into the previous unambiguity region.

Maximum Unambiguous Range

The maximum unambiguous range is defined by the maximum frequency of the beat signal that can still be measured unambiguously, which in turn is given by the Nyquist–Shannon sampling theorem [Whi15]

$$f_{\mathrm{b,ua}} = \frac{f_{\mathrm{s}}}{2} \tag{2.77}$$

With this, the maximum unambiguous range can be derived as

$$R_{\mathrm{ua}} = \frac{c_0 T_{\mathrm{s}} f_{\mathrm{s}}}{4B} \tag{2.78}$$

Maximum Unambiguous Velocity

According to the sampling theorem, the maximum unambiguously measurable Doppler frequency is defined by the chirp repetition period

$$f_{\mathrm{D,ua}} = \frac{1}{2T_{\mathrm{c}}} \tag{2.79}$$

which leads to the maximum unambiguous velocity of

$$v_{\mathrm{ua}} = \frac{c_0}{4T_{\mathrm{c}} f_{\mathrm{cr}}} \tag{2.80}$$

Maximum Unambiguous Angle of Arrival

Applying the sampling theorem to spatial sampling, the maximum unambiguously measurable spatial frequency (2.71) is defined by the spatial sampling period d_A [Har14]

$$f_{\mathrm{A,ua}} = \frac{1}{2d_\mathrm{A}} \tag{2.81}$$

which results in the maximum unambiguous AoA of

$$\alpha_{\mathrm{ua}} = \arcsin\left(\frac{\lambda}{2d_\mathrm{A}}\right) \tag{2.82}$$

3 Radar Target Simulation

This chapter elaborates on the state of the art of radar target simulation, both in research and the commercial sector. First, the basic principle as well as the different modes of operation of RTS systems are discussed, before their miscellaneous applications and use cases are presented. Next, the distinctive characteristics of a radar target and the corresponding signal modifications that an RTS system must perform in order to simulate virtual radar targets are explained. The two possible implementation topologies to realize these signal modifications are presented before finally the topologies as well as the different concepts for the target generation and the angle simulation are compared.

3.1 Basic Principle

The basic idea of an RTS system is to deceive a radar under test (RuT) by creating an artificial environment that comprises of one or multiple virtual radar targets. For this purpose, the RTS generates synthetic radar signal echoes and emits them towards the RuT which interprets them as reflections of real-world objects. In order to create these artificial echoes, the RTS system receives the radar signal emitted by the RuT, down-converts and modifies it with regard to the desired target characteristics and subsequently up-converts and re-transmits it towards the RuT. The modifications of the radar signal can be realized using an analog or digital system topology as is further explained in chapter 3.4. There are alternative solutions where the incoming signal is not modified, but analyzed and re-synthesized with alterations that correspond to the desired target properties. The operating principle of both concepts are discussed in more detail in chapter 3.3 and their pros and cons are elaborated in section 3.5.2.

3.2 Applications

Radar target simulation is mainly used in three different applications. The first one is end-of-line production testing as part of the quality assurance process of radar sensor manufacturers. It serves the purpose of calibrating the sensor and verifying its functionality after its final assembly. The RTS systems developed for this application [Roh21a, Key17, dSP20, Kon17b, Ros16] simulate only a single target at high accuracy and the processed output of the radar sensors is set in reference to the ground truth.

The next use case is the development of ADAS functions that are implemented directly on the hardware of the radar sensor. In this context, RTS systems provide a powerful debugging tool that enables the stimulation of the RuT with synthetic radar echoes while monitoring the output of the driving function under development [Key22, dSP21]. In this application, the sensor is tested independently and segregated from its later application site.

In contrast, the third use case concerns the in-place verification of the radar sensor integrated in an autonomous vehicle including the interaction with its connected devices. For this, a vehicle under test (VuT) is placed on a test bench that is wired to a virtual vehicle environment (VVE) simulation in which a digital clone of the car is emulated. The torque, steering, pitch and roll forces that the clone is exposed to are applied to the VuT on the test bench through electric motors and its behavioral response is fed back into the VVE simulation. The integrated radar sensor of the VuT is stimulated by an RTS system which receives a list of the virtual radar targets that it is supposed to simulate from the VVE simulation. RTS systems that are employed for this application must be able to generate a multitude of different synthetic radar echoes simultaneously in order to simulate complex traffic scenarios and thus suffice the requirements of ADAS validation tests [Roh21b, WMN+20, GMS+18, BAB+21, GSG+18]. This setup is considered a Vehicle-in-the-Loop test system and enables holistic verification of autonomous driving functions with the radar sensor deployed in its actual operation site. The basic concept of the setup is illustrated in Fig. 3.1.

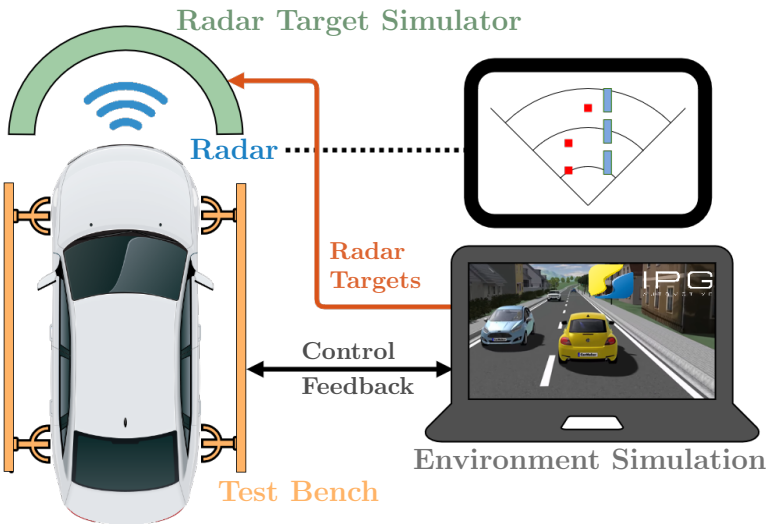

Figure 3.1: Basic concept of an RTS system integrated in a Vehicle-in-the-Loop test bench for the application of ADAS validation testing

3.3 Target Generation Methods

As discussed in chapter 2, a radar target is characterized by four distinct properties: range, velocity, electromagnetic reflectivity (cf. RCS) and angular position. These characteristics correspond to alterations of the received signal of the radar sensor in comparison to the transmitted one in terms of delay, Doppler frequency shift, amplitude and phase offset among the antenna elements of the RuT. Hence, an RTS system must simulate all of these signal amendments in order to generate a virtual radar target.

3.3.1 Range, Doppler and RCS Simulation

As mentioned before, an RTS system creates virtual targets by receiving the emitted radar signal from the RuT and sending back a modified version of it. The altered signal can be generated either by modifying the incoming original radar signal [IRW21, Roh21b, GGS+17] – hereafter referred to as the modifica-

tion approach – or analyzing and re-synthesizing it with changes [DMW18] – hereafter called the re-synthesis approach.

The Modification Approach

The modification approach, in turn, can be divided into two different implementations, which differ only in the simulation of the range of the target. In the first implementation, this target property is mimicked by delaying the incoming radar signal by the same amount as it would be if it were propagating in free space to and from the real-world object [EPB16, GGS+17, LEWW14]. Thus, there required latency that the RTS needs to apply is

$$\tau_{\mathrm{rts}} = \frac{2R_{\mathrm{sim}}}{c_0} \tag{3.1}$$

where R_{sim} describes the range of the simulated target. The second implementation takes advantage of the fact that FMCW and chirp sequence radar receivers transform signal delay into a beat frequency. Hence, shifting the frequency of the incoming radar signal at the RTS by

$$f_{\mathrm{R,rts}} = \frac{B}{T_{\mathrm{s}}}\tau_{\mathrm{rts}} = \frac{2BR_{\mathrm{sim}}}{T_{\mathrm{s}}c_0} \tag{3.2}$$

enables to control the frequency of the beat signal directly, which is later interpreted by the radar sensor as the target range [RH20, RISW22, SSGW21].

The simulation of the RCS and the velocity of the virtual target is the same for both implementations. The latter is realized through a frequency shift of

$$f_{\mathrm{D,rts}} = \frac{2f_{\mathrm{cr}}v_{\mathrm{sim}}}{c_0} \tag{3.3}$$

which corresponds to the Doppler shift that the signal would experience if it were reflected from a dynamic real-world target.

The target's RCS is simulated through attenuation or amplification of the incoming radar signal. The signal power at the receiver of an RTS system at a

distance of R_c from the RuT and with a receive and transmit antenna gain of G_{fe} is

$$P_{rts,rx} = \frac{P_{tx} G G_{fe} G_{rts} \lambda^2}{(4\pi)^2 {R_c}^2} \tag{3.4}$$

Within the RTS an artificial power gain G_{rts} is applied and subsequently the signal is re-transmitted towards the RuT where the signal power at the receiver can be expressed as

$$P_{rx} = \frac{P_{tx} G^2 {G_{fe}}^2 G_{rts} \lambda^4}{(4\pi)^4 {R_c}^4} \tag{3.5}$$

The required artificial gain to simulate a virtual target with an RCS of σ_{sim} at a distance of R_{sim} can be derived when equating (3.5) with the receive power caused by a real-world target from (2.3)

$$G_{rts} = \frac{\sigma_{sim}}{{R_{sim}}^4} \frac{4\pi {R_c}^4}{{G_{fe}}^2 \lambda^2} \tag{3.6}$$

The Re-Synthesis Approach

The re-synthesis approach requires to analyze the incoming radar signal and to extract certain signal parameters, namely the chirp slope B/T_s and repetition time T_c as well as the start and stop frequency. Based on these, a new chirp signal is synthesized which is altered with regard to the frequency and amplitude modifications that are needed to simulate the velocity and RCS of a virtual target. The created artificial signal can also be a superposition of many virtual targets. The signal is synchronized in time and periodicity with the incoming radar signal and transmitted towards the RuT with a delay that corresponds to the range of the target.

3.3.2 Angle Simulation

The simulation of the angular position of the virtual radar target is independent of the range, velocity and RCS simulation approaches discussed above.

It can be realized either by mechanically rotating the RTS system centric around the RuT [ABB+21, dSP21], by rotating the sensor itself [Kon17a], or by electronically switching among multiple, spatially distributed RTS antennas [GMS+18, Key22, Roh21b]. The advantages and disadvantages of the three different concepts are discussed in section 3.5.3.

3.4 System Topology

The signal modifications required to generate virtual radar targets can be implemented in the analog or digital domain. The selection of the topology of the target generation process determines certain features of the respective RTS system such as the minimum simulatable target range, the system's scalability and the hardware costs. Furthermore, not every target generation method presented in section 3.3.1 can be implemented in either, analog or digital, domain, which presents an additional consideration to be made when designing such a system. Only the simulation of the AoA of the virtual target is independent of the selected system domain. In the following, both topologies as well as their possible realizations are presented. In chapter 3.5.1 their pros and cons are listed.

3.4.1 Analog Target Generation

The analog target generation employs discrete RF components in order to apply the required signal modifications. Using this topology, only the aforementioned modification approach with either a true-time delay [EPB16, GGS+17] or a frequency shift concept [SJM+21, IMSW19] for the simulation of the target range can be implemented. Block diagrams illustrating the basic design of an analog true-time delay and frequency shift RTS system are shown in Fig. 3.2.

When implementing the true-time delay concept for the simulation of the target range, so-called delay lines can be employed. The idea is to delay the signal by passing it through either a set of optical [EPB16, LEWW14] or coaxial cables [GGS+17] whose respective combined length correlates with the intended target range. The architecture of the delay line set can be designed in one of two ways. Either with segments of different lengths, that correspond to a power-of-two

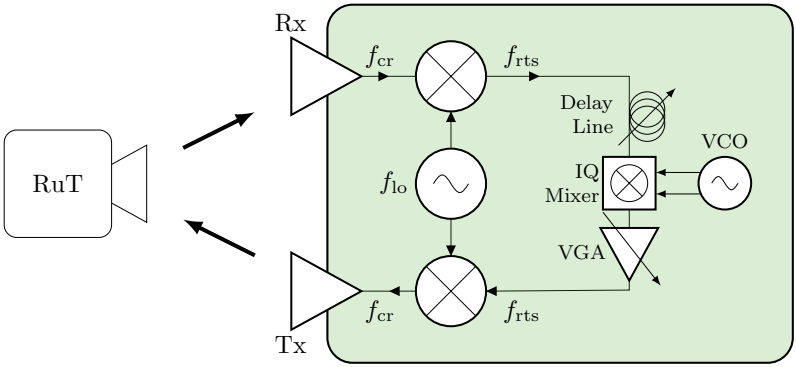

(a) True-time delay concept

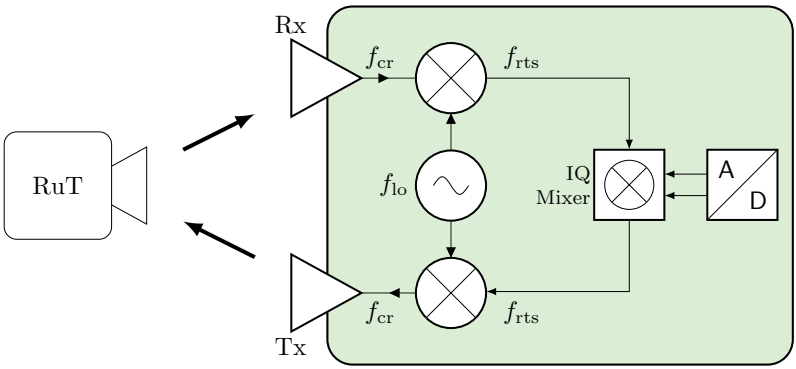

(b) Frequency shift concept

Figure 3.2: Block diagram of an analog (a) true-time delay and (b) frequency shift RTS system

series and which the signal either passes through or bypasses [LEWW14], or with segments of equal length, after each of which the signal can be branched off, with a following switch matrix to de-multiplex the multiple outputs [GGS+17]. Alternatively, a true-time delay can be induced with surface acoustic wave (SAW) filters [ALRP+17]. For the frequency shift concept, a complex-valued mixing scheme can be employed, which is realized either through an in-phase quadrature (IQ) mixer or an analog multiplier [SSGW21, RH20, IMSW19].

The analog simulation of the velocity of a virtual target can be performed either by direct frequency mixing using an IQ mixer or an analog multiplier [IRW20, GMS+18, AOHH21], similar to the frequency shift range simulation, or by introducing a slight frequency offset between the up- and down-conversion prior respectively subsequent to the other signal modifications [KHN+21].

The simulation of the RCS of a target is accomplished with variable gain amplifiers (VGA) [GGS+17] that are placed in the signal path and whose amplification is adjusted according to (3.6).

3.4.2 Digital Target Generation

For the digital generation of virtual radar targets, the incoming radar signal is digitalized prior to the application of the required modifications using an analog-to-digital converter (ADC). The digital signal samples are fed into a field programmable gate array (FPGA) or digital signal processor (DSP), which perform the signal amendments [SN20] or the signal analysis and re-synthesis [WMN+20] in accordance to the target characteristics to be simulated. Subsequently, the signal is converted back to the analog domain using a digital-to-analog converter (DAC) and re-transmitted towards the RuT. The block diagram of a digital RTS system is shown in Fig. 3.3.

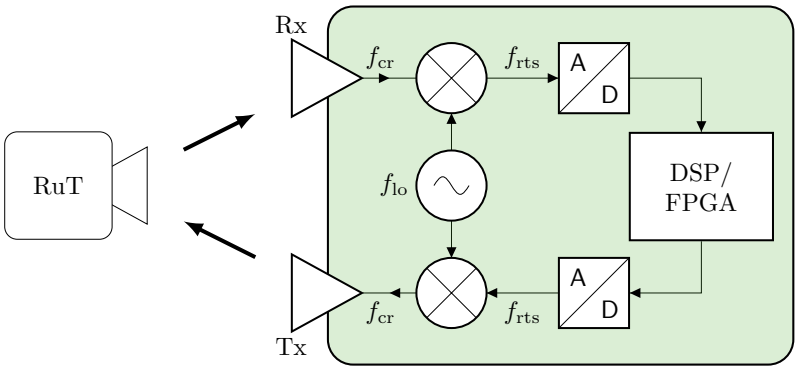

Figure 3.3: Block diagram of a digital RTS system

The digital range simulation of a virtual target is achieved through sample buffering, storing the incoming radar samples in memory and reading them back with a controllable temporal offset [SP21]. Alternatively, the range can be simulated with the re-synthesis approach by synchronizing the newly created artificial signal with the incoming radar signal in time and controlling the time shift with which it is sent back to the RuT [DMW18]. This requires a trigger mechanism that detects the arrival of a chirp to which the re-synthesized signal is then aligned.

The velocity simulation of a target is performed, in the case of the modification approach, with a digital complex-valued mixer that is often implemented as a numerical multiplier [JLH21]. The Doppler signal, that the incoming radar signal is mixed with, is generated using a direct digital synthesis (DDS) component that is capable of synthesizing signals of arbitrary frequencies [KBS+22].

The RCS of a virtual target is simulated either by a simple digital multiplication of the radar signal with an adjustable factor [SN20], or by digitally controllable VGAs in the analog signal path following the DAC [MRP07]. The two options can be combined which yields an extended dynamic range of the system.

For the re-synthesis approach, the simulation of the velocity and RCS of a virtual target is taken into account during the generation of the artificial radar signal [WMN+20].

3.5 Trade-offs

In the following, the advantages and disadvantages of the different system topologies, target generation approaches, and angle simulation concepts are elaborated.

3.5.1 System Topology

The main differences that set analog and digital RTS systems apart are the minimum simulatable target range and the scalability. Due to the implementation of the target generation process on an FPGA or DSP, digital RTSs are highly scalable. Additional virtual targets can easily be simulated through the

reconfiguration of the platform. The amount and distribution of target generation units is only limited by the available hardware resources on the FPGA or DSP employed. However, this topology is associated with the disadvantage that the radar signal experiences an inevitable delay caused by the ADC and DAC, which in turn leads to an unavoidable target range offset. Even the usage of low-latency converters results in a minimum target range in the order of tens of meters, which can be severe for the entire setup, depending on the use case. In contrast, analog RTS systems do not deploy such converters, hence very small target ranges can be achieved. Nonetheless, analog setups are not as scalable since the signal modifications needed for the target generation are realized with discrete electrical components, thus the entire analog signal path must be replicated in order to insert additional targets, which cannot be performed at run-time or even post-production.

Other differences between the two topologies concern the implementable target generation methods, their monetary cost, and the physical space consumption. Analog RTSs can only realize the modification approach, that is the true-time delay and the frequency shift concept. The analysis and parameter extraction, that is needed for the generation of an artificial radar signal in the re-synthesis approach, requires signal processing steps that can only be performed in the digital domain [DMW18]. With a digital RTS system, on the other hand, all of the target generation methods mentioned above can be realized. Another consideration to be made is that the acquisition cost of a high-performance FPGA or DSP, along with high-speed ADCs and DACs, exceeds the price of the relatively cheap electrical components of an analog RTS. However, the latter is by far more space consuming due to the large spatial extent of the delay lines.

In order to combine the benefits of both system topologies, there have been efforts to build a hybrid system that splits the incoming radar signal after the down-conversion and feeds it into an analog and digital RTS in parallel [GSG+18]. Subsequent to the signal modification of the respective target generation units, the signal is recombined and transmitted back to the radar.

3.5.2 Target Generation Methods

The selection of the target generation methodology, that is the re-synthesis and the modification approach, the latter of which in turn can be divided into the

true-time delay and the frequency shift concept, has major implications on the capabilities and performance of the RTS system. In the following, these three target generation concepts are compared with regards to system topologies that can be used to realize them, processable radar modulation schemes, scalability, and minimum simulatable target range.

Analysis & Re-Synthesis

The re-synthesis approach does not have any limitations regarding the minimum target range that can be simulated. Once the generated artificial signal is synchronized in time with the incoming radar signal, its transmission towards the RuT can be performed with an arbitrary time shift, which can even be negative. Furthermore, through the superposition of multiple generated artificial signals, a multitude of virtual radar targets can be created whose number is only limited by the digital hardware resources of the implementing system [WMN+20]. On the downside, the approach can only be realized on a digital RTS setup, as mentioned before. Additionally, it only complies with FMCW or chirp sequence radar sensors, which have a constant pulse repetition period and an invariant frequency slope. This might present an exclusion criterion for future-proof RTS systems, since upcoming radar sensors will possibly employ all-digital modulation schemes [GdONA+22, WS14, SGR+21]. Moreover, at least the first chirp of each measurement is lost, since it is needed for analysis and the extraction of the chirp parameters for the subsequent signal re-synthesis. Lastly, the velocity simulation of a target poses a problem, since the phase at the beginning of each chirp is random, which cannot be compensated by the generated artificial signal.

Frequency Shift

The frequency shift approach is also not limited regarding the minimum simulatable target range, since the utilized frequency to alter the incoming radar signal can be chosen freely. Scalability does not present an issue either, because multiple frequency shift alterations can be applied simultaneously through an analog multiplier. The number of targets that can be simulated is again only limited by the digital hardware resources that create the mixing signal. Even though the approach can be implemented using either system topology, only an

analog realization makes sense, since the conversion to and from the digital domain is associated with the aforementioned drawbacks and in this case a digital implementation offers no advantages over the former. Like the previous target generation approach, the frequency shift concept is only applicable to FMCW and chirp sequence radars and also requires knowledge of the chirp parameters a priori. In addition, the concept is susceptible to the unintended generation of ghost targets that result from non-idealities in the mixing process. IQ imbalances cause a frequency shift in the negated direction and thus create targets with negated range offsets. Furthermore, intermodulation products cause ghost targets at multiples or combinations of the intended target ranges.

True-Time Delay

In contrast to the two aforementioned methods, the true-time delay target generation concept is able to operate with radar signals of any modulation scheme. The signal modifications performed are in accordance with the alterations that the emitted radar signal would undergo in reality and therefore are not specific to FMCW or chirp sequence. The concept can be implemented using either system topology, but each entails limitations. The analog-to-digital and subsequent digital-to-analog conversion required for the digital implementation introduces an inescapable signal latency and thus determines the minimum simulatable target range. The use of low-latency converters can mitigate but not completely avoid this effect. In the analog implementation, the scalability is constrained, since the signal modifications are performed in distinct signal paths that employ discrete electrical components and must be replicated for each additional virtual target. Finally, the approach is subject to a rasterization of the simulatable target range, which is driven by the smallest delay increment of the target generation. The limitations of this particular handicap can be overcome in digital RTS systems by a new technique presented in chapter 5.

3.5.3 Angle Simulation

In the following, the advantages and disadvantages of three different target angle simulation concepts are discussed. For the first concept, the RuT is mounted on a gimbal, that is a motorized cardanic suspension, and the inclination of the sensor is changed in accordance to the target angle to be simulated. This

presents a high-precision and low-cost solution, but is, however, only capable to simulate a single independently moving angle. Therefore, the concept is only applicable to end-of-line testing of radar sensors, but not to the validation of ADAS functions.

In the second concept, the RTS system, or more specifically, its receive and transmit antennas, are moved centrically around the RuT using a mechanical sledge traveling in a semicircle. This also allows a high-precision simulation of the target angle and furthermore enables the realization of multiple independently laterally moving virtual targets. However, due to the possible mutual obstruction and occlusion, the number of targets is limited. Moreover, the travel speed of the sledge constraints the lateral velocity of virtual targets.

For the third concept, the receive and transmit antennas of the RTS system are distributed statically in a hemispheric formation around the RuT. The lateral movement of a virtual target is realized through electronically switching among the antennas. This represents the only of the three solutions capable of simulating complex traffic scenarios that consist of a large number of independently moving radar targets, as required for the thorough validation of autonomous driving functions. A major disadvantage of this concept is that virtual targets can only be simulated at the discrete angular positions at which the antennas of the RTS system are located. This restriction can be tackled with a new approach presented in chapter 6 that expands on the concept of spatially distributed RTS antennas and enables the simulation of radar targets at arbitrary angles.

4 Test System Setup

In this chapter the digital RTS system that was designed and implemented in the course of this work is presented. The system allowed to verify the concepts developed in this thesis, analyze their limitations and investigate unexpected phenomena. In the following, first, the basic structure of the test system, consisting of modular front ends (FEs) and a common back end based on a field programmable gate array (FPGA), as well as their individual components are explained. Hereafter, a link budget and a spectral model of the system are developed, which serve to illustrate and reason the design process. Next, the target generation process and the implementation of the signal modifications included therein, namely delay, frequency shift, phase shift and attenuation, are elaborated. Subsequently, a balance of how many resources of the FPGA were used for the implementation of the target generation unit is drawn, and an estimate of the scalability of the system with respect to the utilized platform is given. At the end of this chapter, a generic signal model is developed that analytically describes the propagation of the signal from the RuT, through the RTS and back and allows the calculation of the modification parameters required to simulate targets with desired properties.

4.1 Basic Design

The basic design of the realized RTS system consists of modular, individual FEs and a common digital back end and is shown in Fig. 4.1. As can be seen, the FEs are separated into dedicated receivers and transmitters, whereas the back end combines multiple analog-to-digital (ADC) and digital-to-analog converters (DAC), as well as target generation instances, and therefore is able to serve multiple FEs. The composition of one receiver front end, ADC, target generation instance, DAC, and transmitter front end is considered an RTS channel. The modularity of the design and the separation of front and

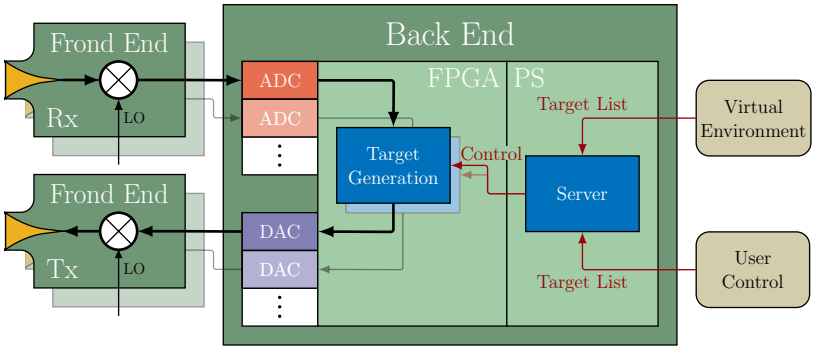

Figure 4.1: Basic design of the digital RTS system

back end enables an easy extension of the system towards a larger number of RTS channels and the free configuration of spatial distribution of the FEs. Moreover, the common back end facilitates the synchronous adjustment and mutual calibration of the individual channels, as required for the concepts presented in the work.

The receiver FE picks up the radar signal emitted by the RuT and down-converts it to an intermediate frequency f_{rts}, so that it can be digitalized by the ADC of the back end. The signal then passes through the target generation unit on the FPGA where the desired target properties are applied. The unit is controlled by a software application that is hosted by the processing system (PS) of the back end, which receives the list of targets to be generated by either a virtual environment simulation or user input. The output of the target generation unit is fed into the DAC which synthesizes the modified radar signal and passes it on to the transmitter FE, where it is up converted back to its original carrier frequency and re-transmitted towards the RuT. Front and back end of the system are connected through coaxial cables.

4.1.1 Front End

The modular FEs are divided into dedicated receivers and transmitters that receive and down-convert the radar signal emitted by the RuT or up-convert and re-transmit the signal modified by the RTS. Block diagrams of both re-

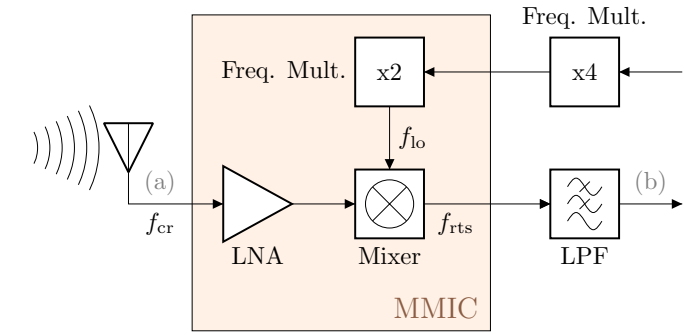

(a) Receiver front end

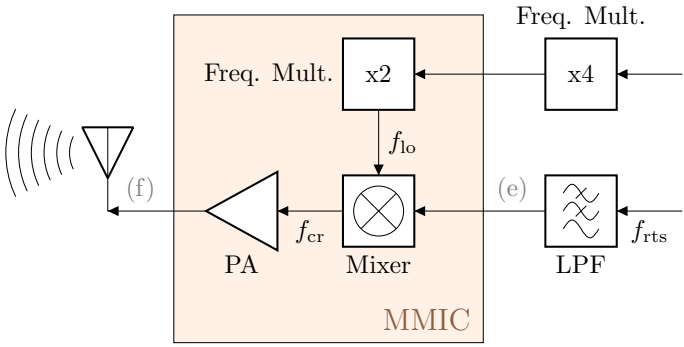

(b) Transmitter front end

Figure 4.2: Block diagram of the (a) receiver and (b) transmitter front end

ceiver and transmitter are shown in Fig. 4.2 with reference indications to the spectral model in section 4.3. The LO signal that is used for the down- respectively up-conversion of the radar signal passes through several frequency multiplication stages which allows for the signal to be fed to the FE at a much lower frequency ($f_{lo}/8$), diminishing the frequency requirements for the utilized hardware components.

The FEs are manufactured as a printed circuit board (PCB) that incorporates a Vivaldi antenna, a monolithic microwave integrated circuit (MMIC) and other electronic surface mount device (SMD) components and is housed in a metal case. The entire assembly measures only 11 mm x 35 mm x 50 mm (W x H x

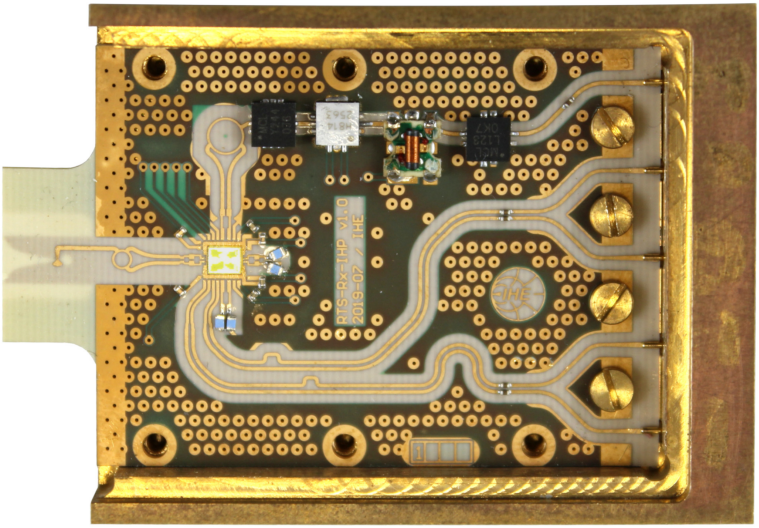

Figure 4.3: Photograph of receiver front end

L). A photograph of the FE can be seen in Fig. 4.3. Brass metal was chosen for the housing material in order to mitigate the influence of surface oxidation which can decrease the electric conductivity of the case and thus weaken the ground connection between the FE PCB and the connected coaxial cable. The PCB was realized as a compound of four copper layers separated by dielectric substrates. For the top RF layer the halogen-free, ultra-low transmission loss material R-5515 from Panasonic with a relative permittivity of $\epsilon_r = 3.09$ and a thickness of 127 µm was used [Pan21]. With this, the width of the micro strip line could be set to 313 µm to achieve a characteristic impedance of 50 Ω.

Antenna

For the reception of the radar signal emitted by the RuT and the re-transmission of the modified signal, a co-planar Vivaldi antenna was designed [Bal15]. For the realization of the antenna, all layers of the PCB except the RF substrate were cropped, which can be seen in Fig. 4.3 by the slight glow in the antenna's

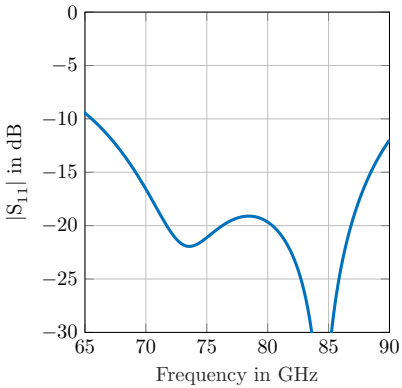

Figure 4.4: Simulated S-Parameters of the co-planar Vivaldi antenna

surrounding area. The results of the S-Parameter simulation are shown in Fig. 4.4. The wide bandwidth of the antenna supports the applicability of the RTS system for the entire automotive frequency spectrum from 76 to 81 GHz. Its poor selectivity is tolerable considering its deployment in a controlled environment without other sources of electromagnetic radiation other than the RuT. An end-fire antenna type was chosen in order to reduce the electromagnetic backscatter of the geometric structure which may be interpreted by the RuT as a static target.

RF Chip

For the down- or up-conversion of the received or modified radar signal, a transceiver MMIC provided by the Leibniz Institute for High Performance Microelectronics (IHP) was used [NHK19]. It incorporates both a receive as well as a transmit path including a low-noise amplifier (LNA) or power amplifier (PA) and an in-phase and quadrature (IQ) mixer and frequency multiplier each. As mentioned before, in order to mitigate mutual coupling and thus the generation of ghost targets, receive and transmit FEs are implemented as separate modules, which is why only the receive or transmit path of the MMIC is used. Moreover, the quadrature port of the IQ mixer was terminated and only a real-valued signal was transmitted in order to save hardware resources as will be further explained

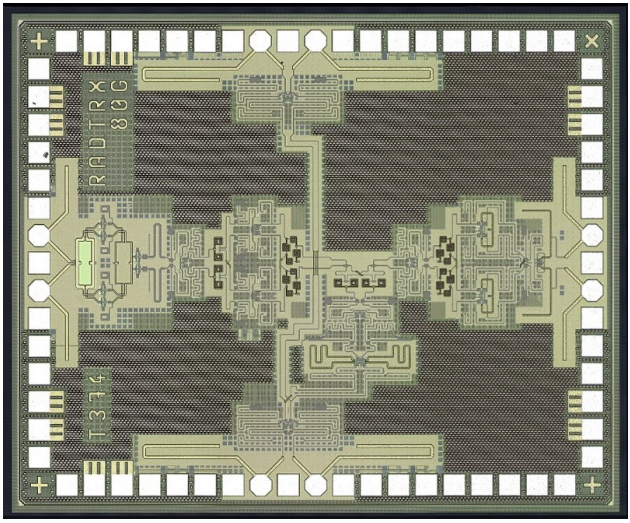

Figure 4.5: Photograph of the radar transceiver MMIC

in chapter 4.3. The chip was not originally designed for the deployment in a RTS system and could be adapted for this application. However, due to the efforts of radar chip manufacturers to integrate as many functionalities into a single MMIC as possible, the chip at hand was the best available choice at the time that provides direct access to the broadband intermediate frequency (IF) in- and output signals. The MMIC was placed in a cavity cutout of the PCB which allowed for relatively short bond wire connections. An enlarged photograph of the chip can be seen in Fig. 4.5.

4.1.2 Back End

For the digital back end of the RTS system, a ZCU111 evaluation board from Xilinx was employed, that features a Zynq UltraScale+ XCZU28DR radio frequency system on chip (RFSoC) with eight integrated high-speed ADCs and DACs [Xil18]. The Zynq SoC family from Xilinx integrates both a processing system (PS) and programmable logic (PL), in this case in the form of a quad-core Arm Cortex-A53, a dual-core Arm Cortex-R5, and an UltraScale+ FPGA. PS

Figure 4.6: Photograph of the Zynq UltraScale+ RFSoC ZCU111 evaluation board with mounted adapter board

and PL are connected to their own dedicated Double Data Rate (DDR) Random-Access Memory (RAM) that is located on the evaluation board. Advanced eXtensible Interface (AXI) connections between the PS and PL enable the control of the FPGA unit through software applications that run on the ARM processors. A custom-made adapter board that is mounted on the ZCU111 and incorporates balanced-to-unbalanced (BALUN) converters enables the access of the ADCs and DACs through SubMiniature version A (SMA) connectors. A photograph of the setup is shown in Fig. 4.6.

Analog-to-Digital Converter (ADC) & Digital-to-Analog Converter (DAC)

The eight integrated ADCs and DACs are configured to a common sampling frequency of $f_{s,rts} = 4\,\text{GHz}$. The sampling clock is generated external to the RFSoC by an on-board RF phased-locked loop (PLL). The ADCs feature a resolution of 12 bit/sample and the DACs 14 bit/Sample, which are each scaled up to 16 bit/Sample for compatibility reasons. The maximum input respectively output power of the converters is $P_{ADC} = P_{DAC} = 1\,\text{dBm}$. Since the sampling frequency exceeds the internal clock frequency of the FPGA to which the ADCs and DACs are connected to, the samples are parallelized at the digital output of the ADCs and serialized at the input of the DACs, using first-in-first-out (FIFO) buffers. The ADCs and DACs introduce an inevitable latency to the signal that passes through them, which together with other latencies of the system defines the minimum simulatable distance of a virtual radar target. Compared to others, the combined latency of ADC and DAC of $\tau_{ADC} + \tau_{DAC} = 162\,\text{ns}$ is decisive and it alone increases the minimum target range by $R_{min} \approx 24.28\,\text{m}$.

Field Programmable Gate Array (FPGA)

The UltraScale+ FPGA of the XCZU28DR RFSoc features 850 560 flip-flops (FFs), 425 280 lookup tables (LUTs), 1080 Block RAM (BRAM) blocks and 4272 digital signal processor (DSP) slices. It receives the sample data stream containing the down-converted and digitalized radar signal from the ADC, applies the target generating signal modifications and forwards it to the DAC for re-synthesis. The internal clock frequency of the FPGA is set to 500 MHz, which requires the data samples to be parallelized in groups of eight, to propagate through the PL simultaneously by means of an AXI stream interface. Consequently, each stage of the target generation unit on the FPGA must be implemented in parallel in order to avoid any backlog.

Processing System (PS)

The processing system hosts the ARM cores on which a baremetal C application is deployed. It controls the delay, frequency shift, attenuation and phase shift that the target generation unit on the FPGA applies to the radar signal. For this, it sets the corresponding registers in the PL through an AXI Lite interface.

In addition, the software application instances either a Transmission Control Protocol (TCP) or alternatively an User Datagram Protocol (UDP) webserver depending on the use case scenario. The server receives the list of targets that are to be simulated by the RTS system over an Ethernet connection from either a virtual environment simulation or user input. For this purpose, an open-source lightweight Internet Protocol (lwIP) stack is implemented which grants a resource-efficient, low-latency transfer of the target generation parameters from the user or environment simulation to the FPGA.

4.2 Dynamic Range

The exact values of the transmit power and the receiver sensitivity of a commercial radar sensor are often times not published by the radar manufacturers. However, the absolute power levels of the receive and transmit chain of the RTS system, although not entirely negligible, are not as relevant in this application and can simply be adjusted with variable gain amplifiers and attenuators during the calibration process prior to the actual RTS measurements. It must only be ensured that the signal power at the receiver of the RuT does not drive its low-noise amplifier (LNA) into compression. More important in this context is the dynamic range of the system, as it is essential in order to simulate entire traffic scenarios that may consist of a large number of targets with various reflection properties. The system must be able to generate targets with a high RCS at small distances and targets with a low RCS at large distances at the same time. The signal power attenuation caused by a target at a distance of R with an RCS of σ can be expressed as

$$A_{\mathrm{tgt}} = \frac{\sigma \lambda^2}{(4\pi)^3 R^4} \tag{4.1}$$

The dynamic range that needs to be covered by the RTS system can be determined by calculating the difference of the extremes. For instance, the weakest radar reflection that is still detectable by a commercial automotive radar is caused either by a pedestrian ($\sigma_{\mathrm{pd}} = -7\,\mathrm{dBm}^2$) at $R_{\mathrm{pd}} = 110\,\mathrm{m}$, a

moped ($\sigma_{\mathrm{mp}} = 0\,\mathrm{dBm}^2$) at $R_{\mathrm{mp}} = 170\,\mathrm{m}$ or a motorcycle ($\sigma_{\mathrm{mc}} = 5\,\mathrm{dBm}^2$) at $R_{\mathrm{mc}} = 220\,\mathrm{m}$ [Con21], which all result in a signal attenuation of

$$A_{\mathrm{tgt,max}}\big|_{\mathrm{dB}} = -158\,\mathrm{dB} \tag{4.2}$$

The strongest receive signal that may impinge on the RuT originates from a high RCS target (truck, $\sigma_{\mathrm{tr}} = 20\,\mathrm{dBm}^2$) at the minimum simulatable range of $R_{\mathrm{min}} = 25\,\mathrm{m}$ (cf. section 4.1.2) resulting in a signal attenuation of

$$A_{\mathrm{tgt,min}}\big|_{\mathrm{dB}} = -105\,\mathrm{dB} \tag{4.3}$$

With this the required dynamic range can be determined to

$$DR_{\mathrm{req}}\big|_{\mathrm{dB}} = A_{\mathrm{tgt,min}}\big|_{\mathrm{dB}} - A_{\mathrm{tgt,max}}\big|_{\mathrm{dB}} = 53\,\mathrm{dB} \tag{4.4}$$

The integrated DAC features a resolution of 14 bit and therefore a dynamic range of

$$DR_{\mathrm{DAC}}\big|_{\mathrm{dB}} \approx 6.02\,\mathrm{dB/bit} \cdot 14\,\mathrm{bit} = 84.28\,\mathrm{dB} \tag{4.5}$$

which sufficiently covers the required dynamic range of the system [PL15].

4.3 Spectral Model

In the following, the spectral model of the developed RTS system is elaborated in order to facilitate the comprehensibility of the system design decisions made and to explain the individual processing steps within the RTS signal chain. The presented system was developed for current automotive radar sensors that occupy a bandwidth of $B = 1\,\mathrm{GHz}$ at a carrier frequency of $f_{\mathrm{cr}} = 76.5\,\mathrm{GHz}$ [Con21, Rob21], but it can be easily adapted for future sensors with greater bandwidths or at different frequency bands, as only the sampling frequency of the ADCs and DACs or the LO frequency must be adjusted, respectively. The design of the RTS system is based on a double-heterodyne concept, meaning that the radar signal emitted by the RuT and received by the RTS receive antenna is down-converted in two steps; first analog to an intermediate frequency of $f_{\mathrm{rts}} = 1\,\mathrm{GHz}$ and then digitally to baseband. The up-conversion is done similar but in reverse. This two-stage process was chosen for two reasons. On the one

hand, the use of the intermediate frequency allows the signal to be digitalized and later synthesized in its real-valued representation, requiring only one ADC and DAC per RTS channel. On the other hand, the usage of the complex-valued baseband is required to generate virtual radar targets at a given velocity while suppressing ghost targets with the inverse velocity.

A diagram showing the spectral progress of the radar signal through the individual stages of the RTS system is shown in Fig. 4.7. Each plot shows the spectrum of the signal in GHz and is referenced by the block diagrams of both the front (Fig. 4.2) and back end (Fig. 4.8). The in-band amplitude slopes shown in the diagram indicate the directionality of the signal frequency band, which is of importance to the signal processing of the RuT.

Fig. 4.7a shows the frequency band of the radar signal emitted by the RuT and received by the RTS FE at $f_{\mathrm{cr}} + B/2 = 77\,\mathrm{GHz}$, and the LO signal that it is down-converted with at $f_{\mathrm{lo}} = 76\,\mathrm{GHz}$, as a Dirac impulse. Both signals are real-valued, meaning their frequency components are mirrored in the negative half of the spectrum. The resulting signal (Fig. 4.7b) features frequency components at $f_{\mathrm{rts}} = 1\,\mathrm{GHz}$ and 153 GHz, however, the latter is not output by the MMIC. In order to mitigate aliasing, the signal is filtered using an analog low-pass filter (LPF) before it is digitalized by the back end ADC. Subsequently, the signal is digitally down-converted to baseband using a digital IQ mixer and a LO frequency of $-1\,\mathrm{GHz}$, and low-pass filtered using a digital LPF. The spectrum of the emerging complex-valued signal is shown in Fig. 4.7c, with indications for the spectral repetitions at $\pm f_{\mathrm{s,rts}}/2 = \pm 2\,\mathrm{GHz}$. In the next step, the only spectrally relevant signal modification of the target generation process, that is the Doppler shift, is applied (Fig. 4.7d) and the signal is up-converted to its previous intermediate frequency of $f_{\mathrm{rts}} + f_{\mathrm{D}} = 1\,\mathrm{GHz} + f_{\mathrm{D}}$. In order to save hardware resources, thereupon only the real part of the signal is continued, which brings back the mirrored frequency component in the negative half of the spectrum depicted in Fig. 4.7e. Next, the other target signal modifications are applied and the signal is re-analogized by the DAC and once more low-pass filtered to suppress the arising spectral repetitions (Fig. 4.7f). Finally, the signal is up-converted back to its original carrier frequency and re-transmitted towards the RuT by the transmitter FE. As can be seen in Fig. 4.7g, this results in an undesired spectral component at 75 GHz in addition to the intended band at $f_{\mathrm{cr}} + B/2 = 77\,\mathrm{GHz}$. However, this presents a tolerable side effect, since the unwanted frequency component, although also received by the RuT, is directed

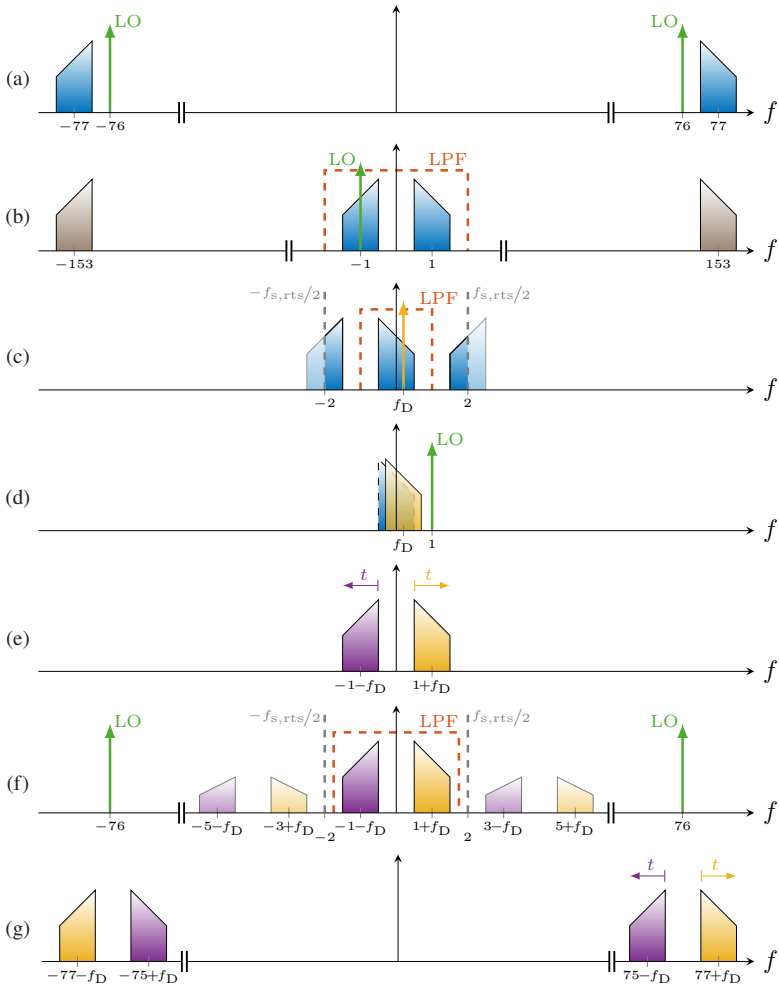

Figure 4.7: Spectral progression of the radar signal through the RTS system with all frequencies given in GHz

in the opposite frequency direction over time t and thus causes a de-chirped signal at the RuT that features a frequency slope double the steepness of the transmitted ramp

$$f_\mathrm{b} = 2f_\mathrm{rts} + 2\frac{B}{T_\mathrm{s}} \cdot t = [2, 4]\mathrm{GHz} \tag{4.6}$$

This signal component is filtered out by the LPF preceding the ADC of the RuT. Alternatively, the signal emerging from the target generation unit can also be re-analogized in its complex-valued representation using two instead of one DAC per RTS channel which avoids this behavior.

The delay, attenuation and phase shift applied by the target generation unit do not have any effect on the spectral properties of the signal and can therefore be implemented as real-valued operations. The complex-valued baseband is only needed for the application of the Doppler shift, as otherwise an additional ghost target with the inverse velocity would arise.

4.4 Target Generation

The digital target generation unit is implemented using the configurable logic blocks in the FPGA. A block diagram displaying its functional components is shown in Fig. 4.8 with references to the spectral model in chapter 4.3. The signal, after being digitalized by the ADC, is down-converted to complex baseband using a digital down-converter (DDC). Subsequent to the application of the Doppler shift, which is realized with a direct digital synthesis (DDS) component and an IQ mixer, the signal is up-converted back to f_rts using a digital up-converter (DUC). After this, the delay, phase shift and attenuation are applied before the signal is re-synthesized by the DAC. As mentioned before, the sampling frequency of the ADCs and DACs exceeds the internal clock frequency of the FPGA with which the data samples are processed, therefore all of the signal modification functions had to be implemented to process the samples in parallel. If more than one target per channel shall be generated, the signal can be split after the DDC and re-combined just before the DAC minimizing the required hardware resources.

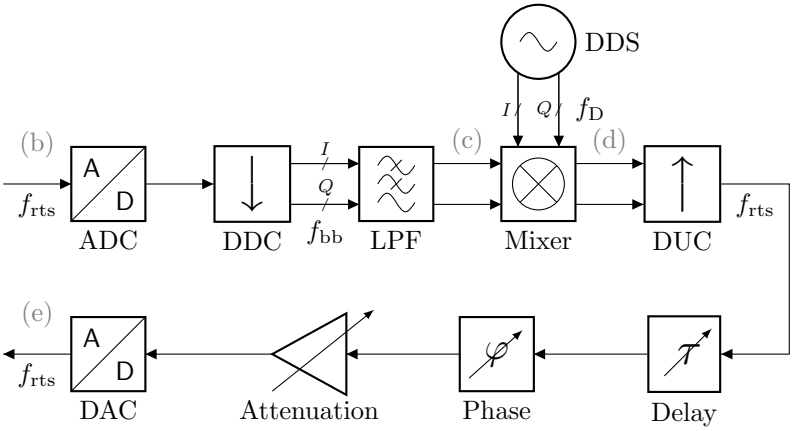

Figure 4.8: Block diagram of the back end target generation

4.4.1 Digital Up-/Down-Conversion

The digital up- and down-conversion of the signal prior and subsequent to the application of the Doppler shift, is done using an LO signal with a quarter of the sampling frequency $f_{lo,rts} = f_{s,rts}/4 = 1\,\text{GHz}$. This allows the LO signal to be sampled at exactly four cyclic instances per period, which limits its value domain to

$$s_{rts,lo} = \{1,\ j,\ -1,\ -j\} \tag{4.7}$$

This in turn enables the output of the digital converters to be expressed as

$$y = x \cdot s_{rts,lo} = \{x_I + jx_Q,\ -x_Q + jx_I,\ -x_I - jx_Q,\ x_Q - jx_I\} \tag{4.8}$$

where x describes the input signal. The real and imaginary parts of the samples are separated into two dedicated signal paths, thus the above function can be implemented by exchanging samples between the paths and flipping the sign bit of certain samples. A digital finite impulse response (FIR) filter succeeding the down-conversion is employed in order to suppress the undesired sideband. After the DUC, the imaginary signal path is terminated since for the following signal modifications the real-valued signal representation is sufficient and it

helps to save resources on the FPGA and potentially increasing the scalability of the target generation unit.

4.4.2 Range Simulation

The range simulation of the virtual target is realized by delaying the signal samples. This is done through sample buffering, meaning storing the incoming samples in on-chip BRAM blocks and reading them back a specified amount of clock cycles later. The blocks feature two read-write ports whose memory map addresses can be set individually allowing to write and read at the same time at arbitrary locations of the BRAM block. One of the ports is used only for write- and the other only for read-operations. Both ports cycle over the memory space with an address offset of

$$\eta_{\mathrm{rts}} = \tau_{\mathrm{rts}} \cdot f_{\mathrm{s,rts}} \tag{4.9}$$

between them which is determined by the desired signal delay τ_{rts} and the sampling frequency $f_{\mathrm{s,rts}}$ of the ADC and DAC. A given range is simulated by calculating the required delay according to (3.1) and setting the corresponding address offset of the ports through the PS. The smallest realizable delay increment is defined by the sampling frequency

$$\Delta\tau_{\mathrm{rts}} = \frac{1}{f_{\mathrm{s,rts}}} \tag{4.10}$$

which in turn defines the range resolution of the RTS system to

$$\Delta R_{\mathrm{sim}} = \frac{c_0}{2 f_{\mathrm{s,rts}}} = 37.47\,\mathrm{mm} \tag{4.11}$$

The maximum range that can be simulated is defined by the size of the memory space that is allocated for each RTS channel.

4.4.3 Doppler Simulation

The velocity of the virtual radar target is simulated through a complex-valued frequency shift. This is done by synthesizing an additional signal $s_{\mathrm{rts,D}}$ with

the corresponding Doppler frequency and mixing it with the radar signal. The discrete complex-valued mixing product can be expressed as

$$y = x \cdot s_{\mathrm{rts,D}} = x_{\mathrm{I}} s_{\mathrm{I}} - x_{\mathrm{Q}} s_{\mathrm{Q}} + \mathrm{j}\left(x_{\mathrm{I}} s_{\mathrm{Q}} + x_{\mathrm{Q}} s_{\mathrm{I}}\right) \tag{4.12}$$

where x describes in the input signal. As mentioned before, complex-valued signals within the FPGA are realized as two designated signal paths (real and imaginary). DSP slices are employed for the fixed point multiplication and subsequent summation of the respective signal I- and Q-parts. The required Doppler signal is created using a DDS component with an adjustable phase increment that is accumulated in the phase register which is driven by a reference clock. The register operates the address port of a LUT in which the values of a sin-function are stored. The output is the real-valued time-discrete sequence of a sin-wave whose frequency can be adjusted by setting the increment of the phase register. The imaginary part of the signal is obtained through a second output port of the DDS, whose address pointer is offset by a quarter of the wavelength.

Given the velocity of the target, the required Doppler frequency $f_{\mathrm{D,rts}}$ can by calculated according to (3.3) and the phase increment needed to synthesize the corresponding signal is

$$\Delta\varphi_{\mathrm{rts}} = 2\pi \frac{f_{\mathrm{D,rts}}}{f_{\mathrm{ref}}} \tag{4.13}$$

where f_{ref} describes the frequency of the reference clock. Since the smallest address increment is equal to one, the smallest phase increment $2\pi/N_{\mathrm{LUT}}$ is defined only by the depth of the LUT N_{LUT}, as it must always span 2π, whereas the maximum phase increment must not exceed π in order to meet the Nyquist-Shannon sampling theorem [Whi15]. Together with the reference clock frequency, the smallest phase increment determines the Doppler frequency rasterization

$$\Delta f_{\mathrm{D}} = \frac{f_{\mathrm{ref}}}{N_{\mathrm{LUT}}} \tag{4.14}$$

Given the depth of the LUT $N_{\mathrm{LUT}} = 2^{20}$ and the reference clock frequency $f_{\mathrm{ref}} = 1\,\mathrm{MHz}$, the velocity resolution of the RTS system can be derived as

$$\Delta v_{\mathrm{sim}} = \frac{c_0 f_{\mathrm{ref}}}{2 f_{\mathrm{cr}} N_{\mathrm{LUT}}} = 0.002\,\mathrm{m/s} \tag{4.15}$$

4.4.4 RCS Simulation

The RCS of a virtual target is simulated by controlling the attenuation of the radar signal. This is achieved by multiplying the incoming samples with an adjustable factor that is stored in a register and set through the PS. For the multiplication, again a DSP slice is employed. The required amplitude attenuation is defined by the RTS channel gain that is needed to simulate a virtual target with a given RCS, which can be calculated according to (3.6). The attenuation can be derived as

$$A_{\mathrm{rts}} = \sqrt{G_{\mathrm{rts}}} = \frac{\sqrt{\sigma_{\mathrm{sim}}}}{{R_{\mathrm{sim}}}^2} \cdot A_{\mathrm{cal}} \tag{4.16}$$

where A_{cal} is the channel-specific amplitude offset that is determined during the calibration process.

4.5 Resource Utilization

The resource utilization is relevant, since it allows an estimation of the scalability of the design given the available resources of the utilized FPGA platform. Table 4.1 lists the number of logic blocks that are required for the implementation of a single target generation unit and the RTS channel overhead structure. As stated before, not only does the back end feature multiple RTS channels, but also each channel may comprise of one ore more target generation units. Depending on the application it might be required to simulate multiple virtual targets whose corresponding radar echoes originate from similar angles, especially when taking advantage of the concept of arbitrary angle simulation presented in chapter 6. Therefore, Table 4.1 distinguishes between resources needed for the generation of a single target and those common for the entire channel. The items *AXI* and *Combiner* represent the configuration bus system

Table 4.1: FPGA Resource Utilization

		LUT	FF	BRAM	DSP
Channel		1313	4333	-	80
	AXI	190	141	-	-
	LPF	738	3040	-	80
	Combiner	385	1152	-	-
Target		2843	3052	4.5	48
	AXI	152	139	-	-
	Doppler	81	300	0.5	48
	Delay	458	651	4	-
	Atten.	2152	1962	-	-

and the merge unit that unifies the output signals subsequent to the individual target generation units, respectively.

Table 4.2 enumerates the resources available on the Zynq UltraScale+ XCZU28DR along with those necessary for the basic system functionality (*Fixed*), such as PS-PL interconnects and the system reset control. In addition, the number of logic blocks required to realize eight RTS channels and a total of 32 target generation units are listed. The number of channels is chosen with respect to the number of ADCs and DACs integrated on the chip. The number of target generation units is selected exemplarily to demonstrate a potential use case, where each channel may simulate up to four virtual targets simultaneously.

As can be seen, with the given parameterization, the proportionate usage lies in the low tens for all logic block types, except for the DSP, which is employed for the multiplication operations of the FIR low-pass filter (LPF) and the complex mixing of the Doppler unit. Although the DSP demand can be reduced, this comes at the cost of a drastic increase of the LUT and FF usage [dDP09], hence not necessarily more targets can be simulated. Moreover, it is not advisable to scale the design beyond a usage rate of 50 % since all radar-signal-related data paths are clocked at a high frequency close to the FPGA's maximum, making their routing time-critical and complex [Xil22].

Table 4.2: FPGA Design Scalability

	LUT	FF	BRAM	DSP
Available	425 280	850 560	1080	4272
Fixed	6222	4951	-	-
8x channel	10 504	34 664	-	640
32x target	58 976	97 664	144	1536
Total	75 702	137 279	144	2176
Usage	17.8 %	16.14 %	13.33 %	50.94 %

4.6 Signal Model

In the following, a generic signal model that analyzes the propagation of the radar signal from the RuT through the RTS system and back is presented. It further depicts the successive radar signal processing within the RuT and discloses the impact of the various RTS parameters on the target detection. The model is based on the analytical derivations of a chirp sequence radar in section 2.2.1, but is adapted in order to examine the influence of certain RTS characteristics, which in turn allows to deduce the target generation configurations required, given the properties of the real-world radar target to be simulated. As before, the model is represented mainly by its phase, with its amplitude mostly neglected. It will later be re-used and adapted for the application-specific use cases in chapter 5 and 6.

The signal emitted by the RuT and its phase can be expressed as

$$\varphi_{\mathrm{tx}}(t, n_{\mathrm{c}}) = 2\pi \left[f_{\mathrm{cr}} \cdot t + \frac{B}{2T_{\mathrm{s}}} \cdot t^2 \right] + \Phi(n_{\mathrm{c}}) \ , \qquad t \in [0, T_{\mathrm{s}}] \tag{4.17}$$

$$s_{\mathrm{tx}}(t, n_{\mathrm{c}}) = \exp\left\{ \mathrm{j}\varphi_{\mathrm{tx}}(t, n_{\mathrm{c}}) \right\} = \exp\left\{ \mathrm{j}2\pi \left[f_{\mathrm{cr}} \cdot t + \frac{B}{2T_{\mathrm{s}}} \cdot t^2 \right] + \Phi(n_{\mathrm{c}}) \right\} \tag{4.18}$$

It travels from the RuT through free space to the RTS FE, where it is received with a time delay of

$$\tau_{\mathrm{tx}} = \frac{R_{\mathrm{c}}}{c_0} \tag{4.19}$$

where R_{c} describes the physical distance between the RuT and the FEs, which is assumend to be the same for the transmit and receive paths. Subsequently, it is down-converted using an LO signal with a frequency of f_{lo}, whose phase can be described by

$$\varphi_{\mathrm{lo}}(t, n_{\mathrm{c}}) = 2\pi f_{\mathrm{lo}} \left(t + n_{\mathrm{c}} T_{\mathrm{c}}\right) \tag{4.20}$$

to an intermediate frequency of

$$f_{\mathrm{rts}} = f_{\mathrm{cr}} - f_{\mathrm{lo}} \tag{4.21}$$

Thus, the signal phase at the output of the RTS FE can be expressed as

$$\begin{aligned} \varphi_{\mathrm{rts,rx}}(t, n_{\mathrm{c}}) &= \varphi_{\mathrm{tx}}(t - \tau_{\mathrm{tx}}, n_{\mathrm{c}}) - \varphi_{\mathrm{lo}}(t, n_{\mathrm{c}}) \\ &= 2\pi \left[-f_{\mathrm{cr}}\tau_{\mathrm{tx}} + f_{\mathrm{rts}} \cdot t + \frac{B}{2T_{\mathrm{s}}}(t - \tau_{\mathrm{tx}})^2 - f_{\mathrm{lo}} \cdot n_{\mathrm{c}} T_{\mathrm{c}} \right] + \Phi(n_{\mathrm{c}}) \end{aligned} \tag{4.22}$$

Next, the signal is digitalized using the integrated ADC of the RFSoC. Therefore, the time domain is discretized using the sampling frequency $f_{\mathrm{s,rts}}$

$$t \rightarrow \frac{n_{\mathrm{rts}}}{f_{\mathrm{s,rts}}}, \qquad n_{\mathrm{rts}} \in \mathbb{N}_0 \tag{4.23}$$

where n_{rts} denotes the sample index, resulting in a signal phase at the output of the ADC of

$$\begin{aligned} \varphi_{\mathrm{rts,adc}}(n_{\mathrm{rts}}, n_{\mathrm{c}}) = 2\pi \Bigg[&-f_{\mathrm{cr}}\tau_{\mathrm{tx}} + f_{\mathrm{rts}} \cdot \frac{n_{\mathrm{rts}}}{f_{\mathrm{s,rts}}} + \frac{B}{2T_{\mathrm{s}}} \left(\frac{n_{\mathrm{rts}}}{f_{\mathrm{s,rts}}} - \tau_{\mathrm{tx}} \right)^2 \\ &- f_{\mathrm{lo}} \cdot n_{\mathrm{c}} T_{\mathrm{c}} \Bigg] + \Phi(n_{\mathrm{c}}) \end{aligned} \tag{4.24}$$

Thereupon, the Doppler shift is applied to the signal. For this, the DDS unit synthesizes a signal with a frequency of

$$f_{\mathrm{D,rts}} = \frac{2v_{\mathrm{sim}}}{\lambda} \tag{4.25}$$

that corresponds to the radial velocity of the simulated target. The synthesized signal with a phase of

$$\varphi_{\mathrm{rts,dds}}(n_{\mathrm{rts}}, n_{\mathrm{c}}) = 2\pi f_{\mathrm{D,rts}} \left(\frac{n_{\mathrm{rts}}}{f_{\mathrm{s,rts}}} + n_{\mathrm{c}} T_{\mathrm{c}} \right) \tag{4.26}$$

is mixed with the radar signal and the resulting signal phase at the output of the Doppler unit can be expressed as

$$\begin{aligned} \varphi_{\mathrm{rts,D}}(n_{\mathrm{rts}}, n_{\mathrm{c}}) &= \varphi_{\mathrm{rts,adc}}(n_{\mathrm{rts}}, n_{\mathrm{c}}) - \varphi_{\mathrm{rts,dds}}(n_{\mathrm{rts}}, n_{\mathrm{c}}) \\ &= 2\pi \left[-f_{\mathrm{cr}} \tau_{\mathrm{tx}} + (f_{\mathrm{rts}} - f_{\mathrm{D,rts}}) \frac{n_{\mathrm{rts}}}{f_{\mathrm{s,rts}}} \right. \\ &\qquad \left. + \frac{B}{2T_{\mathrm{s}}} \left(\frac{n_{\mathrm{rts}}}{f_{\mathrm{s,rts}}} - \tau_{\mathrm{tx}} \right)^2 - (f_{\mathrm{lo}} + f_{\mathrm{D,rts}}) n_{\mathrm{c}} T_{\mathrm{c}} \right] + \Phi(n_{\mathrm{c}}) \end{aligned} \tag{4.27}$$

After that, the signal is fed into the delay unit, where it is buffered for η_{rts} samples, which corresponds to a delay of

$$\tau_{\mathrm{rts}} = \frac{2R_{\mathrm{sim}}}{c_0} = \frac{\eta_{\mathrm{rts}}}{f_{\mathrm{s,rts}}}, \qquad \eta_{\mathrm{rts}} \in \mathbb{N}_0 \tag{4.28}$$

The signal phase subsequent to the delay unit can be described by

$$\begin{aligned} \varphi_{\mathrm{rts},\tau}(n_{\mathrm{rts}}, n_{\mathrm{c}}) &= \varphi_{\mathrm{rts,D}}(n_{\mathrm{rts}} - \eta_{\mathrm{rts}}, n_{\mathrm{c}}) \\ &= 2\pi \left[-f_{\mathrm{cr}} \tau_{\mathrm{tx}} - (f_{\mathrm{rts}} - f_{\mathrm{D,rts}}) \tau_{\mathrm{rts}} + (f_{\mathrm{rts}} - f_{\mathrm{D,rts}}) \frac{n_{\mathrm{rts}}}{f_{\mathrm{s,rts}}} \right. \\ &\qquad \left. + \frac{B}{2T_{\mathrm{s}}} \left(\frac{n_{\mathrm{rts}}}{f_{\mathrm{s,rts}}} - \tau_{\mathrm{tx}} - \tau_{\mathrm{rts}} \right)^2 - (f_{\mathrm{lo}} + f_{\mathrm{D,rts}}) n_{\mathrm{c}} T_{\mathrm{c}} \right] + \Phi(n_{\mathrm{c}}) \end{aligned} \tag{4.29}$$

where the number of buffered samples η_{rts} is substituted by the corresponding delay τ_{rts}. As the final step of the target generation unit, the RCS is simulated. For this, the signal is attenuated by multiplying the signal samples with a factor

that can be calculated according to (4.16) and that corresponds to the range and RCS of the target

$$s_{\mathrm{rts,A}}(n_{\mathrm{rts}}, n_{\mathrm{c}}) = A_{\mathrm{rts}} \cdot s_{\mathrm{rts},\tau}(n_{\mathrm{rts}}, n_{\mathrm{c}}) \tag{4.30}$$

Subsequently, the signal is converted back to the analog domain, re-substituting the discrete sample index with a continuous time variable

$$n_{\mathrm{rts}} \rightarrow f_{\mathrm{s,rts}} \cdot t \tag{4.31}$$

The signal phase at the output of the DAC can be expressed as

$$\begin{aligned}\varphi_{\mathrm{rts,dac}}(t, n_{\mathrm{c}}) = 2\pi \Bigg[& - f_{\mathrm{cr}}\tau_{\mathrm{tx}} - (f_{\mathrm{rts}} - f_{\mathrm{D,rts}})\tau_{\mathrm{rts}} + (f_{\mathrm{rts}} - f_{\mathrm{D,rts}}) \cdot t \\ & + \frac{B}{2T_{\mathrm{s}}}\,(t - \tau_{\mathrm{tx}} - \tau_{\mathrm{rts}})^2 - (f_{\mathrm{lo}} + f_{\mathrm{D,rts}}) \cdot n_{\mathrm{c}} T_{\mathrm{c}} \Bigg] + \Phi(n_{\mathrm{c}})\end{aligned} \tag{4.32}$$

Next, the signal is fed into the transmitter FE where it is up-converted back to its original carrier frequency using the same LO signal as before and re-transmitted towards the RuT. The signal propagates through free space and is received by the RuT with a delay of

$$\tau_{\mathrm{rx}} = \frac{R_{\mathrm{c}}}{c_0} \tag{4.33}$$

Combining the delay caused by the free space propagation to and from the RTS into a physical delay of

$$\tau_{\mathrm{c}} = \tau_{\mathrm{tx}} + \tau_{\mathrm{rx}} = \frac{2R_{\mathrm{c}}}{c_0} \tag{4.34}$$

and this in turn together with the artificial delay of the RTS into a common delay of

$$\tau = \tau_{\mathrm{c}} + \tau_{\mathrm{rts}} \tag{4.35}$$

allows to simplify the resulting signal phase at the receiver of the RuT to

$$\begin{aligned}\varphi_{\mathrm{rx}}(t, n_{\mathrm{c}}) &= \varphi_{\mathrm{rts,dac}}(t - \tau_{\mathrm{rx}}, n_{\mathrm{c}}) + \varphi_{\mathrm{lo}}(t - \tau_{\mathrm{rx}}, n_{\mathrm{c}}) \\ &= 2\pi\Bigg[- f_{\mathrm{cr}}\tau_{\mathrm{c}} - (f_{\mathrm{rts}} - f_{\mathrm{D,rts}})\tau_{\mathrm{rts}} + f_{\mathrm{D,rts}}\tau_{\mathrm{rx}} + (f_{\mathrm{cr}} - f_{\mathrm{D,rts}})t \\ &\qquad + \frac{B}{2T_{\mathrm{s}}}(t - \tau)^2 - f_{\mathrm{D,rts}} \cdot n_{\mathrm{c}}T_{\mathrm{c}}\Bigg] + \Phi(n_{\mathrm{c}})\end{aligned} \tag{4.36}$$

The beat signal is formed by down-converting the receive signal with the transmitted one which translates to a subtraction of their respective phases

$$\begin{aligned}\varphi_{\mathrm{b}}(t, n_{\mathrm{c}}) &= \varphi_{\mathrm{tx}}(t, n_{\mathrm{c}}) - \varphi_{\mathrm{rx}}(t, n_{\mathrm{c}}) \\ &= 2\pi\Bigg[\left(\frac{B}{T_{\mathrm{s}}}\tau - f_{\mathrm{D,rts}}\right) \cdot t + f_{\mathrm{D,rts}} \cdot n_{\mathrm{c}}T_{\mathrm{c}} \\ &\qquad + f_{\mathrm{cr}}\tau_{\mathrm{c}} + \left(f_{\mathrm{rts}} - f_{\mathrm{D,rts}}\right)\tau_{\mathrm{rts}} - f_{\mathrm{D,rts}}\tau_{\mathrm{rx}} - \frac{B}{2T_{\mathrm{s}}}\tau^2\Bigg]\end{aligned} \tag{4.37}$$

4.6.1 Radar Signal Processing

In the following, the radar processing of the signal returning from the RTS is elaborated. As in chapter 2.3, the expression for the phase of the beat signal is simplified using the relations in (2.17), (2.18) and (2.19) to

$$\varphi_{\mathrm{b}}(t, n_{\mathrm{c}}) = 2\pi\left[\frac{B}{T_{\mathrm{s}}}\tau \cdot t + f_{\mathrm{D,rts}} \cdot n_{\mathrm{c}}T_{\mathrm{c}} + f_{\mathrm{cr}}\tau_{\mathrm{c}} + f_{\mathrm{rts}}\tau_{\mathrm{rts}}\right] \tag{4.38}$$

Range-Doppler Estimation

Passing the signal described above through the same processing stages as in section 2.3.1 and 2.3.2 allows to express the output of the two-dimensional range-Doppler FFT as

$$\begin{aligned}s_{\mathrm{D}}(k, m) &= N_{\mathrm{s}}N_{\mathrm{c}} \cdot \mathrm{sinc}\,(B\tau - k) \cdot \mathrm{sinc}\left(f_{\mathrm{D,rts}}T_{\mathrm{m}} - m\right) \\ &\quad \cdot \exp\left\{\mathrm{j}2\pi\left[\frac{B\tau - k}{2} + \frac{f_{\mathrm{D,rts}}T_{\mathrm{m}} - m}{2} + f_{\mathrm{cr}}\tau_{\mathrm{c}} + f_{\mathrm{rts}}\tau_{\mathrm{rts}}\right]\right\}\end{aligned} \tag{4.39}$$

From this, the respective range- and Doppler cell that holds the target can be identified as

$$k_{\mathrm{det}} = B\tau \tag{4.40}$$

$$m_{\mathrm{det}} = f_{\mathrm{D,rts}} T_{\mathrm{m}} \tag{4.41}$$

which in turn enables the estimation of the range and velocity of the virtual target to

$$R_{\mathrm{det}} = k_{\mathrm{det}} \cdot \frac{c_0}{2B} = R_{\mathrm{c}} + R_{\mathrm{sim}} \tag{4.42}$$

$$v_{\mathrm{det}} = m_{\mathrm{det}} \cdot \frac{\lambda}{2T_{\mathrm{m}}} = \frac{f_{\mathrm{D,rts}}}{2}\lambda = v_{\mathrm{sim}} \tag{4.43}$$

As can be concluded from (4.42), R_{sim} must be adjusted to account for the physical distance between the RTS and RuT in order to simulate the correct target distance. In addition, R_{sim} must be calibrated for each RTS channel individually, since their respective signal path lengths within the FPGA logic may vary from another which in turn introduces differing latencies.

Angle of Arrival Estimation

Taking into account the lateral position of the FE from where the radar signal is re-transmitted towards the RuT from, the free space signal delay can be redefined as

$$\tau_{\mathrm{rx}} = \frac{R_{\mathrm{c}}}{c_0} + \frac{d_{\mathrm{A}} \sin(\theta)}{c_0} \cdot n_{\mathrm{A}} \tag{4.44}$$

where $\theta \in [-90°, 90°]$ describes the azimuth angle of the transmit FE from the perspective of the RuT. The signal phase subsequent to the range-Doppler detection can be expressed as

$$\varphi_{\mathrm{D}}(n_{\mathrm{A}}) = 2\pi \left[\left(f_{\mathrm{cr}} + \frac{B}{2} \right) \tau_0 + \left(f_{\mathrm{rts}} + \frac{B}{2} \right) \tau_{\mathrm{rts}} + \frac{d_{\mathrm{A}} \sin(\theta)}{\lambda} \cdot n_{\mathrm{A}} \right] \tag{4.45}$$

Applying Fourier beamforming and simplifying in the same manner as in section 2.4.2 results in a signal of

$$s_{\mathrm{A}}(\alpha) = N_{\mathrm{A}} \cdot \operatorname{sinc}\left(\frac{d_{\mathrm{A}}}{\lambda}\left[\sin(\theta) - \sin(\alpha)\right] N_{\mathrm{A}}\right) \cdot \exp\left\{\mathrm{j}2\pi\left[\left(f_{\mathrm{cr}} + \frac{B}{2}\right)\tau_0 + \left(f_{\mathrm{rts}} + \frac{B}{2}\right)\tau_{\mathrm{rts}} + \frac{d_{\mathrm{A}}\sin(\theta)}{\lambda}\frac{N_{\mathrm{A}} - 1}{2}\right]\right\} \tag{4.46}$$

from which the angle of the RTS FE and thus the AoA of the virtual target can be estimated

$$\sin\left(\alpha_{\mathrm{det}}\right) = \sin\left(\theta\right) \tag{4.47}$$

5 High-Precision Range Simulation

The necessity of simulating virtual radar targets at a high-precision range is not intuitively apparent. Common RTS systems are already capable of adjusting the range of virtual targets in increments in the single-digit centimeter region [SN20, GGS+17], which seems sufficient to deceive current radar senors with range resolving abilities of $\Delta R \approx 15\,\text{cm}$ [Con21, Rob21]. Moreover, given the context of automotive radar target simulation, it misleadingly appears irrelevant if a preceding vehicle is simulated with a rage offset of a few centimeters.

However, not only does the range accuracy of a modern sensor exceed its resolution and therefore must be covered by the validating system, but also will future radar sensors utilize the entire automotive radar frequency spectrum between 77 and 81 GHz [Eur08], which implies an increase of the radar signal bandwidth and thus a finer range resolution of $\Delta R \approx 38\,\text{mm}$. Moreover, real-world objects, e.g. a car, usually cause a multitude of reflections, forming so called point clouds that consist of many individual radar targets close to each other in the lateral and longitudinal domain. Therefore, RTS systems must be capable of generating multiple virtual radar targets with small radial offsets which in turn requires a fine range precision. Furthermore, fast-moving objects feature characteristics that make them too complex to be substituted by ideal virtual point targets as generated by the classical RTS approach. These objects cause a migration effect in the signal processing of a radar sensor that degrades the target detection and must be replicated for credible radar target simulation. This necessitates the capability to adjust the simulated target range seamlessly even within a measurement cycle.

The aforementioned challenges can be overcome with an improved range simulation precision. The precision at which virtual radar targets can be created by an RTS system in the range domain is driven by the rasterization at which the delay that the system applies can be adjusted. It is obvious that the smallest possible delay step limits the range simulation precision and must therefore be minimized. It also determines the update period at which the range of a virtual

target has to be re-set given its radial velocity. Updating the simulated target range within a measurement cycle at a high refresh rate allows to replicate the range migration phenomenon and enables the generation of credible virtual radar targets. The adjustment of the Doppler shift, that represents the velocity of the virtual target, does not pose an overly difficult challenge, since target velocities do not change as quickly as ranges and the components utilized for this task already possess fine rasterizations. Moreover, the synthesis of range migration inevitably leads to the same effect in the velocity domain, as will later be proven [DAN+21].

In the following, first the necessity of high-precision range simulation is substantiated which enables the synthesis of the migration phenomenon that can be observed in the presence of high-speed radar targets which are common in the automotive context. Next, the generic signal model in chapter 2.2.1 is extended in order to facilitate the comprehension of the migration phenomenon, analyze its origin and estimate its magnitude. Thereupon, a reference measurement conducted with a magnetic sledge is presented that verifies the preceding analytical elaborations. After that, the range increment and update rate required to synthesize the migration effect in radar target simulation is examined and realized using fraction delay filter. Subsequently, a verification measurement is shown that validates the successful implementation of the migration synthesis in the RTS system. Finally, some practical considerations are given.

5.1 Migration Phenomenon

Conventional range-Doppler processing with a coherent processing interval as described in chapter 2.3 implicitly assumes that the range change of a dynamic target within one measurement period due to its radial speed is less than the range resolution. The same is adopted for the velocity estimation, that is subject to a spread caused by the dependence of the Doppler shift on the instantaneous frequency. The migration phenomenon describes the spread of a single radar target over several range and Doppler bins. It is primarily known from synthetic-aperture radar (SAR) applications [PDF99], but is also gaining importance in the automotive sector, due to the continuous increase in automotive radar resolution capabilities, which pronounces the effect [XBP19].

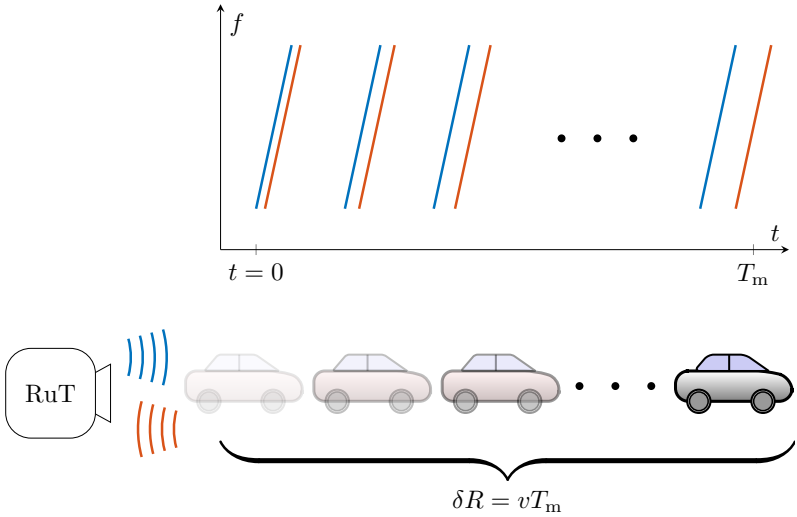

Figure 5.1: Diagram of the range migration phenomenon principle in the context of an automotive application

Fig. 5.1 shows exemplarily the principle of range migration, where the radar target travels the distance δR in the measurement time T_m. The drawing is by no means to scale and is for illustrative purposes only. As can be seen, the distance of the vehicle to the RuT increases during the measurement time, and so do the signal delay and the detected target range that is derived from each chirp. If this increase in the range δR exceeds the range resolution capability of the radar sensor ΔR, the target's peak in the range-FFT spreads over several bins and range migration can be observed. In order for this to happen, the product of the target's velocity and the measurement time must be greater than the RuT's range resolution

$$\delta R = vT_\mathrm{m} > \Delta R = \frac{c_0}{2B} \tag{5.1}$$

To prove the occurrence of the migration phenomenon in automotive radar applications and therefore the necessity to synthesize it for radar target simulation,

the minimum velocity, that is needed for the target range to migrate over a single bin, can be calculated. This can be done exemplarily for a common automotive radar sensor, whose measurement time can be derived from its velocity resolution Δv

$$T_\mathrm{m} = \frac{c_0}{2 f_\mathrm{cr} \Delta v} \tag{5.2}$$

Considering a velocity resolution of $\Delta v = 0.1\,\mathrm{m/s}$, a carrier frequency of $f_\mathrm{cr} = 77\,\mathrm{GHz}$, a radar bandwidth of $B = 1\,\mathrm{GHz}$ [Rob21] and substituting T_m in (5.1) reveals the needed velocity of

$$v > \frac{c_0}{2 B T_\mathrm{m}} = \frac{f_\mathrm{cr}}{B} \Delta v = 7.7\,\mathrm{m/s} \approx 28\,\mathrm{km/h} \tag{5.3}$$

It is understood that velocities in this order of magnitude occur on a regular bases in road traffic and thus it can be concluded that the migration phenomenon plays a role for the validation of automotive radar senors and the ADAS functions that depend on them.

5.2 Extended Chirp Sequence Signal Model

In order to facilitate the comprehension of the migration phenomenon and to unveil its analytical origin, a detailed signal model is developed. As before, the signal is represented mainly by its phase, as this neatly illustrates the various effects of the radar target. The model is based on the derivations in chapter 2.2.1,

but leaves out some of the simplifications made there. Considering (2.15), the beat signal phase can be expressed as

$$\varphi_\mathrm{b}(t, n_\mathrm{c}) = 2\pi \Bigg[\underbrace{\left(\frac{B}{T_\mathrm{s}} \tau_0 \left(1 - \frac{2v}{c_0}\right) + \overbrace{f_\mathrm{cr} \frac{2v}{c_0}}^{\text{Range-Doppler coupling}} \right) \cdot t}_{\text{Range estimation}} + \underbrace{\left(\frac{2v}{c_0} \left(f_\mathrm{cr} - \frac{B}{T_\mathrm{s}} \tau_0 \right) \right) \cdot n_\mathrm{c} T_\mathrm{c}}_{\text{Velocity estimation}}$$
$$+ \left(\frac{B}{T_\mathrm{s}} \frac{2v}{c_0} \left(1 - \frac{v}{c_0}\right) \right) \cdot t^2 - \left(\frac{B}{T_\mathrm{s}} \frac{2v^2}{c_0^2} \right) \cdot (n_\mathrm{c} T_\mathrm{c})^2$$
$$+ \underbrace{\left(\frac{B}{T_\mathrm{s}} \frac{2v}{c_0} \left(1 - \frac{2v}{c_0}\right) \right) \cdot t \cdot n_\mathrm{c} T_\mathrm{c}}_{\text{Range-Doppler migration}} + \underbrace{\tau_0 \left(f_\mathrm{cr} - \frac{B}{2T_\mathrm{s}} \tau_0 \right)}_{\text{Angle of arrival estimation}} \Bigg] \tag{5.4}$$

The expression can be simplified with regard to the range-Doppler migration and the range and velocity estimation, leaving out the range-Doppler coupling and the constant phase term. The terms that depend on t^2 and ${n_\mathrm{c}}^2$ are also negligible, since they present a much smaller impact on the signal phase than the aforementioned ones. In addition, the relations in (2.17), (2.18) and (2.19) are considered to streamline the expression even further. After the discretization by the RuT's ADC, the phase can be formulated as

$$\varphi_\mathrm{b}(n_\mathrm{s}, n_\mathrm{c}) = 2\pi \left[\frac{B}{N_\mathrm{s}} \tau_0 \cdot n_\mathrm{s} + \frac{2v}{\lambda} \cdot n_\mathrm{c} T_\mathrm{c} + \frac{B}{N_\mathrm{s}} \frac{2v}{c_0} \cdot n_\mathrm{s} \cdot n_\mathrm{c} T_\mathrm{c} \right] \tag{5.5}$$

Applying the range-FFT and then simplifying in the same manner as in section 2.3.1 leads to

$$s_\mathrm{R}(k, n_\mathrm{c}) = N_\mathrm{s} \cdot \operatorname{sinc} \left(B \left(\tau_0 + \frac{2v}{c_0} \cdot n_\mathrm{c} T_\mathrm{c} \right) - k \right) \tag{5.6}$$
$$\cdot \exp \left\{ \mathrm{j}2\pi \left[\frac{2v}{\lambda} \cdot n_\mathrm{c} T_\mathrm{c} + \frac{B \left(\tau_0 + \frac{2v}{c_0} \cdot n_\mathrm{c} T_\mathrm{c} \right) - k}{2} \left(1 - \frac{1}{N_\mathrm{s}} \right) \right] \right\}$$

As can be observed, in this equation the argument of the sinc-function also holds a delay offset, that is caused by the range change of the moving target ($R_\mathrm{mig} = v \cdot n_\mathrm{c} T_\mathrm{c}$) and that increases from chirp to chirp. The detection range bin

k_{det} is subject to the influence of the chirp index n_{c}, and therefore the detected range of the last chirp differs from that of the first chirp by δR

$$k_{\mathrm{det}} = B\left(\tau_0 + \frac{2v}{c_0} \cdot n_{\mathrm{c}} T_{\mathrm{c}}\right) \tag{5.7}$$

$$\delta R = v \cdot (N_{\mathrm{c}} - 1) T_{\mathrm{c}} \approx v T_{\mathrm{m}} \tag{5.8}$$

The number of bins that the range migrates over is given by

$$N_{\mathrm{mig}} = \frac{\delta R}{\Delta R} = \frac{2BT_{\mathrm{m}}}{c_0} v \tag{5.9}$$

This number has to be considered with ±1, as the number of bins visited also depends on the position of the initial range peak within the bin.

The Doppler-FFT is applied directly to (5.5) and not subsequent to the range processing, since the FFTs can be exchanged due to the distributive law, and it is more demonstrative to show the migration effects in this representation.

$$\begin{aligned} s_{\mathrm{D}}(n_{\mathrm{s}}, m) = N_{\mathrm{c}} \cdot \mathrm{sinc}\left(\frac{2v}{\lambda} T_{\mathrm{m}}\left(1 + \frac{B}{N_{\mathrm{s}} f_{\mathrm{cr}}} \cdot n_{\mathrm{s}}\right) - m\right) \\ \cdot \exp\left\{\mathrm{j}2\pi\left[\frac{B}{N_{\mathrm{s}}}\tau_0 \cdot n_{\mathrm{s}} + \frac{\frac{2v}{\lambda} T_{\mathrm{m}}\left(1 + \frac{B}{N_{\mathrm{s}} f_{\mathrm{cr}}} \cdot n_{\mathrm{s}}\right) - m}{2}\right]\right\} \end{aligned} \tag{5.10}$$

This time, it can be witnessed that the maximum of the sinc-function depends on the sample index n_{s} and thus the detected velocity experiences a spread over multiple bins

$$m_{\mathrm{det}} = \frac{2v}{\lambda} T_{\mathrm{m}}\left(1 + \frac{B}{N_{\mathrm{s}} f_{\mathrm{cr}}} \cdot n_{\mathrm{s}}\right) \tag{5.11}$$

$$v_{\mathrm{det}} = v\left(1 + \frac{B}{N_{\mathrm{s}} f_{\mathrm{cr}}} \cdot n_{\mathrm{s}}\right) \tag{5.12}$$

with a span of

$$\delta v = \frac{B}{N_{\mathrm{s}} f_{\mathrm{cr}}} (N_{\mathrm{s}} - 1)\, v \approx \frac{B}{f_{\mathrm{cr}}} v \tag{5.13}$$

Table 5.1: Simulation radar parameters

Name	Symbol	Value
Bandwidth	B	1 GHz
Sampling rate	f_s	40 MS/s
Chirp repetition period	T_c	30 µs
Number of chirps	N_c	1024

The number of velocity bins visited equals that of the range migration in (5.9)

$$N_{\text{mig}} = \frac{\delta v}{\Delta v} = \frac{2BT_m}{c_0} v = \frac{\delta R}{\Delta R} \tag{5.14}$$

To illustrate the phenomenon and its effects, a numeric simulation was performed with the parameterization of a modern radar sensor [NXP20] shown in Table 5.1. For this, a target was simulated at an initial distance of $R = 30\,\text{m}$ and with a radial velocity of $v = 80\,\text{km/h} \approx 22.2\,\text{m/s}$. The results of the simu-

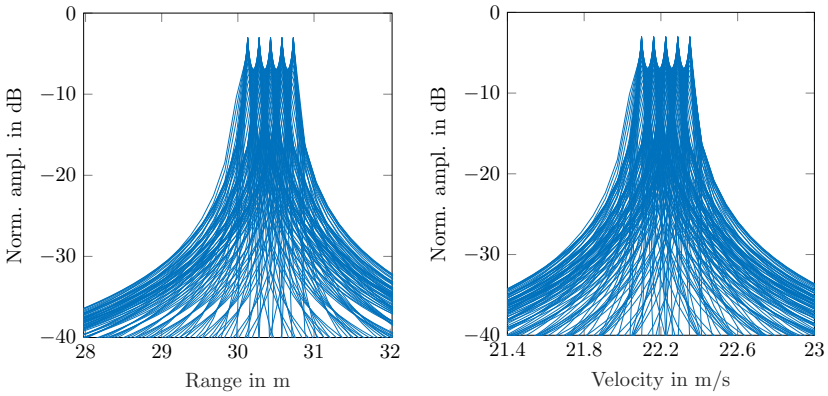

(a) Range profile

(b) Doppler profile

Figure 5.2: Simulation results of the respective one-dimensional (a) range FFT for all N_c chirps overlaid and (b) Doppler FFT for all N_s samples overlaid

lated signal after the respective one-dimensional FFTs can be seen in Fig. 5.2. In the range respectively Doppler profile, each trace corresponds to a chirp respectively a sample. The number of bins that the target migrates over can be calculated to $N_{\text{mig}} = 4.55$, which is consistent with the range and Doppler profile plots.

5.3 Reference Measurement

In order to validate the effect of the migration phenomenon, a reference measurement with a moving radar target was conducted and published in [DAN+21].

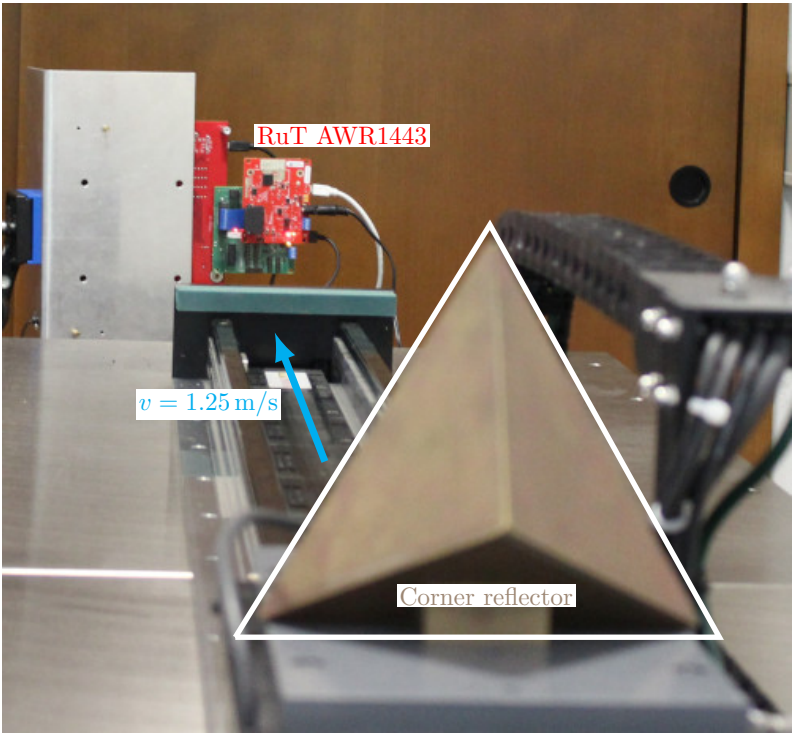

Figure 5.3: Photograph of migration reference measurement setup © 2021 IEEE [DAN+21]

For this, a corner reflector was mounted onto a sledge that moves along a linear magnetic rail and that was accelerated to $v = 1.25\,\mathrm{m/s}$. As the RuT, a Texas Instruments AWR1443BOOST radar sensor evaluation module was employed, which transmitted a chirp sequence signal with a bandwidth of $B = 1\,\mathrm{GHz}$ at a carrier frequency of $f_{\mathrm{cr}} = 77\,\mathrm{GHz}$. Since the maximum velocity of the sledge and the number of chirps were limited, the chirp repetition period was extended beyond what is typical for an automotive sensor to $T_{\mathrm{c}} = 1.25\,\mathrm{ms}$, in order to increase the measurement time T_{m}, and therefore to be able to showcase the migration phenomenon. Since the velocity of the sledge exceeded the maximum velocity resulting from the parameterization chosen ($v_{\max} = \frac{c_0}{4 f_{\mathrm{cr}} T_{\mathrm{c}}}$), the unambiguous interval of the velocity estimation was shifted to $[v_{\max}, 3v_{\max}]$. The number of chirps was set to $N_{\mathrm{c}} = 240$. A photograph of the measurement setup is displayed in Fig. 5.3.

The results of the measurement are depicted in Fig. 5.4. Again, each trace corresponds to a chirp respectively a sample in the range respectively Doppler profile. It can be clearly seen that in both the range and Doppler profile the target migrates over several bins. The additional peaks in the range plot can be attributed to the metallic frame of the sledge and the cable routing that cause unwanted reflections. According to (5.9), the expected number of bins

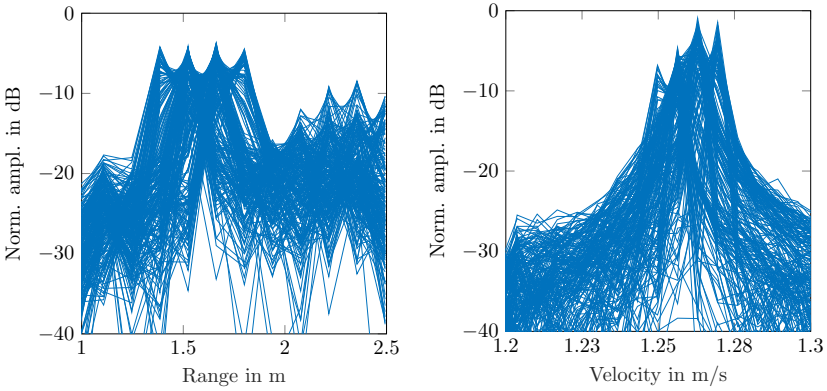

(a) Range profile

(b) Doppler profile

Figure 5.4: Measurement results of the respective one-dimensional (a) range FFT for all N_{c} chirps overlaid and (b) Doppler FFT for all N_{s} samples overlaid © 2021 IEEE [DAN+21]

over which the target travels can be calculated to $N_{\mathrm{mig}} = 2.5$, which is in agreement with the measurement results, considering N_{mig} has to be adjusted by ± 1 depending on the position of the initial range and velocity peak within the respective occupied bin.

5.4 High-Precision Radar Target Range Simulation

From the findings above, it can be concluded that RTS systems are required to create virtual radar targets with a high range accuracy. In the following, an extended signal model that is based on that of a generic RTS in chapter 4.6 is developed. It demonstrates how synthetic radar targets can be generated with a fine discretization in the range domain and allows an investigation of the update rate needed at which the target range has to be adjusted. As will later be shown, the delay increment that defines the smallest possible range offset undercuts the capabilities of sample buffering, for which reason fractional delay filters are introduced. Finally, the results of a measurement campaign are presented that verify the practical functionality of the proposed scheme.

5.4.1 Signal Model

Referring to (4.29), the artificial delay applied by the RTS back end is re-defined as

$$\tau_{\mathrm{rts}} = \tau_{\mathrm{rts},0} + \tau_{\mathrm{u}} \tag{5.15}$$

to consist of a constant part

$$\tau_{\mathrm{rts},0} = \frac{\eta_{\mathrm{rts},0}}{f_{\mathrm{s,rts}}}\,, \qquad \eta_{\mathrm{rts},0} \in \mathbb{N}_0 \tag{5.16}$$

with the index of the sample delay $\eta_{\mathrm{rts},0}$ and a dynamic one that represents the target's range change during the measurement

$$\tau_{\mathrm{u}} = \frac{2R_{\mathrm{u}}}{c_0} = \frac{2v_{\mathrm{sim}}}{c_0} \cdot n_{\mathrm{u}} T_{\mathrm{u}} \tag{5.17}$$

where T_u describes the range update period and $n_\mathrm{u} \in [0, N_\mathrm{u} - 1]$ the update index. This leads to a sample delay of

$$\begin{aligned}\eta_\mathrm{rts} &= \tau_\mathrm{rts} f_\mathrm{s,rts} = \left(\tau_\mathrm{rts,0} + \tau_\mathrm{u}\right) f_\mathrm{s,rts}\,, \qquad \eta_\mathrm{rts} \in \mathbb{Q}^+ \\ &= \left(\tau_\mathrm{rts,0} + \frac{2v_\mathrm{sim}}{c_0} \cdot n_\mathrm{u} T_\mathrm{u}\right) f_\mathrm{s,rts} \end{aligned} \tag{5.18}$$

Therefore, the resulting phase of the radar signal after the artificial delay has been applied can be expressed as

$$\begin{aligned}\varphi_{\mathrm{rts},\tau}(n_\mathrm{rts}, n_\mathrm{c}, n_\mathrm{u}) &= \varphi_\mathrm{rts,D}(n_\mathrm{rts} - \eta_\mathrm{rts}, n_\mathrm{c}) \\ &= 2\pi \left[-f_\mathrm{cr}\tau_\mathrm{tx} - \left(f_\mathrm{rts} - f_\mathrm{D,rts}\right)\left(\tau_\mathrm{rts,0} + \frac{2v_\mathrm{sim}}{c_0} \cdot n_\mathrm{u} T_\mathrm{u}\right) \right. \\ &\quad + \frac{B}{2T_\mathrm{s}}\left(\frac{n_\mathrm{rts}}{f_\mathrm{s,rts}} - \tau_\mathrm{tx} - \left(\tau_\mathrm{rts,0} + \frac{2v_\mathrm{sim}}{c_0} \cdot n_\mathrm{u} T_\mathrm{u}\right)\right)^2 \\ &\quad \left. + \left(f_\mathrm{rts} - f_\mathrm{D,rts}\right)\frac{n_\mathrm{rts}}{f_\mathrm{s,rts}} - \left(f_\mathrm{lo} + f_\mathrm{D,rts}\right) n_\mathrm{c} T_\mathrm{c} \right] + \Phi(n_\mathrm{c}) \end{aligned} \tag{5.19}$$

The subsequent conversion back to the analog domain and up to its original carrier frequency and the mixing with the transmit signal of the radar leads to a beat signal phase of

$$\begin{aligned}\varphi_\mathrm{b}(n_\mathrm{s}, n_\mathrm{c}, n_\mathrm{u}) = 2\pi \left[\right. &\left(\frac{B}{T_\mathrm{s}}\tau_0 - f_\mathrm{D,rts}\right) \cdot \frac{n_\mathrm{s}}{f_\mathrm{s}} + f_\mathrm{D,rts} \cdot n_\mathrm{c} T_\mathrm{c} \\ &+ \left(f_\mathrm{rts} - f_\mathrm{D,rts} - \frac{B}{T_\mathrm{s}}\tau_0\right)\frac{2v_\mathrm{sim}}{c_0} \cdot n_\mathrm{u} T_\mathrm{u} \\ &+ \frac{B}{T_\mathrm{s}}\frac{2v_\mathrm{sim}}{c_0} \cdot \frac{n_\mathrm{s}}{f_\mathrm{s}} \cdot n_\mathrm{u} T_\mathrm{u} - \frac{B}{T_\mathrm{s}}\frac{2{v_\mathrm{sim}}^2}{{c_0}^2} \cdot \left(n_\mathrm{u} T_\mathrm{u}\right)^2 \\ &+ f_\mathrm{cr}\tau_\mathrm{c} + \left(f_\mathrm{rts} - f_\mathrm{D,rts}\right)\tau_\mathrm{rts} - f_\mathrm{D,rts}\tau_\mathrm{rx} - \frac{B}{T_\mathrm{s}}\tau^2 \left. \right] \end{aligned} \tag{5.20}$$

Taking into account the relations in (2.17), (2.18) and (2.19) and $\tau_0 = \tau_c + \tau_{rts,0}$ the expression can be simplified to

$$\varphi_b(n_s, n_c, n_u) = 2\pi \left[\frac{B}{T_s}\tau_0 \cdot \frac{n_s}{f_s} + f_{D,rts} \cdot n_c T_c + f_{rts}\frac{2v_{sim}}{c_0} \cdot n_u T_u + \frac{B}{T_s}\frac{2v_{sim}}{c_0} \cdot \frac{n_s}{f_s} \cdot n_u T_u \right] \tag{5.21}$$

After the application of the range-FFT and the same simplifications used before, the signal can be represented by

$$s_R(k, n_c) = N_s \cdot \operatorname{sinc}\left(B\left(\tau_0 + \frac{2v_{sim}}{c_0} \cdot n_u T_u \right) - k \right) \cdot \exp\left\{ j2\pi \left[\frac{2v_{sim}}{\lambda} \cdot n_c T_c + \frac{B\left(\tau_0 + \frac{2v_{sim}}{c_0} \cdot n_u T_u \right) - k}{2} \left(1 - \frac{1}{N_s} \right) \right] \right\} \tag{5.22}$$

From this, the detected range bin, and therefore the estimated range can be expressed as

$$k_{det} = B\left(\tau_0 + \frac{2v_{sim}}{c_0} \cdot n_u T_u \right) \tag{5.23}$$

$$R_{det} = k_{det} \cdot \frac{c_0}{2B} = R_0 + v_{sim} \cdot n_u T_u \tag{5.24}$$

The detected range comprises of a spread $R_u = v_{sim} \cdot n_u T_u$ which is a function of the update period and index. In the following, investigations are made on how often or seldom the simulated target range has to be adjusted, and therefore how T_u has to be chosen, in order to synthesize the migration phenomenon in radar target simulation.

5.4.2 Range Update Rate Investigation

It is evident that the target range, respectively the delay, should be updated as seldom as possible in order to safe resources in the target generation unit. More frequent updates require greater memory allocation, as will be shown later.

Still, the same range change δR as that of a real target must be covered during a measurement

$$\delta R = N_\mathrm{u} T_\mathrm{u} = N_\mathrm{c} T_\mathrm{c} \tag{5.25}$$

From (5.24) it follows that the simulated target range must be updated frequently enough for every bin to be visited that the target migrates over. For this, the range increment of a single update must be less than or equal to the range bin width

$$v_\mathrm{sim} \cdot T_\mathrm{u} \leq \Delta R \tag{5.26}$$

Considering the maximum unambiguously detectable velocity of a target v_max, the following can be concluded

$$T_\mathrm{u} \leq \frac{\Delta R}{v_\mathrm{max}} = 2\frac{f_\mathrm{cr}}{B} T_\mathrm{c} \tag{5.27}$$

Setting the update period to five or ten times the chirp repetition period ($T_\mathrm{u} = 5\,T_\mathrm{c} \vee T_\mathrm{u} = 10\,T_\mathrm{c}$) as an example and thereby fulfilling this criterion yields the desired migration phenomenon of the virtual target in the range and Doppler domain, as can be seen in Fig. 5.5a and Fig. 5.5b. This time the profiles only show the maximum values of each FFT bin for all samples or chirps respectively with a marker to indicate the actual bin value to allow an easier comparison. However, choosing the update period like that also leads to spurious peaks in the Doppler profile, as can be observed in Fig. 5.5c. The number of unwanted peaks correlates to the factor by which the update period exceeds the chirp repetition time. The ideal signal according to the signal model from 5.2 is plotted as a reference.

These erroneous results can be illustratively explained by plotting the respective beat signal value and phase as a function of the chirp samples n_c and for a single time sample n_s as shown in Fig. 5.6. As can be seen, the beat signal and its phase stay constant between two range updates for the update periods of $T_\mathrm{u} \in \{5T_\mathrm{c}, 10T_\mathrm{c}\}$, which creates harmonic peaks in the frequency analysis comparable to the spectrum of a digital signal. Again, the ideal signal according to the signal model from section 5.2 is plotted as a reference.

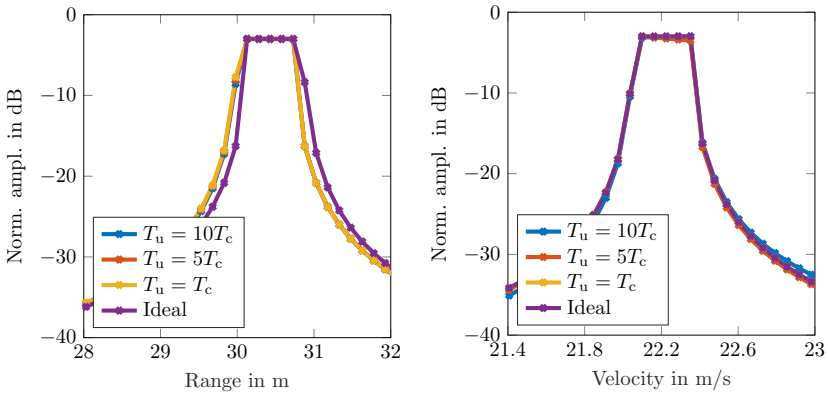

(a) Range profile close-up

(b) Doppler profile close-up

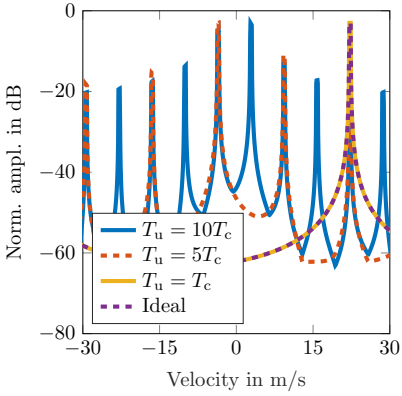

(c) Doppler profile

Figure 5.5: Range and Doppler profile simulation results for different range update periods T_u

Reducing the range update period to equal the chirp repetition time prevents any steps in the beat signal phase and thus undesired, spurious peaks in the Doppler profile. Also, from the analytical perspective this makes sense, since

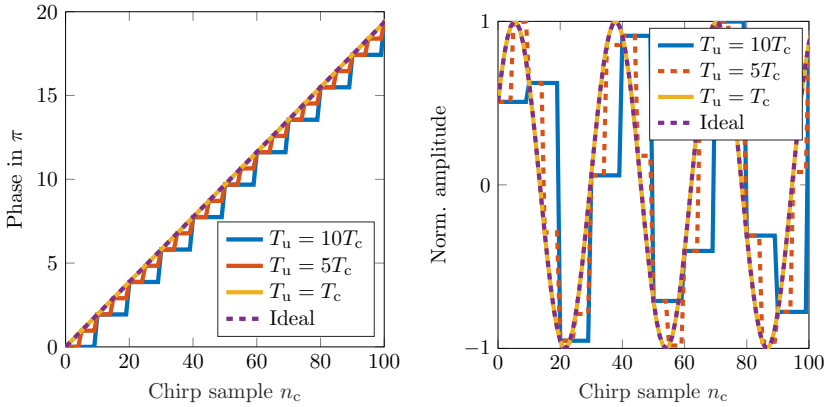

(a) Beat signal phase

(b) Beat signal value

Figure 5.6: Simulation results of the beat signal (a) phase and (b) value for different range update periods T_u

determining $T_u = T_c$ allows to streamline the expression for the detected range and velocity to

$$R_{det} = R_0 + v_{sim} \cdot n_c T_c \tag{5.28}$$

$$v_{det} = v_{sim} \left(1 + \frac{f_{rts}}{f_{cr}} + \frac{B}{N_s f_{cr}} \cdot n_s\right) \tag{5.29}$$

which largely correspond to those of the extended signal model in section 5.2. The detected velocity deviates slightly, however, this can be accounted for when setting v_{sim}.

For these reasons, it can be concluded that the simulated range and thus the applied artificial delay must be adjusted at least once per chirp. However, the update period is not limited downwards and can also be set smaller than the chirprate ($T_u \leq T_c$). The chirp repetition time can be derived from the maximum unambiguous velocity v_{max}, as this parameter is usually given in the data sheet of a commercial radar sensor. For practical reasons, it is advisable to set the update period to half of the chirp repetition time ($T_u = T_c/2$) in order to guarantee the suppression of any spurious Doppler peaks, while still limiting the resource demand.

5.4.3 Delay Increment

The delay increment that is needed to adjust the target range after every chirp ($T_u = T_c$) can be expressed as

$$\Delta\tau_u = \frac{2\Delta R_u}{c_0} = \frac{2T_c v_{sim}}{c_0} \tag{5.30}$$

Considering the necessity to synthesize range-Doppler migration for all detectable velocities, the smallest delay increment required can be calculated with $v_{sim} = v_{max}$ to

$$\Delta\tau_{u,min} = \frac{2T_c v_{max}}{c_0} = \frac{1}{2f_{cr}} \tag{5.31}$$

The smallest possible delay increment in digital RTS systems, which implement sample buffering for the range simulation, results from the sample frequency of the ADCs and is too coarse for delay steps of such fineness:

$$\Delta\tau_{rts} = \frac{1}{f_{s,rts}} > \Delta\tau_{u,min} \tag{5.32}$$

Therefore, the target generation is extended with fractional delay filters that allow the application of artificial delays, even of fractions of the sample interval.

Fractional Delay Filter

The underlying theorem for applying a delay of a fraction of the sampling period to a discrete-time signal is based on the principle that a bandlimited signal can be reconstructed exactly if it has been sampled correctly. In this context, this implies that the sample frequency must be greater than the bandwidth of the signal ($f_{s,rts} > B$) [Sha84]. The idea is to convert a time-discrete signal $s_{in}(n_{rts})$ to its time-continuous representation ($x(t)$), apply an arbitrary delay τ_{fd} and convert it back to the time-discrete domain ($s_{out}(m_{rts})$). The recon-

struction operation of the time-continuous signal can be expressed with the Whittaker–Shannon interpolation formula

$$x(t) = \sum_{n_{\mathrm{rts}}=-\infty}^{\infty} s_{\mathrm{in}}(n_{\mathrm{rts}}) \cdot \operatorname{sinc}\left(\frac{t - T_{\mathrm{s,rts}} \cdot n_{\mathrm{rts}}}{T_{\mathrm{s,rts}}}\right) \tag{5.33}$$

where $T_{\mathrm{s,rts}}$ denotes the RTS's sample interval. The continuous signal $y(t)$ is subsequently time-shifted with a fractional delay τ_{fd}

$$y(t) = x(t - \tau_{\mathrm{fd}}) = \sum_{n_{\mathrm{rts}}=-\infty}^{\infty} s_{\mathrm{in}}(n_{\mathrm{rts}}) \cdot \operatorname{sinc}\left(\frac{t - \tau_{\mathrm{fd}} - T_{\mathrm{s,rts}} \cdot n_{\mathrm{rts}}}{T_{\mathrm{s,rts}}}\right) \tag{5.34}$$

Since the time shift is applied in the continuous-time domain, the delay τ_{fd} can be adjusted steplessly. Thereafter, the signal is discretized again at equidistant time instances $t = T_{\mathrm{s,rts}} \cdot m_{\mathrm{rts}}$

$$s_{\mathrm{out}}(m_{\mathrm{rts}}) = \sum_{n_{\mathrm{rts}}=-\infty}^{\infty} s_{\mathrm{in}}(n_{\mathrm{rts}}) \cdot \operatorname{sinc}\left(\frac{T_{\mathrm{s,rts}} \cdot m_{\mathrm{rts}} - \tau_{\mathrm{fd}} - T_{\mathrm{s,rts}} \cdot n_{\mathrm{rts}}}{T_{\mathrm{s,rts}}}\right) \tag{5.35}$$

The expression can be simplified by setting $T_{\mathrm{s,rts}} = 1\,\mathrm{s}$ without loss of generality, since the actual sampling rate does not need to be fixed for a discrete-time system description [DCD11], resulting in

$$s_{\mathrm{out}}(m_{\mathrm{rts}}) = \sum_{n_{\mathrm{rts}}=-\infty}^{\infty} s_{\mathrm{in}}(n_{\mathrm{rts}}) \cdot \operatorname{sinc}\left(m_{\mathrm{rts}} - \tau_{\mathrm{fd,d}} - n_{\mathrm{rts}}\right) \tag{5.36}$$

where $\tau_{\mathrm{fd,d}} = \tau_{\mathrm{fd}}/\mathrm{s}$ describes the unit-free fractional delay. Comparing the equation to the definition of the discrete convolution, it becomes apparent that the operation can be implemented as a filter. However, the ideal fractional delay operation can not be realized since its impulse response is of infinite length. Therefore, an approximation needs to be made by using a finite impulse response (FIR) filter limiting the number of taps N_{tap} by windowing the coefficients. Additionally, the coefficients are shifted by $(N_{\mathrm{tap}} - 1)/2$ to make the filter

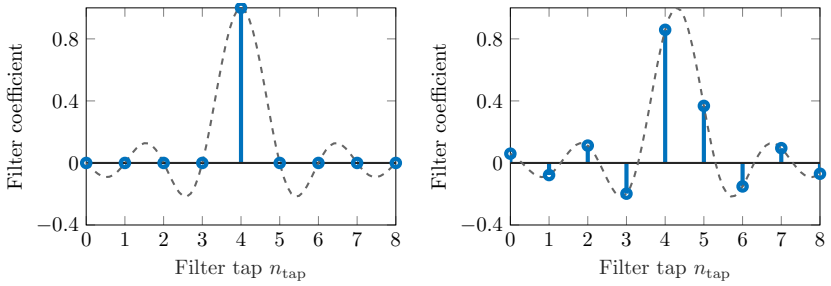

(a) $\tau_{\text{fd}} = 0$ (b) $\tau_{\text{fd}} = 0.3\,T_{\text{s,rts}}$

Figure 5.7: Simulated exemplary calculation of the fractional delay filter coefficients © 2021 IEEE [DANZ21]

causal, which in turn introduces additional latency to the signal. The coefficients can be calculated using

$$h(n_{\text{tap}}) = \text{sinc}\left(n_{\text{tap}} - \tau_{\text{fd,d}} - \frac{N_{\text{tap}} - 1}{2}\right) \tag{5.37}$$

where $n_{\text{tap}} \in [1, N_{\text{tap}}]$ is the filter tap index. Fig. 5.7 shows as an example the filter coefficients for no delay and $\tau_{\text{fd}} = 0.3\,T_{\text{s,rts}}$ with $N_{\text{tap}} = 9$ taps. As can be deduced from Fig. 5.7a, the filter introduces an additional, inherent delay of $(N_{\text{tap}} - 1)/2 = 4\,T_{\text{s,rts}}$, that deteriorates the minimum simulatable target range of the system. Prominently, the delay grows with the amount of filter taps employed, which must therefore be kept minimal.

However, reducing the number of taps causes ripples in the filter transfer function which in turn leads to a non-uniform frequency response that can inject ghost targets in the radar signal processing. Determining the number of taps of the fractional delay filter is therefore a compromise between these two considerations. Fig. 5.8 shows the frequency response of the filter for different number of taps N_{tap} and for a set delay of $\tau_{\text{fd}} = 0.5\,T_{\text{s,rts}}$, which causes the strongest fluctuations in the transfer function. The filter is designed as an all-pass filter, i.e. the bandwidth of the radar signal is smaller than the filter's cut-off frequency and thus only the transfer function and its ripples that lay within the occupied signal band are of relevance. The influence of the fluctuations can be reduced by windowing the coefficients, as is exemplarily shown in the

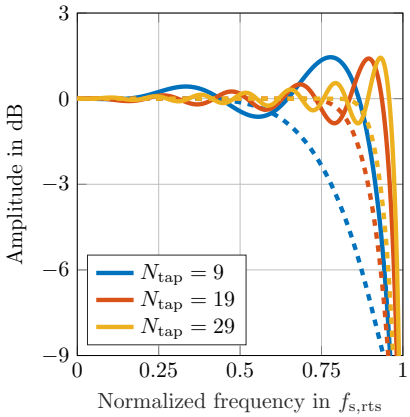

Figure 5.8: Simulated frequency response of the fractional delay filter for different number of taps N_{tap} without (solid) and with (dashed) *Blackman* window

graph for a *Blackman* window. Furthermore, the cut-off frequency itself is also dependent on the number of taps used, which has to be taken into account when designing the filter.

5.4.4 Measurement Results

In order to verify the functioning of the proposed approach to synthesize the range Doppler migration phenomenon in the context of radar target simulation, a measurement campaign was conducted and published in [DANZ21]. For this, the RTS system that is described in chapter 4 was set up in front of a Texas Instruments AWR2243BOOST radar sensor, that was utilized as the RuT, at a physical distance of $R_{\text{c}} \approx 1\,\text{m}$. A photograph of the setup of the measurement can be seen in Fig. 5.9. The receive and transmit front ends of the RTS were placed vertically aligned and behind a metal sheet that was used to block off undesired radar reflections of any structures in the background. The carrier frequency of the RTS was set to $f_{\text{rts}} = 500\,\text{MHz}$. The sensor was parameterized according to Table 5.2.

First, a reference measurement was performed for which an artificial radar target was generated with a range of $R_{\text{sim}} = 40\,\text{m}$ and a radial velocity of

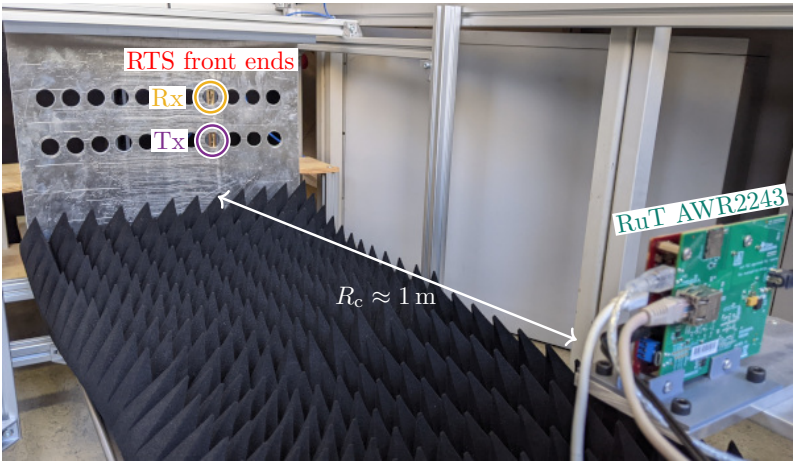

Figure 5.9: Photograph of the migration measurement setup

$v_{sim} = 25\,\mathrm{m/s}$. No fractional delay unit was employed at this time and the basic back end design presented in chapter 4.1.2 was used. The range and Doppler profiles are shown in Fig. 5.10, where it can be seen, that the virtual target occupies only a single bin in each plot. The range of the target is subject to a small offset which originates from an imperfect range calibration.

For the subsequent verification measurement, the same virtual target parameters were used, but the fractional delay unit was put in place. For this, a finite impulse

Table 5.2: Radar parameters

Name	Symbol	Value
Carrier frequency	f_{cr}	77 GHz
Bandwidth	B	1 GHz
Sampling rate	f_s	25 MS/s
Chirp repetition period	T_c	74 µs
Number of chirps	N_c	240

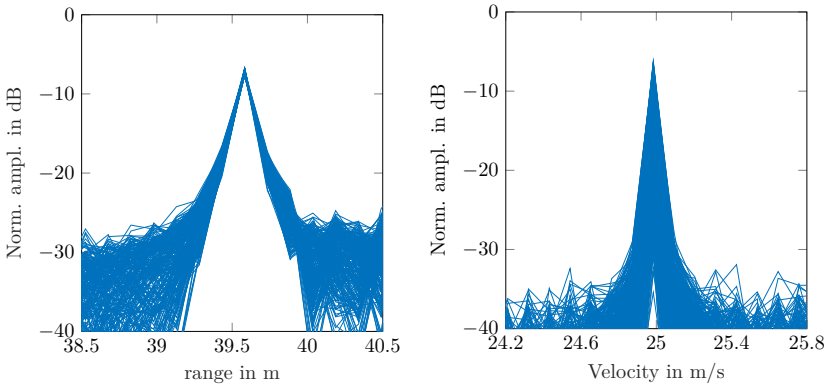

(a) Range profile

(b) Doppler profile

Figure 5.10: Measurement results of the respective one-dimensional (a) range FFT for all N_c chirps overlaid and (b) Doppler FFT for all N_s samples overlaid bypassing the fractional delay unit © 2021 IEEE [DANZ21]

response filter with $N_{tap} = 19$ taps was implemented on the RTS back end. Its adaptive design allowed the filter coefficients to be stored in the DDR memory attached to the FPGA and to be loaded at run time. The delay of the virtual target was adjusted every $T_u = T_c/2 = 37\,\mu s$, requiring a delay increment of

$$\Delta\tau_u = \frac{2\Delta R_u}{c_0} = \frac{2T_u v_{sim}}{c_0} \approx 12.33\,ps \tag{5.38}$$

This update period was chosen in accordance to the explanations in section 5.4.2. From this, the number of different fractional delays and thus the number of filter coefficient sets that were needed to generate all inter-sample delays can be calculated to

$$N_{fd} = \frac{\Delta R}{\Delta R_u} = \frac{c_0}{2BT_u v_{sim}} \approx 162 \tag{5.39}$$

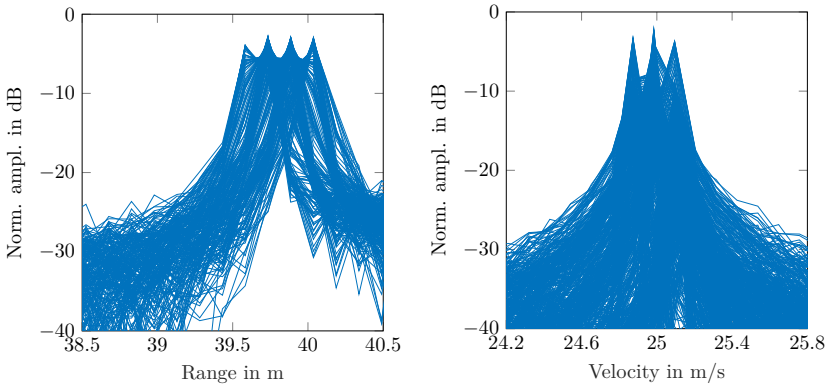

(a) Range profile

(b) Doppler profile

Figure 5.11: Measurement results of the respective one-dimensional (a) range FFT for all N_c chirps overlaid and (b) Doppler FFT for all N_s samples overlaid with the fractional delay unit in place © 2021 IEEE [DANZ21]

In this context, a coefficient set is the collection of filter coefficients required for a specific fractional delay. The filter coefficients of each set were calculated according to (5.37) with

$$\tau_{\mathrm{fd}} = n_{\mathrm{fd}} \cdot \Delta\tau_{\mathrm{u}} \,, \qquad n_{\mathrm{fd}} \in [0, N_{\mathrm{fd}} - 1] \tag{5.40}$$

and uploaded to the FPGA's DDR memory. In order to adjust the target delay, a new coefficient set is loaded from memory and substituted for the current one at the fractional delay filter. This exchange of filter coefficients is clocked at the update rate T_{u} described earlier. The results of the measurement are depicted in Fig. 5.11, where the range and Doppler profiles are shown. It can be observed that the target migrates of several bins which verifies the successful synthesis of the range-Doppler migration phenomenon. The number of visited bins can be calculated with (5.9) to $N_{\mathrm{mig}} = 3$, which stands in good agreement to the measurement results when considering the uncertainty of the exact position of the initial range and Doppler peak within the occupied bin.

5.5 Practical Considerations

As was demonstrated in this chapter, the synthesis of the migration phenomenon was successfully realized and demonstrated on a digital radar target simulation system. However, when implementing the proposed approach for a commercial solution a few practical considerations have to be taken into account.

First, the filter coefficient sets that were utilized for the measurement were generated for the particular velocity of the virtual target. Different velocities require different delay increments, thus different coefficient sets must be generated. These must be pre-computed and stored in the system's memory, since calculating them in real time is impractical given the required update frequency. One possible solution to this is to compute the coefficient sets for the smallest detectable velocity and use it as a LUT with an incremental address input whose step size can be adjusted according to the velocity of the virtual target and thus to the required update frequency. Alternatively, the fractional delay filter can be designed as a polynomial filter using the Farrow structure whose tunability allows simple handling of the coefficients and eliminates the necessity to recalculate them [Smi10].

Next, the hardware resources used to implement the fractional delay filter must be considered. The number of filter taps N_{tap} correlates with the number of complex multipliers and thus with that of DSP slices needed. As can be concluded, a compromise between quality and quantity of the fractional delay filters, meaning the filter response flatness and number of filters, must be made in order to deal with the limited resources of an FPGA. A configurable target generation unit design with a demand-driven dynamic allocation of the filters only in RTS channels with moving radar targets that show migration behavior could tackle this problem.

Finally, the adaption of the approach towards analog radar target generation demands an analog implementation of the required delay increments. Possible solutions are true-time-delay phase shifters [TMH+03], surface acoustic wave (SAW) filters [Hol74], bulk acoustic wave (BAW) filters and co-fired ceramic low-temperature (LTCC) that need to be controllable [ALP+17].

6 High-Precision Angle of Arrival Simulation

In the past, there have been essentially three techniques to simulate and control the angle of arrival of a virtual radar target generated by an RTS system. The most intuitive method is to adjust the physical angular position of the RTS channel according to the desired AoA of the target. This can be done by mechanically moving the respective FE along a circular trajectory that is centered on the position of the RuT [GR17, ABB+21, KEY, Way11]. However, this comes with the disadvantage that only a limited number of FEs, and consequently different angles, can be realized since they block each other's angular movement. Furthermore, the simulatable maximum lateral velocity of the targets is limited by the traverse speed of the mechanical setup.

The second method remedies this deficiency by rotating the RuT itself rather than the FEs [dSP22, Kon21], which allows much quicker lateral target movements. This technique, however, was developed for the application in end-of-line radar calibration tests and thus is only capable of simulating a single independent target angle and is not suited for integrated ADAS validation test procedures.

Lastly, for the third method, which this work focuses on, multiple FEs are distributed in the lateral domain and the control of the AoA of a virtual target is implemented by electronically switching between them [Key22, Roh22, VGS+21]. It enables the utilization of a high number of FEs and is therefore the only method capable to represent complex traffic scenarios as they are needed for thorough ADAS validation testing that includes current or future radar sensors. The approach allows fast lateral target movement and a large amount of virtual targets simultaneously, but comes at a high price as it requires many FE units whose hardware components are costly. Furthermore, it inevitably introduces angular deviations of the simulated AoA from its set-point, as targets can only be generated at the discrete physical angular positions at which the FEs are

located. Each virtual radar target is synthesized by a single RTS channel and its AoA is defined by the physical angular position of the corresponding FE. Consequently, the rasterization of the simulatable angle of arrival of the RTS system is driven by the lateral spacing of the FEs $\Delta\theta$. The maximum angle error occurs for a virtual radar target whose AoA ought to reside exactly between two neighboring FEs and thus equals half the FE lateral spacing ($\alpha_\epsilon = \Delta\theta/2$). Although this error can be reduced by decreasing the angular spacing of the FEs, this comes at the expense of an increased number of FEs in order to cover the same angular view span, may cause inter-pair coupling between the transmit and receive antennas of the RTS channels, and is further limited by their physical dimensions.

The new approach that is presented in this chapter overcomes these shortcomings and enables the simulation of virtual radar targets at an arbitrary angle of arrival. It is based on the method of lateral distributed FEs, which will serve as a reference for the later evaluation and will be referred to as the conventional approach in the following. By superimposing the echo signals of adjacent FEs, this new technique allows to drastically reduce the introduced angle error while at the same time reducing the number of FEs needed. It is neither limited in regards of the methodology of the RTS, as it is applicable for analog and digital systems, nor by the modulation scheme of the RuT.

In the further course of this chapter, first, the basic concept of the new approach and its advantages are explained. Next, an extended signal model based on that of a generic RTS system in chapter 4.6 is developed that facilitates the comprehension of the method and its limitations. Thereafter, the constraints of the approach and the calibrations required to satisfy them are elaborated on. Subsequently, the results of a measurement campaign that verify the functional operation and demonstrate the accomplished linearity of the technique are presented. After that, investigations regarding the angle accuracy that can be achieved in relation to the lateral spacing of the utilized FEs and the coherence properties of the respective RTS channels are exhibited, which allows to draw conclusions concerning the number of FEs needed for the overall setup. Next, the quasi-monostatic character of RTS systems, due to the physical separation of the receive and transmit antennas of the FEs, and its influence on the angle accuracy are analyzed. Finally, the approach is extended for the simulation of virtual targets in both angular domains simultaneously which makes it suitable for the application of 4D radar sensors that are capable to resolve targets in the

azimuth and elevation plane concurrently. A further measurement campaign verifies the successful implementation of the extension.

6.1 Superposition of Adjacent Echo Signals

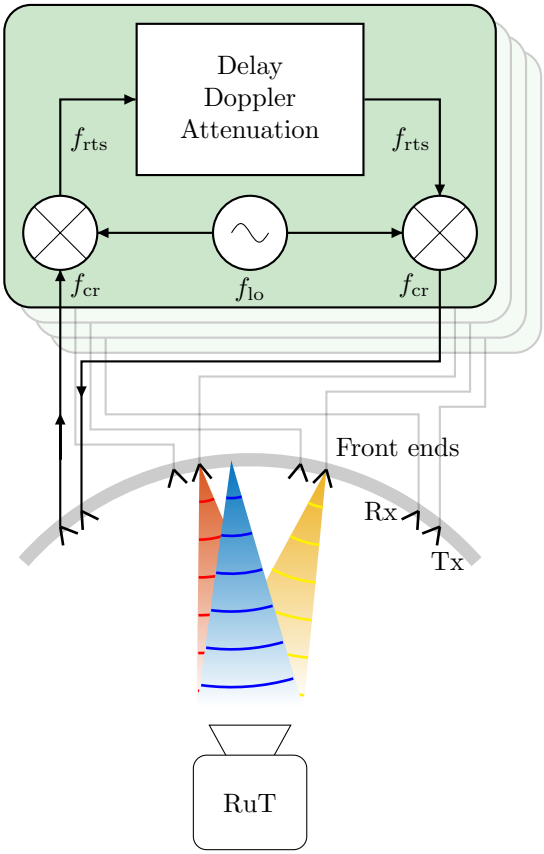

Figure 6.1: Concept of the superposition of the returning radar signals of two adjacent RTS channels (red and yellow) forming a composed virtual radar target (blue) © 2021 IEEE [DNPZ22]

The basic concept of the new approach is to superimpose the returning radar signals of two adjacent RTS channels to form a composed virtual radar target whose AoA resides between the physical angular positions of the respective RTS FEs and that can be adjusted arbitrarily. The artificial target's AoA can be controlled by the amplitude attenuation of the respective RTS channels. The concept of the approach is visualized in Fig. 6.1. It allows to strongly reduce the angle error of an RTS system, as it provides the capability to synthesize virtual targets at an arbitrary angle of arrival that lies between the corresponding FEs and at the same time decreases the number of FEs needed. In the conventional approach, the amount of FEs required could be determined by dividing the RuT's field of view by the desired angle accuracy, or respectively the FE spacing of the RTS. In contrast, with the new approach the desired angle accuracy is mostly independent of the FE spacing and thus the number of FEs only correlates with the RuT's field of view divided by its angular resolution. Detailed investigations regarding the achievable angle accuracy and the required number of FEs can be found in chapter 6.6.

6.2 Extended Signal Model

For an analytical investigation of the approach and to identify its constraints, an extended signal model was developed that is based on that of a generic RTS system in chapter 4.6. It demonstrates the capability of the concept to control the synthesized AoA through the signal attenuation of the respective RTS channels. The model focuses mostly on the signal phase since it is essential for the successful superposition of the respective radar signals to form a common virtual target, as will be shown later. For the sake of simplicity, a frequency-modulated continuous wave (FMCW) radar will be assumed. Nonetheless, the underlying principle of this approach operates independently of the modulation scheme of the radar.

Redefining the angular position of an RTS front end θ_q, formerly introduced in (4.44), to be specific for a particular RTS channel q with $q \in [1, Q]$, allows the phase shift of the antenna element n_A of the RuT to be expressed as

$$\varphi_\mathrm{A} = 2\pi \frac{d_\mathrm{A} \sin(\theta_q)}{\lambda} \cdot n_\mathrm{A} \tag{6.1}$$

where d_A denotes the antenna element spacing. Thus, the free space signal delay between a particular RTS channel q and a particular antenna element n_A can be described as

$$\tau_{\mathrm{c},q} = \tau_\mathrm{tx} + \tau_\mathrm{rx} = \frac{2R_{\mathrm{c},q}}{c_0} + \frac{d_\mathrm{A}\sin(\theta_q)}{c_0} \cdot n_\mathrm{A} \tag{6.2}$$

where $R_{\mathrm{c},q}$ is the physical distance between the specific FE and the phase center of the RuT, which are assumed to be equal for the transmit and receive paths. Furthermore, the signal attenuation and the artificial delay of a specific RTS channel are redefined as A_q and $\tau_{\mathrm{rts},q}$, respectively. These adjustments in relation to the generic RTS signal model allow the radar signal after the beamforming process to be expressed as

$$\begin{aligned} s_{\mathrm{A},q}(\alpha) = A_q \cdot N_\mathrm{A} N_\mathrm{c} N_\mathrm{s} \cdot \operatorname{sinc}\left(\frac{d_\mathrm{A}}{\lambda}\left[\sin(\theta_q) - \sin(\alpha)\right] N_\mathrm{A}\right) \\ \cdot \exp\left\{\mathrm{j}2\pi\left[\left(f_\mathrm{cr} + \frac{B}{2}\right)\tau_{0,q} + \left(f_\mathrm{rts} + \frac{B}{2}\right)\tau_{\mathrm{rts},q} + \frac{d_\mathrm{A}\sin(\theta_q)}{\lambda}\frac{N_\mathrm{A}-1}{2}\right]\right\} \end{aligned} \tag{6.3}$$

with the substitute for the invariant delay

$$\tau_{0,q} = \frac{2R_{\mathrm{c},q}}{c_0} \tag{6.4}$$

Comparing this expression to that of the generic model in (4.46) unveils that their only difference is that the phase and the shift of the sinc-function are RTS channel specific. If the virtually generated radar targets of two neighboring RTS channels ($Q = 2$) are detected in the same range and Doppler bin, their complex-valued superposition can be described as

$$\widehat{s}_\mathrm{A}(\alpha) = \sum_{q=1}^{Q} s_{\mathrm{A},q}(\alpha) = s_{\mathrm{A},1}(\alpha) + s_{\mathrm{A},2}(\alpha) \tag{6.5}$$

which in turn can be written out in full as

$$\begin{aligned}\widehat{s}_{\mathrm{A}}(\alpha) = N_{\mathrm{A}} N_{\mathrm{c}} N_{\mathrm{s}} \Bigg[& A_1 \cdot \operatorname{sinc}\left(\frac{d_{\mathrm{A}}}{\lambda}\left[\sin(\theta_1) - \sin(\alpha)\right] N_{\mathrm{A}}\right) \\ & \cdot \exp\left\{\mathrm{j}2\pi\left[\left(f_{\mathrm{cr}} + \frac{B}{2}\right)\tau_{0,1} + \left(f_{\mathrm{rts}} + \frac{B}{2}\right)\tau_{\mathrm{rts},1} + \frac{d_{\mathrm{A}}\sin(\theta_1)}{\lambda}\frac{N_{\mathrm{A}}-1}{2}\right]\right\} \\ & + A_2 \cdot \operatorname{sinc}\left(\frac{d_{\mathrm{A}}}{\lambda}\left[\sin(\theta_2) - \sin(\alpha)\right] N_{\mathrm{A}}\right) \\ & \cdot \exp\left\{\mathrm{j}2\pi\left[\left(f_{\mathrm{cr}} + \frac{B}{2}\right)\tau_{0,2} + \left(f_{\mathrm{rts}} + \frac{B}{2}\right)\tau_{\mathrm{rts},2} + \frac{d_{\mathrm{A}}\sin(\theta_2)}{\lambda}\frac{N_{\mathrm{A}}-1}{2}\right]\right\}\end{aligned} \tag{6.6}$$

This complex-valued superposition of two sinc-functions and their respective phases compose a common maximum that lies in between their individual maxima. Fig. 6.2 plots this superposition (SP) as an example for two different configurations of the RTS channel attenuations A_1 and A_2. As can be seen in the diagrams, the maximum of the superimposed function can be controlled by the amplitudes of the individual channels and reveals the AoA of the commonly formed virtual radar target. In order for the individual signals to superimpose additively, their phases must be coherent, which is explained in greater detail in

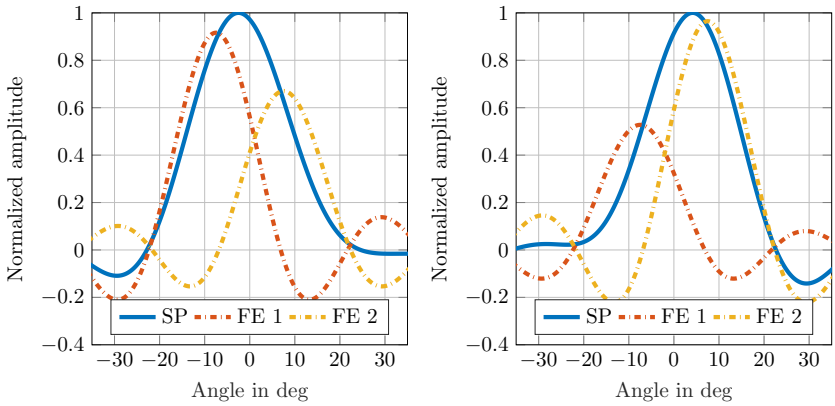

Figure 6.2: Simulation of exemplary superpositions (SPs) of two adjacent echo signals forming a common virtual radar target for two different amplitude configurations with $N_{\mathrm{A}} = 8$ and $d_{\mathrm{A}} = \lambda/2$

chapter 6.3. In the upcoming section, the quantified relationship between the individual signal amplitudes and the resulting AoA of the superimposed radar target are presented.

6.2.1 Control of Simulated Angle of Arrival

Determining the maximum of the commonly formed function $\widehat{s}_{\mathrm{A}}(\alpha)$ for a given amplitude configuration is not analytically straightforward, since the corresponding variable α is nested in two independent sinc-functions. However, to control the simulated angle of arrival only requires to calculate the amplitude configuration needed for a given target angle α_{tgt}. For this, $\widehat{s}_{\mathrm{A}}(\alpha)$ is derived according to α and set equal to zero

$$\frac{\partial \widehat{s}_{\mathrm{A}}(\alpha)}{\partial \alpha} = \frac{\partial s_{\mathrm{A},1}(\alpha)}{\partial \alpha} + \frac{\partial s_{\mathrm{A},2}(\alpha)}{\partial \alpha} = 0 \tag{6.7}$$

Since the sinc-terms of the function are only connected commutatively with each other, their derivatives can be formed individually and substituted with

$$\begin{aligned} g_q(\alpha) &= \frac{\partial \operatorname{sinc}\left(\frac{d_{\mathrm{A}}}{\lambda}\left[\sin(\theta_q) - \sin(\alpha)\right] N_{\mathrm{A}}\right)}{\partial \alpha} \\ &= \frac{\cos(\alpha)\sin\left(\pi\frac{d_{\mathrm{A}}}{\lambda}\left(\sin(\theta_q) - \sin(\alpha)\right) N_{\mathrm{A}}\right)}{\pi\frac{d_{\mathrm{A}}}{\lambda}\left[\sin(\theta_q) - \sin(\alpha)\right]^2 N_{\mathrm{A}}} \\ &\quad - \frac{\cos(\alpha)\cos\left(\pi\frac{d_{\mathrm{A}}}{\lambda}\left[\sin(\theta_q) - \sin(\alpha)\right] N_{\mathrm{A}}\right)}{\sin(\theta_q) - \sin(\alpha)} \end{aligned} \tag{6.8}$$

allowing the generic individual function's derivative to be expressed as

$$\begin{aligned} \frac{\partial s_{\mathrm{A},q}(\alpha)}{\partial \alpha} &= A_q N_{\mathrm{A}} N_{\mathrm{c}} N_{\mathrm{s}} \cdot g_q(\alpha) \\ &\quad \cdot \exp\left\{\mathrm{j}2\pi\left[\left(f_{\mathrm{cr}} + \frac{B}{2}\right)\tau_{0,q} + \left(f_{\mathrm{rts}} + \frac{B}{2}\right)\tau_{\mathrm{rts},q}\right.\right. \\ &\quad \left.\left. + \frac{d_{\mathrm{A}}\sin(\theta_q)}{\lambda}\frac{N_{\mathrm{A}} - 1}{2}\right]\right\} \end{aligned} \tag{6.9}$$

Solving (6.7) for the relation of the RTS channel amplitudes A_1/A_2 leads to

$$\frac{A_1}{A_2} = -\frac{g_2(\alpha_{\text{tgt}})}{g_1(\alpha_{\text{tgt}})} \cdot \exp\left\{ \mathrm{j}2\pi \left[\frac{d_{\text{A}}}{\lambda} \frac{N_{\text{A}} - 1}{2} \left(\sin(\theta_2) - \sin(\theta_1) \right) + \left(f_{\text{cr}} + \frac{B}{2} \right) \left(\tau_{0,2} - \tau_{0,1} \right) + \left(f_{\text{rts}} + \frac{B}{2} \right) \left(\tau_{\text{rts},2} - \tau_{\text{rts},1} \right) \right] \right\} \tag{6.10}$$

which can be utilized to determine the channel attenuations ratio for a desired angle of arrival α_{tgt} of a virtual target. To address the remaining underdetermination of the individual attenuations, the amplitude-based superposition of the signals to a common virtual radar target with a given RCS can be used

$$\sigma \sim \widehat{P} = \frac{\left(\sum_{q=1}^{Q} A_q \right)^2}{R_\Omega} = \frac{(A_1 + A_2)^2}{R_\Omega} \tag{6.11}$$

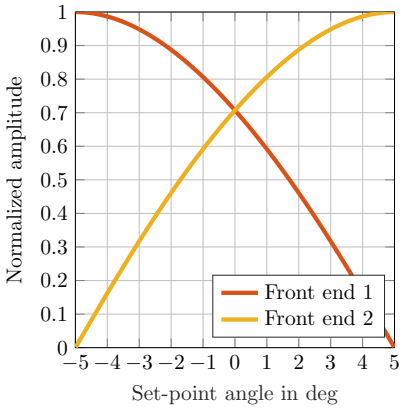

Figure 6.3: Simulation of the amplitude attenuations of the respective RTS channels over the set-point angle with an antenna configuration of the RuT of $N_{\text{A}} = 8$ and $d_{\text{A}} = \lambda/2$

where $\widehat{P}$ is the power of the superimposed radar signal and R_Ω the ohmic impedance. Fig. 6.3 shows the amplitude attenations of the respective RTS channels as a function of the set-point angle α_{tgt}.

6.3 Constraints

The successful constructive interference of the individual signals is subject to certain constraints. As mentioned before, the individual radar targets must be detected in the same range-Doppler bin, in order for the signals of the spatial-spectrum to be superimposed in the subsequent beamforming process. Additionally, the spacing of the FEs $\Delta\theta = \theta_2 - \theta_1$ and the corresponding distance between the individual signal maxima after beamforming must be small enough so that the commonly formed signal features only a single maxima. Otherwise, two individual maxima emerge which may be unintentionally detected as two angularly resolvable targets. This case is depicted exemplarily in Fig. 6.4. As can be concluded, the threshold of the FE spacing for a successful superposition correlates with the width of the sinc-function, and thus with the RuT's angle resolution. Further research on this topic is presented in chapter 6.6.

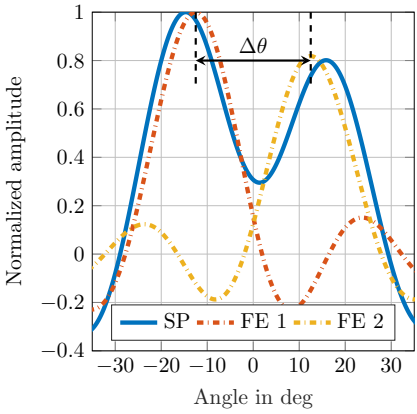

Figure 6.4: Simulated unsuccessful superposition (SP) of two adjacent echo signals forming two angular resolvable radar targets due to excessive FE spacing with $N_\text{A} = 8$ and $d_\text{A} = \lambda/2$

The next constraint is that two adjacent RTS channels can only simulate a single common target per range-Doppler bin, since the signals of multiple individual targets would be coherent in regards of phase and frequency and therefore overlay additively and form a composite target at an intermediate AoA.

Phase Coherency

A major constraint concerns the individual signals' phases. For a purely constructive superposition, the phases of the signals must be coherent, or else the signals will partially or completely cancel each other out, resulting in a distorted angle detection. For this, the individual phase controlling terms in (6.6) must be set equal leading to

$$\exp\left\{\mathrm{j}\varphi_{\mathrm{A},1}\right\} = \exp\left\{\mathrm{j}\varphi_{\mathrm{A},2}\right\} \tag{6.12}$$

with the generic phase

$$\varphi_{\mathrm{A},q} = 2\pi\left[\left(f_{\mathrm{cr}} + \frac{B}{2}\right)\tau_{0,q} + \left(f_{\mathrm{rts}} + \frac{B}{2}\right)\tau_{\mathrm{rts},q} + \frac{d_{\mathrm{A}}\sin(\theta_q)}{\lambda}\frac{N_{\mathrm{A}}-1}{2}\right] \tag{6.13}$$

From (6.12), it can be concluded that any phase difference between the two individual signals must be an integer multiple of 2π

$$\Delta\varphi = \varphi_{\mathrm{A},1} - \varphi_{\mathrm{A},2} = 2n\pi\,, \qquad n \in \mathbb{N} \tag{6.14}$$

The individual signal phases are very sensitive to variations in the physical distance $R_{\mathrm{c},q}$ between the RuT and the respective FE, hence even small inaccuracies in the mechanical mounting of the FEs $\Delta R_{\mathrm{c}} = R_{\mathrm{c},1} - R_{\mathrm{c},2}$ lead to a significant relative phase offset and potentially destructive interference of the individual signals. For example, assuming a carrier frequency of $f_{\mathrm{cr}} = 77\,\mathrm{GHz}$, a relative radial position offset of one of the FEs of only $\Delta R_{\mathrm{c}} = \lambda/4 \approx 967\,\mu\mathrm{m}$, causes an overall phase shift of $\Delta\varphi = \pi$ and the extinction of the composite signal. This is shown exemplarily in Fig. 6.5, where the detected target angle is plotted as a function of the set-point angle for different radial distance deviations ΔR_{c} and phase shifts $\Delta\varphi$. As can be seen, a distance offset of $\Delta R_{\mathrm{c}} = \lambda/2$ does not affect the detected AoA, since it corresponds to a phase shift of $\Delta\varphi = 2\pi$, which in turn has no influence on the phase coherency. Therefore, it appears as the radial distance of the FEs must only match in multiples of $\lambda/2$.

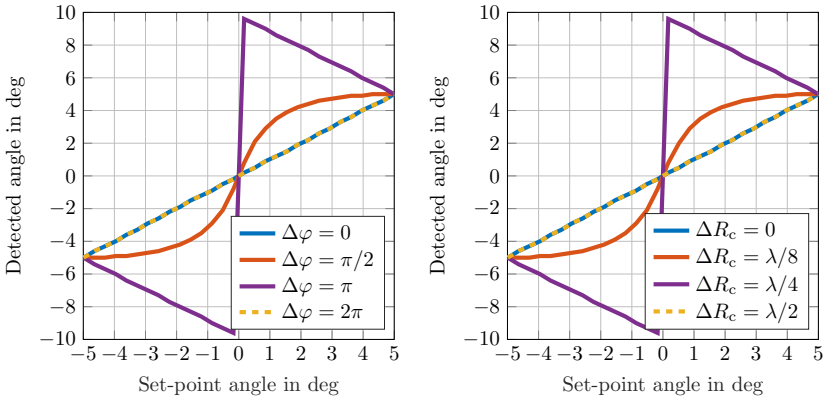

(a) Radial distance offset ΔR_c

(b) Phase shift $\Delta\varphi$

Figure 6.5: Simulation of the detected angle of arrival for different (a) radial distance offsets ΔR_c and (b) phase shifts $\Delta\varphi$ with $N_A = 8$ and $d_A = \lambda/2$

However, if the distance discrepancy ΔR_c is larger than just fractions of the wavelength, the positions of the individual maxima within the FFT bin in the range profile deviate from another. This causes the individual amplitudes to differ at the center of the FFT bin, which is used for the subsequent beamforming, leading to an error in the detected AoA, as can be seen in Fig. 6.6. Since the distance offset ΔR_c in this plot is chosen in multiples of $5\lambda \approx 19$ mm, this does not result in any phase shifts. The occurring angular error is similar to that caused by mere amplitude deviations $\Delta A = A_1 - A_2$. Since the AoA of the commonly formed radar target is controlled by the amplitude ratio of the RTS channels, any deviations in their amplitude levels will result in errors in the detected AoA. Therefore, the signal amplitudes of the involved channels must be balanced. For illustration, Fig. 6.6 also shows exemplarily the detected over the set angle for different amplitude deviations ΔA.

Since the RTS channels are under the influence of various hardware imperfections and positioning inaccuracies, it becomes clear that in order to meet these constraints and thus reduce the occurring angle error, the channels must be calibrated both in conjunction and individually with regard to delay, phase and amplitude.

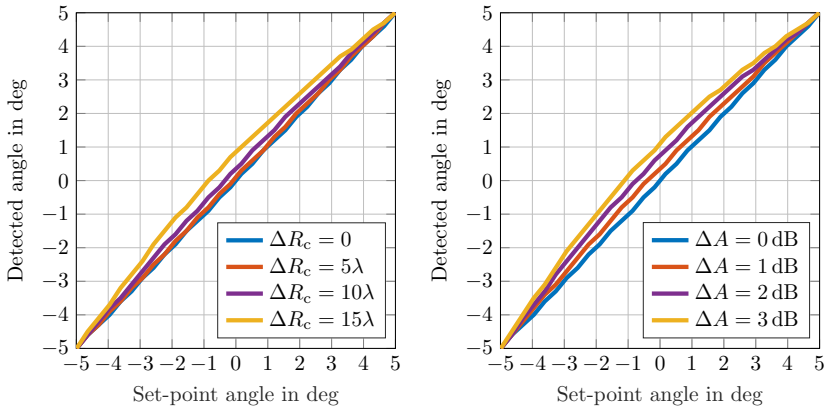

(a) Radial distance offset ΔR_c

(b) Amplitude deviation ΔA

Figure 6.6: Simulation of the detected angle of arrival for different (a) radial distance offsets ΔR_c and (b) amplitude deviations ΔA with $N_A = 8$ and $d_A = \lambda/2$

6.4 Calibration

As pointed out in the previous section, differences between the RTS channels in terms of delay, phase and amplitude cause errors in the angle detection and thus must be calibrated out. A prerequisite of the RTS system as a whole, and thus also for the calibration, is that it must be applicable for commercial radar sensors, meaning that only the data of the detected point targets after the range-Doppler FFT, the beamforming, and the subsequent detection is available [Con21, Rob21]. That is the target range, velocity, RCS and AoA.

The calibration procedure is executed in three steps, which are shown in a flow chart in Fig. 6.7. First, the physical angular positions of the FEs are measured individually. Next, in order to meet the criterion that the individual

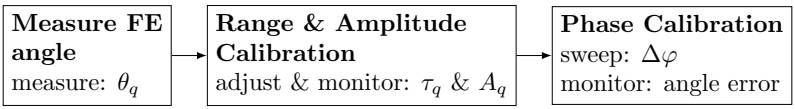

Figure 6.7: Calibration procedure flow chart

radar targets must be detected in the same range-Doppler bin, the target ranges of the respective RTS channels are measured individually and calibrated by adjusting the artificial delay $\tau_{\mathrm{rts},q}$. The same can be performed for the amplitude respectively RCS calibration using the channel attenuation A_q. Finally, a collaborative phase calibration is executed.

Phase Calibration

The calibration of the signal phase and the delay within an FFT bin presents itself as not as simple, since they are not output directly by commercial sensors. Furthermore, even if they were, such a calibration would require the signal delay respectively target range to be determined with an extremely high accuracy. However, high-precision radar range estimation down to the order of fractions of the wavelength λ, as it is required here, demands for a high signal-to-noise ratio (SNR) and can nevertheless only provide a relative rough estimate of the actual delay together with a statistical specification for its estimation accuracy, as has been shown in [Sch17a]. Therefore, the calibration is realized on the basis of the angle error, whose sensitivity to delay and phase differences can be used. Even though this method bears a certain indeterminacy and does not allow for an exact determination of the signal delay and phase, it operates in the sense of the goal of the calibration to minimize the relative phase offset and thus the angular error of the superimposed target.

The calibration is performed by monitoring the occurring angle error while sweeping the signal phase of one of the RTS channels and keeping that of the other constant. The angle error is calculated as the absolute value of the difference between set-point and actual AoA. The set-point can be chosen freely between the two respective FE positions and the required RTS channel attenuations are determined according to (6.10). The phase sweep can be executed using a phase shifter or, as (6.13) reveals, using the artificial target delay $\tau_{\mathrm{rts},q}$ whose adjustment causes a phase shift corresponding to

$$\frac{\partial \varphi_{\mathrm{A},q}}{\partial \tau_{\mathrm{rts},q}} = 2\pi \left(f_{\mathrm{rts}} + \frac{B}{2} \right) \tag{6.15}$$

For illustrative purposes, Fig. 6.8 shows exemplarily the simulation results of the calibration process plotting the calculated angle error as a function of the

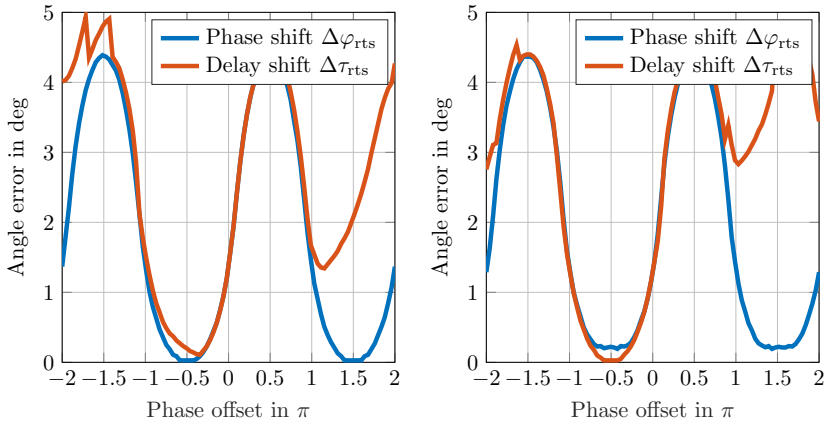

(a) $\Delta R_{\mathrm{c}} = \lambda/8$ (b) $\Delta R_{\mathrm{c}} = (10 + 1/8)\,\lambda$

Figure 6.8: Simulation of the phase calibration with the angle error over the phase offset using phase shifts $\Delta\varphi_{\mathrm{rts}}$ and delay shifts $\Delta\tau_{\mathrm{rts}}$ for two different physical range offsets ΔR_{c}

phase shifts induced by a phase shifter $\Delta\varphi_{\mathrm{rts}} \in [-2\pi, 2\pi]$ and a delay offset $\Delta\tau_{\mathrm{rts}} \in [-1\,\mathrm{ns}, 1\,\mathrm{ns}]$ for two different initial physical distance offsets ΔR_{c}. As can be seen, in both plots the angle error arrives at a minimum for a phase shift of $\Delta\varphi = -\pi/2$, which is in accordance with the previous elaborations since it eliminates the initial phase shift introduced by ΔR_{c}. However, as is noticeable in the comparison of the two graphs, there are differences in the minimum values of the angle error for the respective parameter sweeps. This is due to the difference between the two initial distance offsets of 10λ, as it does not cause any phase shift, but it does cause a deterioration of the amplitude balance which in turn introduces an angle error as mentioned before. The difference of the minimum angle error between the two different phase sweeping methods within one graph can be explained by the range shift caused by the delay shift $\Delta\tau_{\mathrm{rts}}$, which also leads to an amplitude imbalance, but of much smaller magnitude.

It is for this reason, that neither of the two phase calibration methods clearly outperforms the other, given the uncertainty of the exact initial position of the individual target peaks within the range bin, as it is to be expected in a real measurement environment. In order to nevertheless make a selection between the two methods, their implementation complexity in the respective system

topology can be considered. Either method is fairly easy to realize in the digital domain with complex multipliers. On the other hand, the implementation of a variable, frequency-invariant phase shift for an analog signal with a high relative bandwidth is rather difficult when only analog components are available. The analog implementation of a small-step delay shift, while also non-trivial, is more viable [TMH+03, Hol74, ALP+17]. Therefore, the following verification measurement will focus on the true-time-delay sweep calibration method in order to demonstrate not only the practical functionality of the signal superposition approach, but also the feasibility of its implementation.

6.5 Verification Measurement

In order to verify the functioning of the proposed approach, a measurement campaign was conducted and published in [DNPZ22]. For this, the RTS system that is described in chapter 4 was set up in front of a Texas Instruments

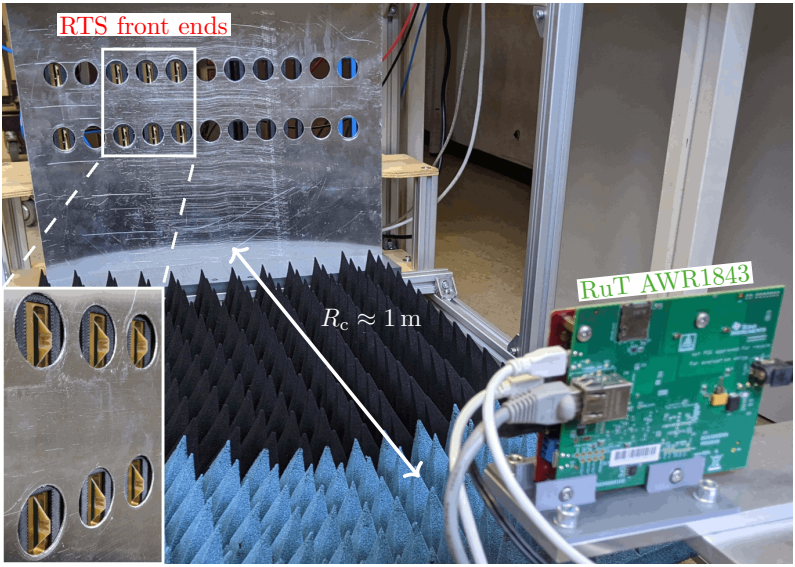

Figure 6.9: Photograph of the arbitrary angle of arrival measurement setup © 2021 IEEE [DNPZ22]

Table 6.1: Radar parameters

Name	Symbol	Value
Carrier frequency	f_{cr}	77 GHz
Bandwidth	B	1 GHz
Chirp repetition period	T_{c}	41.33 µs
Number of chirps	N_{c}	120
Sampling rate	f_{s}	25 MS/s
Number of transmit antennas	N_{tx}	2
Number of receive antennas	N_{rx}	4
Antenna element spacing	d_{A}	$\lambda/2$

AWR1843BOOST radar sensor, that was utilized as the RuT, at a physical distance of $R_{\mathrm{c}} \approx 1$ m. A photograph of the setup of the measurement is shown in Fig. 6.9. The receive and transmit front ends of the RTS were placed in a semi-circle formation, vertically aligned and behind a metal sheet that was used to block off undesired radar reflections of any structures in the background. The carrier frequency of the RTS was set to $f_{\mathrm{rts}} = 500$ MHz and the sampling frequency of the ADCs and DACs to $f_{\mathrm{s,rts}} = 4$ GHz. The radar sensor was configured according to the parameters in Table 6.1.

Calibration Measurement

As a first step, a calibration measurement in accordance with the method described in the previous chapter was conducted. For this purpose, two RTS channels were synchronized in regard of their amplitude and the range-Doppler bin occupied by the virtual radar target that they generate. For this individual measurements were performed with only one channel active at a time. The front ends of the channels were solely distributed in azimuth, with no elevation differences and positioned at the azimuth angles of $\theta_1 = 3.4°$ and $\theta_2 = 12.2°$ from the perspective of the RuT. The phase calibration was performed by monitoring the angle error, which is calculated as the difference between the detected and set-point angle, keeping the delay of the first RTS channel $\tau_{\mathrm{rts},1}$ constant,

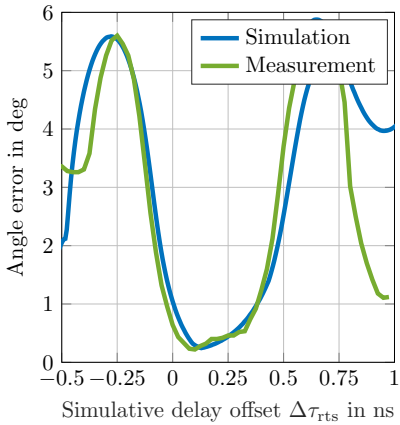

Figure 6.10: Simulation and measurement for the phase calibration with the angle error over the artificial delay offset $\Delta\tau_{\mathrm{rts}}$ © 2021 IEEE [DNPZ22]

while sweeping that of the second channel $\tau_{\mathrm{rts},2} = \tau_{\mathrm{rts},1} + \Delta\tau_{\mathrm{rts}}$ in an interval of $\Delta\tau_{\mathrm{rts}} = [-0.5\,\mathrm{ns}, 1\,\mathrm{ns}]$ with a step size of 25 ps. The smallest delay increment realizable with sampling buffering and the sample frequency used to discretize the signal $\Delta\tau_{\mathrm{rts,buf}} = 1/f_{\mathrm{s,rts}} = 0.25\,\mathrm{ns}$ exceeds the delay step size required for the phase calibration, which is why the fractional delay filter unit that is described in 5.4.3 was used. Fig. 6.10 shows the measurement of the calculated angle error as a function of the artificial delay offset $\Delta\tau_{\mathrm{rts}}$. As can be observed, the angle error arrives at a minimum for $\Delta\tau_{\mathrm{rts}} = 0.1$ ns, which is used to calibrate the RTS channels for the subsequent measurements. In addition, the simulation of the angle error is plotted in order to verify the analytical derivations of the extended signal model in section 6.2. Measurement and simulation show good agreement, as only small deviations occur that can be traced back to differences between the simulated and the actual physical positions of the front ends in regards of range and angle. For the simulation, the positions were determined by a separate measurement, whose inaccuracies lead to the mentioned differences in simulated and actual FE positions.

Linearity Measurement

Next, the achievable linearity and its corresponding error of the AoA of the superimposed virtual radar target were measured. For this purpose, the RTS channels were synchronized in regard of amplitude, delay and phase according to the previously performed calibration measurement. For the linearity measurement itself, the set-point angle was increased in 100 steps in the interval of $\alpha_{\text{tgt}} \in [\theta_1, \theta_2] = [3.4°, 12.2°]$ and the required channel attenuations were calculated according to (6.10) and (6.11). In Fig. 6.11, the detected AoA over the set-point angle α_{tgt} is depicted. Additionally, the results of a simulation of the detected angle according to the signal model in section 6.2 are plotted which show good agreement with the measurement results. In Fig. 6.12, the calculated angle error of the measurement and the simulation can be seen. Although the angle error of the measurement exceeds that of the simulation, the maximum measured error of less than 0.18° correlates to only 2.1 % of the

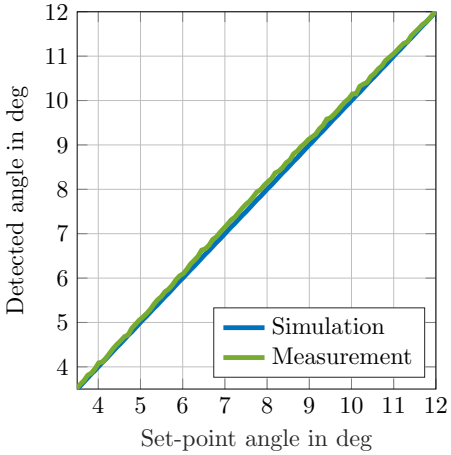

Figure 6.11: Simulation and measurement of the detected angle over the set-point angle © 2021 IEEE [DNPZ22]

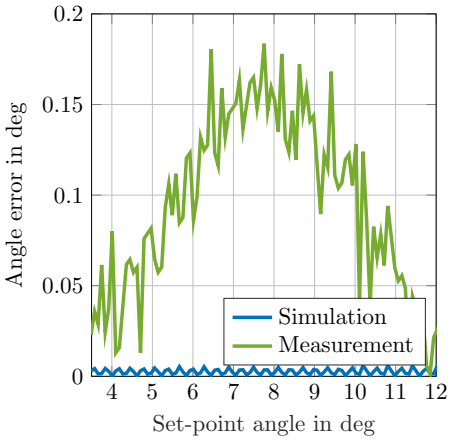

Figure 6.12: Simulation and measurement of the angle error over the set-point angle © 2021 IEEE [DNPZ22]

angular separation of the RTS FEs ($\Delta\theta = 8.8°$). This represents a reduction of the angle error by

$$1 - \frac{0.18°}{50\,\% \cdot \Delta\theta} \mathrel{\hat{=}} 95.9\,\% \tag{6.16}$$

when compared to the conventional approach, in which no signal superposition is performed and virtual targets are only simulated by a single RTS channel each. Furthermore, it can be assumed that the angle error occurs due to a remaining amplitude and phase offset between the utilized RTS channels due to a non-ideal calibration. The latter could be further reduced by an iterative calibration with decreasing step sizes for $\Delta\tau_{\mathrm{rts}}$, but can not be eliminated completely as the aforementioned restrictions still apply. The simulation again serves as a reference for the underlying theory developed in the previous chapters.

Dynamic Multi-Target Measurement

For the final verification measurement, a scenario with four dynamic virtual targets was generated by the RTS. All targets were created by the same two RTS

Table 6.2: Virtual Target Properties

Target	Range	Velocity	Angle
1	33.5 m	0 m/s	7°
2	37 m	4 m/s	4°
3	45 m	−2 m/s	10°
4	52 m	−5 m/s	11°

channels simultaneously, but with different range, radial velocity and angle of arrival characteristics which are stated in Table 6.2. For this, the channels were calibrated in the same manner as before and also the Doppler shift components in the target generation unit were synchronized in regard of their phases. Fig. 6.13 illustrates the range-Doppler and range-angle plot with red crosses indicating the detected targets of the measurement. It can be observed, that the targets are generated with the correct range, velocity and angle of arrival features. This proves the functionality of the approach to generate dynamic, multi-target scenarios, which are required for the validation testing of ADAS functions and the radar sensors involved. The spurious peaks that occur in both plots with

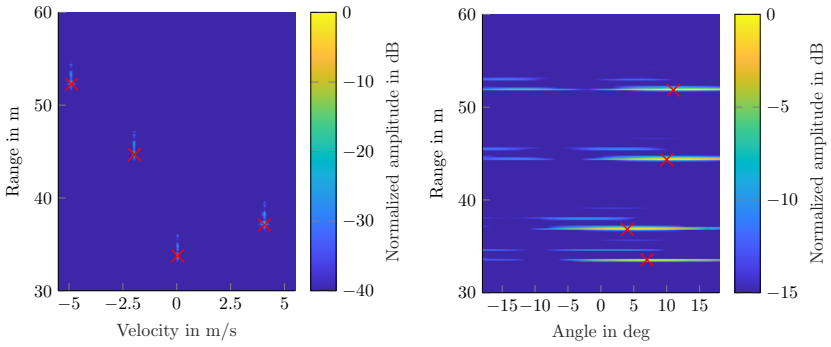

(a) Range-Doppler plot

(b) Range-angle plot

Figure 6.13: Measurement of a dynamic multi-target scenario with red crosses indicating the detected targets © 2021 IEEE [DNPZ22]

an additional range offset to the intended targets are caused by the mismatch of the characteristic impedance between the front ends and the coaxial cables connected to them. The radar signal travels back and forth between the back and front end of the RTS, creating ghost targets with range offsets of multiples of the cable length. The static reflection in close vicinity to the radar can be assigned to the mechanical structure setup of the RTS.

6.6 Achievable Angle Accuracy

In the previous chapter, the practical functionality of the presented approach for generating superimposed virtual radar targets at an arbitrary angle of arrival and thus its capability to increase the angular accuracy of an RTS system was demonstrated. However, the verification measurement was conducted for only one specific front end separation value. In order to further investigate the ability and limitations of the approach to reduce the angular error of a simulated target and thereby to estimate the number of RTS channels required, this section examines the achievable angle accuracy as a function of the front end separation $\Delta\theta$ and the respective channel imbalances. In this context, angle accuracy can be equated with the angle error with which the virtual targets are generated by the RTS. This allows an in-depth analysis of the aforementioned constraint that the front end spacing must not exceed a certain threshold in order for the RTS channels to form a common virtual radar target. The elaborated findings provide a basis for the systematic decision making regarding the total number and placement of the RTS FEs.

For this purpose, another series of measurements was performed using the same RuT and RTS system with the same configurations as in the verification measurement. Two front end receive-transmit pairs were positioned at a distance of $R_\mathrm{c} \approx 1$ m to the RuT. The first pair was mounted statically on a tripod, while the second one was installed on the end of a wooden beam that was attached to a rotation motor that resided below the RuT. This setup allowed to change the angular position of the second FE and thus to adjust the FE separation angle $\Delta\theta$ at will. A photograph of the assembly is shown in Fig. 6.14.

For the actual measurement process, the FE separation angle $\Delta\theta$ was increased stepwise. In each step, the RTS channels were calibrated with regard to range, amplitude and phase, and subsequently a superimposed virtual radar target

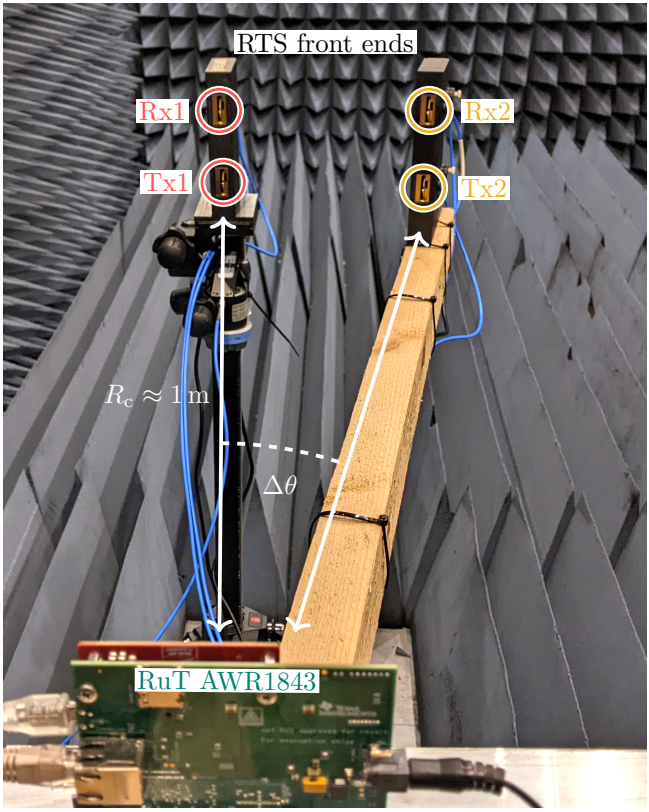

Figure 6.14: Photograph of the achievable angle accuracy measurement setup

was created whose intended AoA α_{tgt} was swept from the position of the first FE to that of the other in $N_{\mathrm{step}} = 100$ steps, in the same way as in the linear measurement procedure. For each step the relative angle error was computed as the absolute value of the difference between the respective set-point $\alpha_{\mathrm{tgt}}(n_{\mathrm{step}})$ and detected angle $\alpha_{\mathrm{det}}(n_{\mathrm{step}})$ over the front end separation angle $\Delta\theta$

$$\alpha_{\epsilon,\mathrm{rel}}(n_{\mathrm{step}}) = \left| \frac{\alpha_{\mathrm{tgt}}(n_{\mathrm{step}}) - \alpha_{\mathrm{det}}(n_{\mathrm{step}})}{\Delta\theta} \right| \tag{6.17}$$

where $n_{\text{step}} \in [1, N_{\text{step}}]$ describes the step index. Then, for each FE separation step the maximum relative angle error was calculated among all simulated angle steps

$$\alpha_{\epsilon,\text{rel,max}}(\Delta\theta) = \max_{n_{\text{step}}} \alpha_{\epsilon,\text{rel}}(n_{\text{step}}) \tag{6.18}$$

Next, the front end separation $\Delta\theta$ was increased and the procedure was repeated.

The results of the measurement together with those of a simulation that is based on the extended signal model developed in section 6.2 are shown in Fig. 6.15, where the maximum relative angle error is drawn as a function of the FE separation $\Delta\theta$. This form of presentation was chosen to liberate the results from the parametric configuration of the RuT (angle resolution) and to provide a generic representation of the capability of the approach. The simulation takes into account the occurrence of amplitude (ΔA) and phase mismatches ($\Delta\varphi$) between the RTS channels, which can be caused by an imperfect calibration or potential hardware influences. These mismatches are potentially also present in the measurement results, but to an unknown extent for which the simulation serves as a reference. Due to the geometrical dimensions of the FEs the minimum FE separation realizable for the measurement was 4°. A horizontal dashed line indicates the maximum relative angle error of the conventional angle simulating approach for RTS systems with lateral distributed FEs (50 %) as a reference.

The results show that the angular error of the system becomes more sensitive to amplitude and phase imbalances between the RTS channels for larger FE separations. In particular, the simulated phase deviation of $\Delta\varphi = \pi/2$ causes a partially destructive interference of the superimposed target and the occurence of an unintended second target, thus a rather strong distortion of the detected angle. This also complies with the previous simulation results shown in Fig. 6.5a. The results underline the importance of the preceding calibration and demonstrate the dependency of the angular accuracy thereon. In general, measurement and simulation are in good agreement, which verifies the signal model and its ability to estimate the angle error to be expected given the separation of the FEs and the imbalances of the RTS channels. Conversely, the model can also be used to determine the number of FEs needed when the field of view (FoV) of the RuT, the RTS channel imbalances and the angle error tolerable are given.

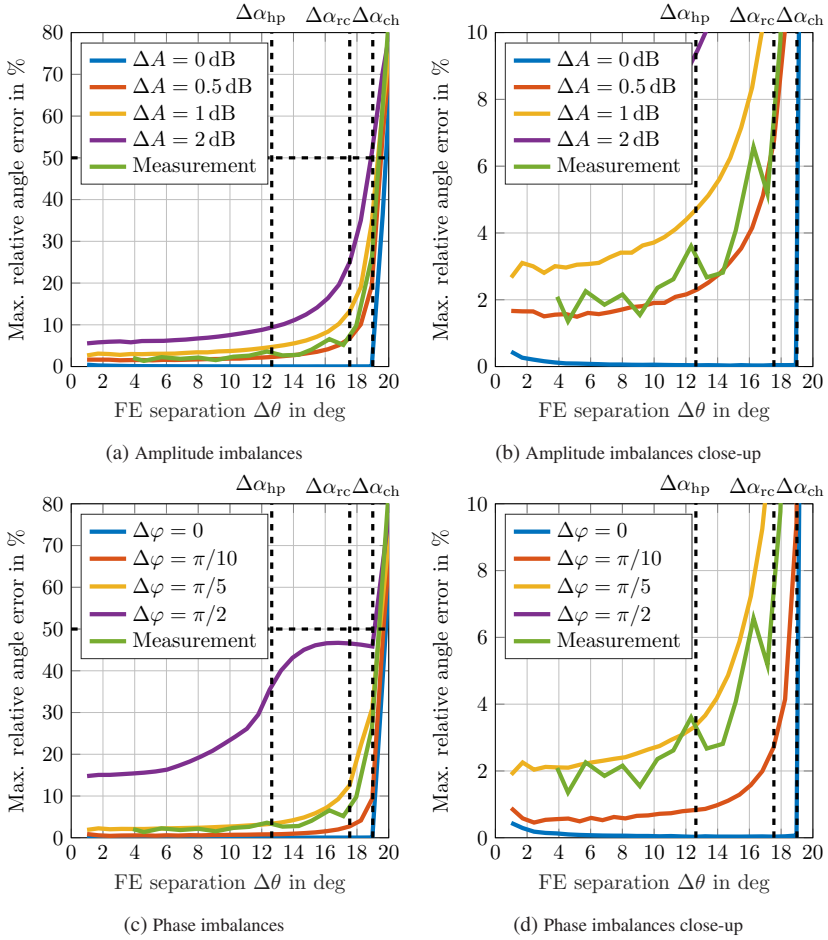

(a) Amplitude imbalances

(b) Amplitude imbalances close-up

(c) Phase imbalances

(d) Phase imbalances close-up

Figure 6.15: Measurement and simulation of the achievable angle accuracy as a function of the front end separation $\Delta\theta$ in the presence of (a, b) amplitude and (c, d) phase imbalances

Both estimations can support the design and layout process of high-precision, angle simulating RTS systems.

Angular Boundary Condition for Superposition of Echo Signals

The maximum relative angle error rises sharply for a FE separation that is too large for the superimposed signal to form a single, common peak. For this FE spacing and onward, two distinct peaks are formed in the angular profile and the AoA estimated by the radar deviates significantly from its set-point. Counterintuitively, this turning point does not coincide with the definitions of the angular resolution (half-power beamwidth $\Delta\alpha_{\mathrm{hp}}$ and Rayleigh criterion $\Delta\alpha_{\mathrm{rc}}$) of the utilized radar sensor given in section 2.5.1 and marked with dashed, vertical lines in Fig. 6.15. It lies beyond either of them, as can best be witnessed in the case of the ideal simulation ($\Delta A = 0$ and $\Delta\varphi = 0$), where the maximum relative angle error increases sharply only for a FE separation not negligibly larger than the two. This discrepancy is a result of the different coherence assumptions between the superposition of radar echoes with the intent of composing a virtual radar target at a controllable AoA and the ability of a radar to discriminate two independent targets in the angular domain, that is, the angular resolution.

Both definitions of the angular resolution presume two spatially separated targets of equal range, radial velocity and electromagnetic size whose reflected radar signals are incoherent in regard of their phases. Due to RCS fluctuations, the individual echo signals exhibit a random phase relation, which can lead to constructive or destructive inference of the individual targets within a single measurement. Throughout the course of multiple measurement cycles, the relative phase of the individual signal is uniformly distributed, hence the superposition of the individual target signals according to the angular resolution is considered as an incoherent summation only in terms of the signal power, that is, the absolute value of the amplitudes and neglecting any phase information. Therefore, the angular resolution can be thought of as a statistical expression for the separability of two targets in angular domain, that is not applicable to the superposition of two phase-coherent echoes as encountered in this work.

In contrast, the concept of superimposing the returning signals from two adjacent RTS FEs for the purpose of generating a virtual radar target with an arbitrarily controllable AoA as presented here requires not only phase co-

herency, i.e., a constant phase relation of the RTS channels involved, but also a phase offset of multiples of 2π ($\Delta\varphi = \varphi_1 - \varphi_2 = 2n\pi\ , n \in \mathbb{N}$). This constraint is explained in more detail in section 6.3 and the calibration process discussed in section 6.4 is employed to satisfy it. The result is a phase coherent, complex-valued superposition of the individual radar echoes with respect to the individual signal amplitudes and phases.

The applicable boundary condition for the coherent superposition of two radar targets to form a common peak, i.e., the coherent angular resolution, is given by the first inflection point of the angle profile of an individual target echo. It can be found by setting the second derivative of the signal function from (6.3) equal to zero

$$\frac{\partial^2 s_{\mathrm{A},q}(\alpha)}{\partial \alpha^2} = 0 \tag{6.19}$$

and solving numerically for α, resulting in a coherent angular resolution of

$$\Delta\alpha_{\mathrm{ch}} = 1.32 \frac{\lambda}{N_{\mathrm{A}} d_{\mathrm{A}}} \,\mathrm{rad} \tag{6.20}$$

If the two individual target functions are superimposed at their first inflection points, they form a plateau between them, since the function value of the first signal decreases from this point onward as quickly as that of the second function increases. For a larger separation, two distinct peaks are formed. The boundary condition of the coherent superposition is also indicated in Fig. 6.15 and coincides with the turning point of the maximum relative angle error in the case of the ideal simulation.

The distinction between the coherent and incoherent superposition of two radar echoes is illustrated exemplarily in Fig. 6.16 for the borderline case of a angular separation of $\Delta\alpha_{\mathrm{rc}} < \Delta\theta = 18° < \Delta\alpha_{\mathrm{ch}}$. As can be seen, for this particular separation angle the incoherently superimposed signal already features two distinct peaks, whereas the coherent superposition still forms a single common one. The first inflection points of the individual signals are marked by dots.

Therefore, it can be concluded that it is necessary to take into account the phases of the RTS channels whether the here presented concept to superimpose virtual targets or the conventional AoA simulation approach is used, since unfortunate phase relations among neighboring channels can lead to destructive interference

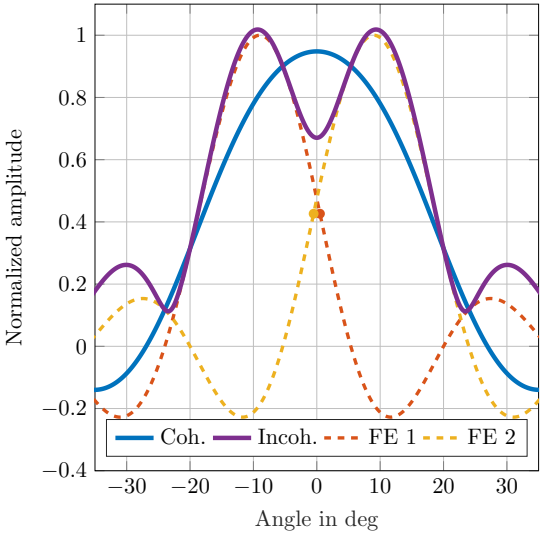

Figure 6.16: Simulated angle profile for coherent and incoherent signal superposition of two radar targets after beamforming for a separation angle of $\Delta\theta = 18°$

canceling out the intended targets. This means that even if the presented approach is omitted, a phase calibration or alternatively an RCS fluctuation simulation model is required. However, as has been shown, the presented concept enables to greatly reduce the number of FEs needed and therefore cuts the corresponding hardware costs substantially.

6.7 Quasi-Monostatic Antenna Displacement

Another source of angular error in radar target simulation, in addition to the previously mentioned FE separation and amplitude and phase imbalances, is the quasi-monostatic characteristic of the RTS FEs. The antennas of the RTS for reception and re-transmission of the radar signal are placed closely together, but still are spatially separated, thus the system can be considered quasi-monostatic. Since the simulated AoA of a virtual radar target is, among others, defined by the physical position of the respective RTS FEs, this characteristic induces an

uncertainty between intended and actual target angle. The radar signal emitted by the RuT is received and re-transmitted at slightly different angular positions which causes the detected AoA to deviate from the physical position of the receiver and transmitter. Fig. 6.17 visualizes the individual signal paths for the receive and transmit signal. In radar validation setups where only a single angular domain is of interest, this issue can be circumvented by aligning the receive and transmit antenna of an FE pair perpendicular to the resolvable

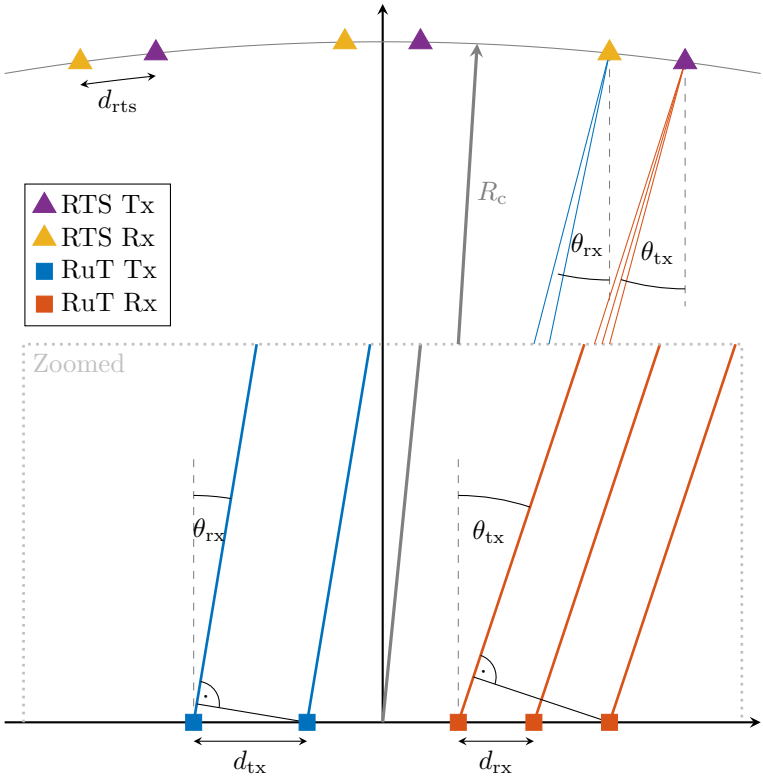

Figure 6.17: Conceptual representation of the quasi-monostatic characteristic of radar target simulation that leads to differences in signal path lengths and propagation delays. The scaling and spacing of the figure were chosen for illustrative purposes and are not representative. © 2022 IEEE [DNZ22]

angular domain. However, since current and future radar sensors are capable of two-dimensional angle of arrival estimation [Con21, Rob21], this technique does no longer present a workaround and the uncertainty in the angle simulation should be investigated.

Extended Signal Model

For this purpose, the RTS signal model presented in 4.6 is adapted and the simplifications of equating the angular positions of the receive and transmit antenna of the RTS FE are removed. The physical position of the FE is split up into a receive angle θ_{rx} and a transmit angle θ_{tx}. Furthermore, the unification of the transmit and receive antenna elements of the RuT to form a virtual antenna array is lifted, in order to break down the effects of delay differences in the outward and return propagation of the radar signal. For a better illustration, the following adapted signal model only considers the spatial separation of the receive and transmit antennas in the azimuth domain, as this allows for a simplified representation of the model, but still enables the investigation of the quasi-monostatic characteristics. With these considerations, the delay of the signal due to its propagation through free space to and from the RTS can be described as

$$\tau_{\mathrm{tx}} = \frac{R_{\mathrm{c}} + d_{\mathrm{tx}} \sin(\theta_{\mathrm{rx}})}{c_0} \cdot n_{\mathrm{tx}} \tag{6.21}$$

$$\tau_{\mathrm{rx}} = \frac{R_{\mathrm{c}} + d_{\mathrm{rx}} \sin(\theta_{\mathrm{tx}})}{c_0} \cdot n_{\mathrm{rx}} \tag{6.22}$$

where $d_{\mathrm{tx/rx}}$ specifies the element spacing of the transmit and receive antennas of the RuT, respectively, and $n_{\mathrm{tx/rx}} \in [0, N_{\mathrm{tx/rx}} - 1]$ indexes the individual antenna elements. The round-trip signal delay can be expressed as

$$\tau_{\mathrm{c}} = \tau_{\mathrm{tx}} + \tau_{\mathrm{rx}} = \tau_0 + \frac{d_{\mathrm{tx}} \sin(\theta_{\mathrm{rx}}) \cdot n_{\mathrm{tx}} + d_{\mathrm{rx}} \sin(\theta_{\mathrm{tx}}) \cdot n_{\mathrm{rx}}}{c_0} \tag{6.23}$$

with the antenna element independent delay $\tau_0 = 2R_c/c_0$. With this, the phase of the radar signal after range-Doppler processing and detection by the RuT in accordance with (4.45) can be formulated as

$$\varphi_D(n_{tx}, n_{rx}) = 2\pi \left[\left(f_c + \frac{B}{2} \right) \tau_0 + \left(f_{rts} + \frac{B}{2} \right) \tau_{rts} + \frac{d_{tx} \sin(\theta_{rx}) \cdot n_{tx} + d_{rx} \sin(\theta_{tx}) \cdot n_{rx}}{\lambda} \right] \tag{6.24}$$

For the subsequent beamforming, the beamsteering vector must be adapted for the non-unified antenna array

$$b_{1D}(n_{tx}, n_{rx}, \alpha) = \exp\left\{ -j2\pi \frac{\sin(\alpha)}{\lambda} \left(d_{tx} \cdot n_{tx} + d_{rx} \cdot n_{rx} \right) \right\} \tag{6.25}$$

The spatial spectrum is generated by Fourier beamforming, for which the adapted steering vector is applied to the radar signal and the sum is formed over all transmit and receive antenna elements and for all angles α to be considered

$$s_A(\alpha) = \sum_{n_{tx}=-\frac{N_{tx}-1}{2}}^{\frac{N_{tx}-1}{2}} \sum_{n_{rx}=-\frac{N_{rx}-1}{2}}^{\frac{N_{rx}-1}{2}} s_D(n_{tx}, n_{rx}) \cdot b_{1D}(n_{tx}, n_{rx}, \alpha) \tag{6.26}$$

which can be reformulated to

$$\begin{aligned} s_A(\alpha) = N_c N_s \cdot \exp\left\{ j2\pi \left[\left(f_c + \frac{B}{2} \right) \cdot \frac{2R_c}{c_0} + \left(f_{rts} + \frac{B}{2} \right) \cdot \tau_{rts} \right.\right. \\ \left.\left. + \left(d_{tx} \left(N_{tx} - 1 \right) + d_{rx} \left(N_{rx} - 1 \right) \right) \frac{\sin(\alpha)}{2\lambda} \right] \right\} \\ \cdot \sum_{n_{tx}=0}^{N_{tx}-1} \exp\left\{ j2\pi \frac{d_{tx}}{\lambda} \left(\sin(\theta_{rx}) - \sin(\alpha) \right) \cdot n_{tx} \right\} \\ \cdot \sum_{n_{rx}=0}^{N_{rx}-1} \exp\left\{ j2\pi \frac{d_{rx}}{\lambda} \left(\sin(\theta_{tx}) - \sin(\alpha) \right) \cdot n_{rx} \right\} \end{aligned} \tag{6.27}$$

As before, the partial sum of a geometric series allows to simplify this expression to

$$s_{\mathrm{A}}(\alpha) = N_{\mathrm{c}} N_{\mathrm{s}} \cdot \exp\left\{ \mathrm{j}2\pi \left[\left(f_{\mathrm{c}} + \frac{B}{2} \right) \cdot \frac{2R_{\mathrm{c}}}{c_0} + \left(f_{\mathrm{rts}} + \frac{B}{2} \right) \cdot \tau_{\mathrm{rts}} + \frac{d_{\mathrm{tx}}(N_{\mathrm{tx}} - 1)\sin(\theta_{\mathrm{rx}}) + d_{\mathrm{rx}}(N_{\mathrm{rx}} - 1)\sin(\theta_{\mathrm{tx}})}{2\lambda} \right] \right\} \cdot N_{\mathrm{tx}} \cdot \mathrm{sinc}\left(\frac{d_{\mathrm{tx}}}{\lambda} \left(\sin(\theta_{\mathrm{rx}}) - \sin(\alpha) \right) N_{\mathrm{tx}} \right) \cdot N_{\mathrm{rx}} \cdot \mathrm{sinc}\left(\frac{d_{\mathrm{rx}}}{\lambda} \left(\sin(\theta_{\mathrm{tx}}) - \sin(\alpha) \right) N_{\mathrm{rx}} \right) \tag{6.28}$$

This reveals a function that is composed of two sinc-functions, much like that in the extended signal model for the superposition of adjacent echo signals in chapter 6.2, only this time not as their sum, but as their product. Additionally, the widths of the sinc-functions differ from one another and are determined by the geometrical dimensions of the receive ($d_{\mathrm{rx}} N_{\mathrm{rx}}$) and transmit antenna array ($d_{\mathrm{tx}} N_{\mathrm{tx}}$) of the RuT. This allows to conclude that the position of the maximum of the composite function $s_{\mathrm{A}}(\alpha)$ and thus the detected AoA will be located between the angular position of the RTS receiver θ_{rx} and transmitter θ_{tx} and, moreover, depends on the antenna array configuration of the particular RuT that is employed. Due to the nesting of α within the two separate sinc-functions, the actual value of the detected AoA can not be derived analytically and must be found numerically.

Measurement

In order to verify the adapted signal model, a verification measurement was conducted using the same RuT and RTS system with the same configurations as in the measurements in chapter 6.5 and 6.6. The RuT was positioned at a distance of $R_{\mathrm{c}} \approx 1\,\mathrm{m}$ in front of an RTS receiver and transmitter. A diagram showing the concept of the measurement setup can be seen in Fig. 6.18. Multiple measurements were performed in between which the spatial separation of the RTS antennas was incrementally increased. For this purpose, a linear motor moved the RTS transmitter laterally to the RuT while the position of the receiver was fixed. An additional rotation motor, that was mounted on the linear motor,

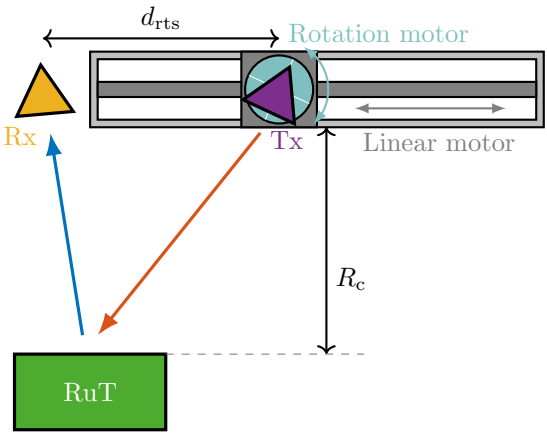

Figure 6.18: Concept of the quasi-monostatic antenna displacement measurement setup © 2022 IEEE [DNZ22]

compensated for the change in the relative angle of the RTS transmitter as seen by the RuT. This was done in order to neutralize any effect that the directional antenna pattern of the RTS transmitter might have on the outcome of the signal processing chain. The resulting additional range offset was accounted for in the simulation, but remained smaller than the range resolution of the radar. In Fig. 6.19 a photograph of the measurement setup can be seen.

The radar signal received by the RuT was processed to estimate the range and angle of arrival of the virtual target. For this, a discrete Fourier transform followed by a range detection was applied to the signal. Subsequently, the AoA was estimated by applying beamforming to the resulting radar signal. The results are shown in Fig. 6.20, where the deviation of the estimated AoA from the angular position of the RTS receiver is depicted as a function of the lateral distance d_{rts} between the RTS receiver and transmitter. The results of the same measurement series were processed with different antenna selections of the RuT (2x4, 2x2, 1x4) and plotted in differently colored, thick lines to demonstrate the influence of the antenna geometry. The fluctuations in the measurement curves are due to multi-path reflections caused by the mechanical structure of the setup, as they occurred identically in successive measurements and could be reduced by placing absorbers. The output of the simulation is drawn in black and shows

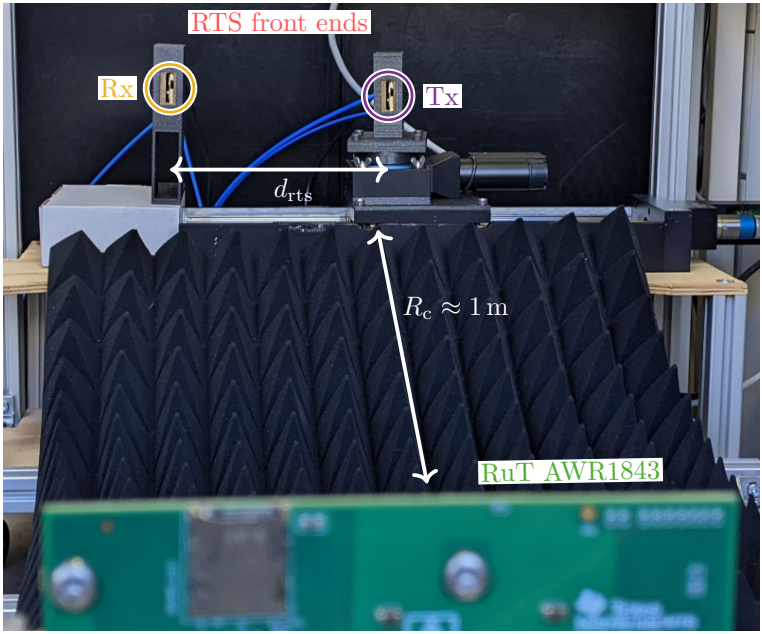

Figure 6.19: Photograph of the quasi-monostatic antenna displacement measurement setup © 2022 IEEE [DNZ22]

good agreement with the measurement, which verifies the adapted signal model and its capability to predict the detected AoA taking into account the quasi-monostatic characteristic of an RTS system. Depending on the selected antenna configuration of the RuT (N_{tx} x N_{rx}), the signal path differences evaluated to determine the AoA of the target are more affected by the number of outward (N_{tx}) or return paths (N_{rx}) of the signal to or from the RTS and are thus more dependent on the position of the RTS receiver or transmitter.

The developed signal model is intended to support the setup and antenna arrangement process of high-precision angle simulating RTS systems. As has been shown, the antenna geometry of the RuT has an impact on the estimated angle of arrival, and thus the antenna aperture and orientation of the RuT must be known a priori. Usually, they can either be concluded given the parameters of the field of view (FoV) and the angular resolution of the RuT, or measured

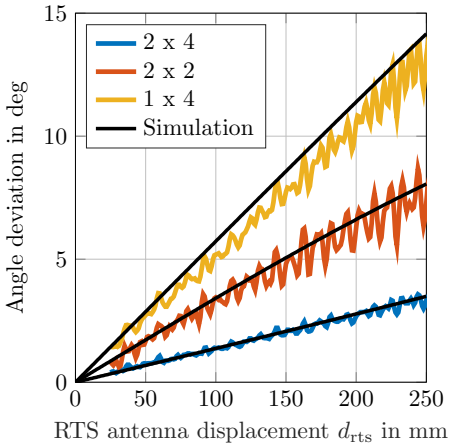

Figure 6.20: Simulation and measurement of the detected angle over the set-point angle © 2022 IEEE [DNZ22]

when removing the packaging of the sensor. With this knowledge and the signal model presented here, the angle deviation that arises from the quasi-monostatic characteristic of the RTS system can be compensated by a minor adjustment of the respective FE positions.

6.8 Two-Dimensional Angle Simulation

Modern 4D imaging radars are capable to detect targets concurrently in both angular domains, azimuth and elevation. Therefore, RTS systems that are employed to validate these sensors must be capable to generate virtual radar targets at freely controllable lateral positions. To achieve this, the previously elaborated approach to superimpose adjacent RTS echoes to form a common target at an arbitrary azimuthal position is extended to also cover the elevation domain. Through the superposition of the return signal of four neighboring RTS channels that are arranged in a vertical square formation, this enhancement enables virtual targets to be created at any two-dimensional angular position. The arrangement concept of the respective RTS FEs and their superimposing radar echoes are shown in Fig. 6.21.

In the following, the RTS signal model developed in 4.6 is again extended, this time to account for the two-dimensional distribution of both the RuT antennas and the RTS FEs. This allows to derive the channel attenuations required to control the simulated AoA of the created virtual target in the azimuth and elevation domain simultaneously. Subsequently, a measurement campaign that verifies the functionality of extension is presented for which, first, the calibration process explained in 6.4 is executed for all RTS channels involved, before the actual measurement series is performed. Virtual targets at various lateral positions distributed in both angular domains are simulated and the detected AoAs are compared to their set-points.

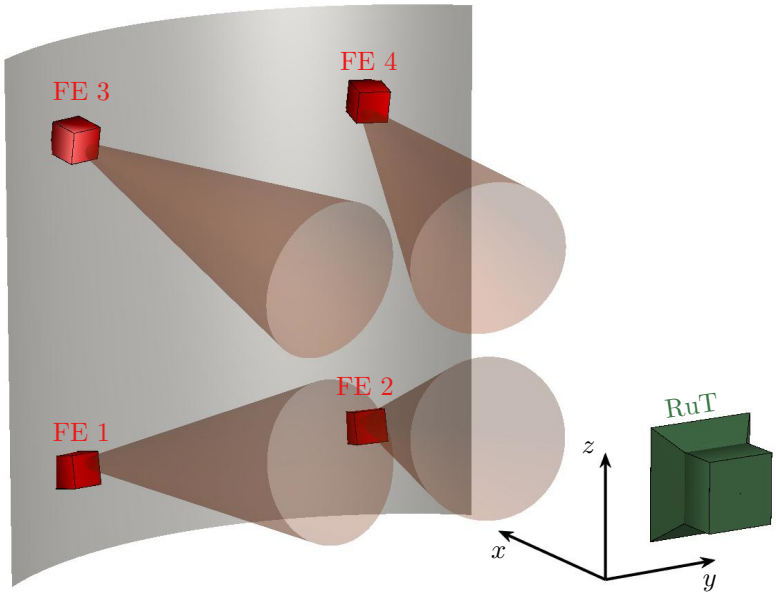

Figure 6.21: Concept of the two-dimensional arbitrary angle of arrival © 2022 IEEE [DNGZ22]

Extended Signal Model

For the extended signal, it is assumed that the transmit and receive antennas of the RuT are distributed in only one angular domain respectively, as is typically the case in current radar sensors. The N_{tx} transmit antennas are allocated only along the vertical axis with an element spacing of d_{tx}. The same applies to the N_{rx} receive antennas in the horizontal domain with a spacing of d_{rx}. Thus, the free space signal propagation delays from the RuT to the RTS FE and back can be expressed as

$$\tau_{\mathrm{tx},q} = \frac{R_{\mathrm{c},q} + d_{\mathrm{tx}} \sin(\psi_q) \cdot n_{\mathrm{tx}}}{c_0} \tag{6.29}$$

$$\tau_{\mathrm{rx},q} = \frac{R_{\mathrm{c},q} + d_{\mathrm{rx}} \sin(\theta_q) \cos(\psi_q) \cdot n_{\mathrm{rx}}}{c_0} \tag{6.30}$$

where $\psi_q, \theta_q \in [-90°, 90°]$ denote the elevation and azimuth angle at which the RTS FE is located as seen by the RuT.

With this, the signal phase after the range-Doppler processing by the RuT follows as

$$\varphi_{\mathrm{D},q}(n_{\mathrm{tx}}, n_{\mathrm{rx}}) = 2\pi \left[\left(f_{\mathrm{c}} + \frac{B}{2} \right) \tau_0 + \left(f_{\mathrm{rts}} + \frac{B}{2} \right) \tau_{\mathrm{rts}} + \frac{d_{\mathrm{rx}} \sin(\theta_q) \cos(\psi_q) \cdot n_{\mathrm{rx}} + d_{\mathrm{tx}} \sin\left(\psi_q\right) \cdot n_{\mathrm{tx}}}{\lambda} \right] \tag{6.31}$$

The two-dimensional steering vector

$$b_{\mathrm{2D}}(n_{\mathrm{tx}}, n_{\mathrm{rx}}, \alpha, \beta) = \exp\left\{ -\mathrm{j} \frac{2\pi}{\lambda} \left[d_{\mathrm{rx}} \sin(\alpha) \cos(\beta) \cdot n_{\mathrm{rx}} + d_{\mathrm{tx}} \sin(\beta) \cdot n_{\mathrm{tx}} \right] \right\} \tag{6.32}$$

has been derived before in chapter 2.4.2 and is stated again here for the sake of clarity. Then the steering vector is applied and the sum is formed over all transmit respectively receive antenna elements. Simplifying in the same manner

as before using the partial sum of a geometric series, as well as $\sin(x) \approx x$ and $\cos(x) \approx 1$ for $|x| \ll 1$ leads to

$$\begin{aligned} s_{\mathrm{A},q}(\alpha,\beta) &= \sum_{n_{\mathrm{tx}}=-\frac{N_{\mathrm{tx}}-1}{2}}^{\frac{N_{\mathrm{tx}}-1}{2}} \sum_{n_{\mathrm{rx}}=-\frac{N_{\mathrm{rx}}-1}{2}}^{\frac{N_{\mathrm{rx}}-1}{2}} s_{\mathrm{D},q}(n_{\mathrm{tx}},n_{\mathrm{rx}}) \cdot b_{\mathrm{2D}}(n_{\mathrm{tx}},n_{\mathrm{rx}},\alpha,\beta) \\ &= A_q N_{\mathrm{c}} N_{\mathrm{s}} \cdot \exp\left\{\mathrm{j}\varphi_{\mathrm{A},q}\right\} \\ &\quad \cdot N_{\mathrm{tx}} \cdot \operatorname{sinc}\left(\frac{d_{\mathrm{tx}}}{\lambda}\left[\sin(\psi_q)-\sin(\beta)\right]N_{\mathrm{tx}}\right) \\ &\quad \cdot N_{\mathrm{rx}} \cdot \operatorname{sinc}\left(\frac{d_{\mathrm{rx}}}{\lambda}\left[\sin(\theta_q)-\sin(\alpha)\right]N_{\mathrm{rx}}\right) \end{aligned} \tag{6.33}$$

with a signal phase of

$$\begin{aligned} \varphi_{\mathrm{A},q} = 2\pi\Bigg[&\left(f_{\mathrm{c}}+\frac{B}{2}\right)\tau_0 + \left(f_{\mathrm{rts}}+\frac{B}{2}\right)\tau_{\mathrm{rts}} \\ &+ \frac{d_{\mathrm{rx}}\,(N_{\mathrm{rx}}-1)\sin(\theta_q) + d_{\mathrm{tx}}\,(N_{\mathrm{rx}}-1)\sin(\psi_q)}{2\lambda}\Bigg] \end{aligned} \tag{6.34}$$

This time, the sinc-function stretches along both spatial axis and has its main maximum at $\sin(\alpha) = \sin(\theta_q)$ and $\sin(\beta) = \sin(\psi_q)$. Through the superposition of $Q = 4$ artificial radar echoes and controlling the attenuation of the corresponding RTS channels, a common virtual radar target is created whose AoA can be steered in the azimuth and elevation domain. The superimposed signal after the two-dimensional beamforming can be expressed as

$$\begin{aligned} \widehat{s}_{\mathrm{A}}(\alpha,\beta) &= \sum_{q=1}^{Q} s_{\mathrm{A},q}(\alpha,\beta) \\ &= s_{\mathrm{A},1}(\alpha,\beta) + s_{\mathrm{A},2}(\alpha,\beta) + s_{\mathrm{A},3}(\alpha,\beta) + s_{\mathrm{A},4}(\alpha,\beta) \end{aligned} \tag{6.35}$$

In contrast to before, deriving the expression above according to α and β does not allow to determine the required channel attenuations A_q, but results in an underdefined system of equations due to the presence of too many unknown

variables. Therefore, further simplifications are made. First, the phase of each individual signal (6.34) is assumed to be equal

$$\varphi_{\mathrm{A},q} = \varphi_{\mathrm{A}} \qquad \forall \qquad q \in [1, Q] \tag{6.36}$$

which will later be ensured by a calibration prior to the actual measurement. Second, due to the horizontal and vertical alignment of the FEs, the angle variables can be partially equated to form a left, right, bottom and top angular position

$$\theta_{\mathrm{L}} = \theta_1 = \theta_3 \tag{6.37}$$
$$\theta_{\mathrm{R}} = \theta_2 = \theta_4 \tag{6.38}$$
$$\psi_{\mathrm{B}} = \psi_1 = \psi_2 \tag{6.39}$$
$$\psi_{\mathrm{T}} = \psi_3 = \psi_4 \tag{6.40}$$

Subsequently, the individual signal attenuations can be substituted by the product of two fictional attenuations that correspond to their angular positions (left, right, bottom and top)

$$A_1 = A_{\mathrm{B}} \cdot A_{\mathrm{L}} \tag{6.41}$$
$$A_2 = A_{\mathrm{B}} \cdot A_{\mathrm{R}} \tag{6.42}$$
$$A_3 = A_{\mathrm{T}} \cdot A_{\mathrm{L}} \tag{6.43}$$
$$A_4 = A_{\mathrm{T}} \cdot A_{\mathrm{R}} \tag{6.44}$$

Additionally, for the sake of clarity, the following substitutes for the sinc-functions will be employed

$$h_q(\alpha) = \mathrm{sinc}\left(\frac{N_{\mathrm{rx}}}{\lambda}\left(\sin(\theta_q) - \sin(\alpha)\right) \cdot d_{\mathrm{rx}}\right) \tag{6.45}$$
$$h_q(\beta) = \mathrm{sinc}\left(\frac{N_{\mathrm{tx}}}{\lambda}\left(\sin(\psi_q) - \sin(\beta)\right) \cdot d_{\mathrm{tx}}\right) \tag{6.46}$$

By inserting all these substitutes, (6.35) can be simplified to

$$\begin{aligned}\widehat{x}_{\mathrm{A}}(\alpha,\beta) = N_{\mathrm{A}}N_{\mathrm{c}}N_{\mathrm{s}} \cdot \exp\{\mathrm{j}\varphi_{\mathrm{A}}\} \\ \cdot \big[A_{\mathrm{L}}A_{\mathrm{B}} \cdot h_{\mathrm{L}}(\alpha) \cdot h_{\mathrm{B}}(\beta) + A_{\mathrm{R}}A_{\mathrm{B}} \cdot h_{\mathrm{R}}(\alpha) \cdot h_{\mathrm{B}}(\beta) \\ + A_{\mathrm{L}}A_{\mathrm{T}} \cdot h_{\mathrm{L}}(\alpha) \cdot h_{\mathrm{T}}(\beta) + A_{\mathrm{R}}A_{\mathrm{T}} \cdot h_{\mathrm{R}}(\alpha) \cdot h_{\mathrm{T}}(\beta)\big]\end{aligned} \tag{6.47}$$

Factorizing the fictional attenuations and their corresponding sinc-functions allows to reformulate the equation as

$$\begin{aligned}\widehat{x}_{\mathrm{A}}(\alpha,\beta) = N_{\mathrm{A}}N_{\mathrm{c}}N_{\mathrm{s}} \cdot \exp\{\mathrm{j}\varphi_{\mathrm{A}}\} \\ \cdot \big[A_{\mathrm{L}} \cdot h_{\mathrm{L}}(\alpha) + A_{\mathrm{R}} \cdot h_{\mathrm{R}}(\alpha)\big] \cdot \big[A_{\mathrm{B}} \cdot h_{\mathrm{B}}(\beta) + A_{\mathrm{T}} \cdot h_{\mathrm{T}}(\beta)\big]\end{aligned} \tag{6.48}$$

In this form, the amplitude relations for the control of the azimuth and elevation AoA of the composed virtual target can be found individually by setting the partial derivative according to α and β equal to zero respectively

$$\nabla \widehat{x}_{\mathrm{A}}(\alpha,\beta) = 0 \tag{6.49}$$

$$\begin{aligned}\frac{\partial \widehat{x}_{\mathrm{A}}(\alpha,\beta)}{\partial\alpha} = N_{\mathrm{A}}N_{\mathrm{c}}N_{\mathrm{s}} \cdot \exp\{\mathrm{j}\varphi_{\mathrm{A}}\} \\ \cdot \left[A_{\mathrm{L}} \cdot \frac{\partial h_{\mathrm{L}}(\alpha)}{\partial\alpha} + A_{\mathrm{R}} \cdot \frac{\partial h_{\mathrm{R}}(\alpha)}{\partial\alpha}\right] \cdot [A_{\mathrm{B}} \cdot h_{\mathrm{B}}(\beta) + A_{\mathrm{T}} \cdot h_{\mathrm{T}}(\beta)] = 0\end{aligned} \tag{6.50}$$

$$\begin{aligned}\frac{\partial \widehat{x}_{\mathrm{A}}(\alpha,\beta)}{\partial\beta} = N_{\mathrm{A}}N_{\mathrm{c}}N_{\mathrm{s}} \cdot \exp\{\mathrm{j}\varphi_{\mathrm{A}}\} \\ \cdot [A_{\mathrm{L}} \cdot h_{\mathrm{L}}(\alpha) + A_{\mathrm{R}} \cdot h_{\mathrm{R}}(\alpha)] \cdot \left[A_{\mathrm{B}} \cdot \frac{\partial h_{\mathrm{B}}(\beta)}{\partial\beta} + A_{\mathrm{T}} \cdot \frac{\partial h_{\mathrm{T}}(\beta)}{\partial\beta}\right] = 0\end{aligned} \tag{6.51}$$

According to the zero-product property, a product is zero if one of its elements equals zero [DF03], which can be utilized to make the following extractions

$$A_{\mathrm{L}} \cdot \frac{\partial h_{\mathrm{L}}(\alpha)}{\partial\alpha} + A_{\mathrm{R}} \cdot \frac{\partial h_{\mathrm{R}}(\alpha)}{\partial\alpha} = 0 \tag{6.52}$$

$$A_{\mathrm{B}} \cdot \frac{\partial h_{\mathrm{B}}(\beta)}{\partial\beta} + A_{\mathrm{T}} \cdot \frac{\partial h_{\mathrm{T}}(\beta)}{\partial\beta} = 0 \tag{6.53}$$

From this, the amplitude relations to control the horizontal and vertical position of the superimposed virtual target can be derived

$$\frac{A_\mathrm{L}}{A_\mathrm{R}} = -\frac{\frac{\partial h_\mathrm{R}(\alpha)}{\partial \alpha}}{\frac{\partial h_\mathrm{L}(\alpha)}{\partial \alpha}} \tag{6.54}$$

$$\frac{A_\mathrm{B}}{A_\mathrm{T}} = -\frac{\frac{\partial h_\mathrm{T}(\beta)}{\partial \beta}}{\frac{\partial h_\mathrm{B}(\beta)}{\partial \beta}} \tag{6.55}$$

Together with the adjusted amplitude-based superposition of the signals

$$\sigma \sim \widehat{P} = \frac{\left(\sum_{q=1}^{Q} A_q\right)^2}{R_\Omega} = \frac{(A_1 + A_2 + A_3 + A_4)^2}{R_\Omega} \tag{6.56}$$

the required RTS channel attenuations for a given azimuth α_tgt and elevation β_tgt angle can be determined unambiguously.

For reasons of completeness, the derivatives of the sinc-function substitutes are given as

$$\begin{aligned}\frac{\partial h_q(\alpha)}{\partial \alpha} =& \frac{\cos(\alpha)\sin\left(\pi \frac{N_\mathrm{rx}}{\lambda}\left(\sin(\theta_q) - \sin(\alpha)\right)\cdot d_\mathrm{rx}\right)}{\pi \frac{N_\mathrm{rx}}{\lambda}\cdot d_\mathrm{rx}\cdot(\sin(\theta_q) - \sin(\alpha))^2} \\ &- \frac{\cos(\alpha)\cos\left(\pi \frac{N_\mathrm{rx}}{\lambda}\cdot(\sin(\theta_q) - \sin(\alpha))\cdot d_\mathrm{rx}\right)}{\sin(\theta_q) - \sin(\alpha)}\end{aligned} \tag{6.57}$$

$$\begin{aligned}\frac{\partial h_q(\beta)}{\partial \beta} =& \frac{\cos(\beta)\sin\left(\pi \frac{N_\mathrm{tx}}{\lambda}\left(\sin(\psi_q) - \sin(\beta)\right)\cdot d_\mathrm{tx}\right)}{\pi \frac{N_\mathrm{tx}}{\lambda}\cdot d_\mathrm{tx}\cdot(\sin(\psi_q) - \sin(\beta))^2} \\ &- \frac{\cos(\beta)\cos\left(\pi \frac{N_\mathrm{tx}}{\lambda}\cdot(\sin(\psi_q) - \sin(\beta))\cdot d_\mathrm{tx}\right)}{\sin(\psi_q) - \sin(\beta)}\end{aligned} \tag{6.58}$$

Measurement

In order to verify the analytical expressions above, a measurement campaign was conducted using the same RTS system and configurations as in section 6.6. Four FEs were positioned at a distance of $R_c \approx 1\,\mathrm{m}$ in front of the RuT in a semi-circular formation in the horizontal and a squared formation in the vertical plane. A metal sheet facilitated the placement of the FEs and shielded off most of the unwanted static radar reflections of the background. A photograph of the setup can be seen in Fig. 6.22. The angular positions of the FEs were measured individually with the RuT and are stated in Table 6.3. The RuT was again configured according to the parameters given in Table 6.1 with the exception that this time all $N_{tx} = 3$ transmit antennas with a vertical element spacing of $d_{tx} = \lambda/2$ were used.

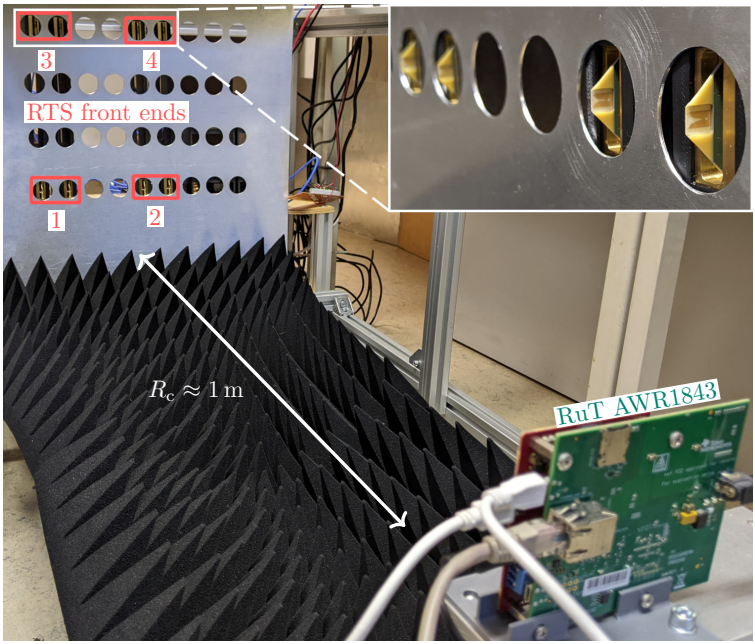

Figure 6.22: Photograph of the two-dimensional arbitrary angle of arrival measurement setup © 2022 IEEE [DNGZ22]

Table 6.3: RTS FE Angular Positions

Front end	Azimuth	Elevation
1	−5.4°	−8.8°
2	4.5°	−7.7°
3	−3.4°	8.4°
4	3.8°	9.9°

As mentioned before, a calibration measurement was executed in order to achieve phase coherency among all RTS channels utilized. The process was similar to the one described in chapter 6.5, but adapted for the usage of four adjacent FEs. First, all channels were calibrated in terms of amplitude and range by performing single measurements with only one FE active at a time. Next, phase coherency was established sequentially in tuples with only two channels active simultaneously. For this, the angle error of the virtual target composed by the two channels was monitored while the delay of one of the channels was swept and the delay of the other was kept constant. The results

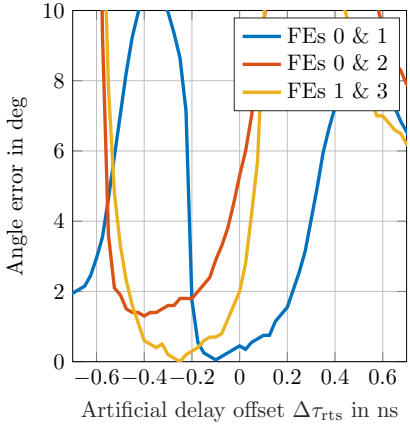

Figure 6.23: Measurement for the the phase calibration with the angle error over the artificial delay offset $\Delta\tau_{\mathrm{rts}}$ for different RTS FE tuples © 2022 IEEE [DNGZ22]

of these measurements are shown in Fig. 6.23, where the angle error is plotted as a function of the simulative delay offset $\Delta\tau_{\mathrm{rts}}$ between the respective FE tuples. Phase coherency is achieved at the point of minimum angular error whose corresponding delay offset is used to calibrate the respective channels for the subsequent AoA measurements.

For the actual two-dimensional arbitrary angle of arrival measurement series, a total of 30 individual measurements comprising of six different azimuth and five different elevation angles were performed. The required RTS channel attenuations were determined according to (6.54) and (6.55). Fig. 6.24 displays the measured and set-point value of the AoA of the superimposed targets, as well as their deviation and the position of the FEs. It can be assumed that the angular errors are caused by the vertical and horizontal misalignment of the FEs and an imperfect phase calibration. Establishing phase coherency among four RTS channels simultaneously presents a challenging task as the calibration process can only be performed metrologically in pairs, which is likely to fall

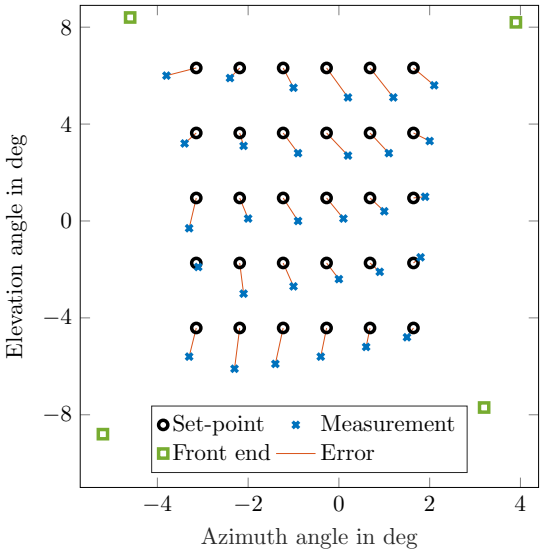

Figure 6.24: Results of the 30 measurements showing the detected and set AoA, as well as their deviations and the angular position of the FEs © 2022 IEEE [DNGZ22]

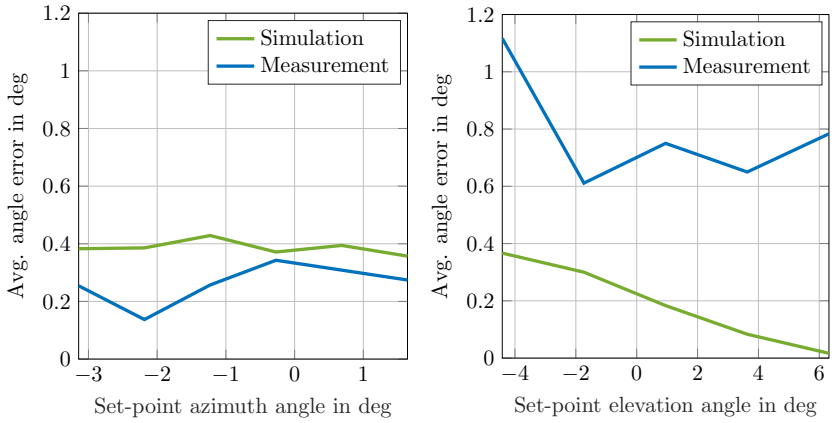

(a) Azimuth average angle error

(b) Elevation average angle error

Figure 6.25: Simulated and measured (a) azimuth and (b) elevation average angle error © 2022 IEEE [DNGZ22]

victim to propagating errors. For the calibration only vertically or horizontally directly adjacent pairs can be selected, since in this either the azimuth or the elevation angle error is evaluated. In addition, the multi-path reflections caused by the mechanical structure can also lead to deviations of the measured angle from its nominal value as has been shown before.

Fig. 6.25 displays the average azimuth and elevation angle errors over the respective set-point angles. The simulated values serve as a reference of the expected error due to the inaccurate vertical and horizontal alignment of the FEs. This misalignment contradicts the simplification constraints made in the calculation of the channel attenuations that are required to create a composed target at the intended AoA. However, the simplifications are necessary to enable an analytically unambiguous solution for the calculation of the channel attenuations, and failure to comply with their assumptions inevitably leads to angular errors. This source of error was also accounted for in the simulation.

The measurement results verify the successful extension of the concept to superimpose the radar echoes of four vertically and horizontally distributed RTS channels in order to create virtual radar targets at arbitrary, two-dimensional AoA in both the azimuth and elevation domain simultaneously. Furthermore,

the results substantiate the necessity for an accurately executed positioning and calibration of the RTS FEs and the corresponding channels.

7 Conclusion

In recent years, the development of autonomous driving has evolved to new levels of sophistication. In order to guarantee proper operation and thus the safety of traffic participants, autonomous driving functions and the radar sensors on which they rely must be validated thoroughly. Since mere software simulations are not able to reliably cover all system and hardware characteristics, and road tests are highly labor-intensive and not reproducible, novel validation paradigms are required.
For these reasons, radar target simulators (RTSs) are on the rise, as they provide testing capabilities to validate radar sensors in-place and under laboratory conditions. They deceive a radar under test (RuT) by creating an artificial environment comprising of virtual radar targets. For this, RTS systems receive, modify and re-transmit the radar signal emitted by the RuT. The simulated range and cross-range of a virtual target can be controlled by applying a delay to the signal and steering its re-transmission angle, respectively.

To fulfill the task of reliably validating autonomous driving functions, RTS systems must be able to create credible, high-precision virtual radar targets at arbitrary positions. The accuracy with which the position of a target can be controlled was so far limited by the delay and angle rasterization, that is, the smallest delay increment and the angular spacing of the front ends (FEs) of the RTS. The concepts presented in this work lift these limitations and enable the generation of high-precision virtual radar targets at an arbitrary, continuous range and cross-range while simultaneously reducing the hardware effort and associated costs. These capabilities are needed in order to deceive modern imaging radar sensors that perceive real-world objects, such as cars and pedestrians, as point clouds of reflections, so that they cannot distinguish between real world and simulated virtual environment.

In the classical approach, the cross-range and thus the angle of arrival (AoA) of a virtual target is simulated by multiplexing the re-transmitted radar signal between lateral distributed FEs, which only allows for targets at discrete angular

positions, inevitably leading to non-negligible deviations between set-point and actual AoA. In this work, a new technique to superimpose the radar echoes of adjacent FEs enables the generation of virtual radar targets at an arbitrary AoA that can be controlled by the amplitude attenuations of the corresponding RTS channels. It helps to reduce the number of FEs and channels required and thereby cuts the hardware cost, while at the same time drastically decreases the angular error and increases the accuracy with which the virtual targets are created. The presented concept overcomes the rasterization and discontinuity limitations and allows to generate artificial complex, multi-reflection traffic scenarios as needed for the validation of autonomous driving functions. It has also been expanded for the application of two-dimensional angle simulation being able to stimulate 4D imaging radars by creating targets that are distributed in both the azimuth and elevation domain simultaneously.

Furthermore, this work enables the analysis of the performance of RTS systems that implement the above technique in regard of their angle simulation capabilities. It provides an estimation of the expected angle error as a function of the FE spacing and RTS channel imbalances in amplitude and phase. A signal model has been developed that grants an in-depth comprehension of the virtual target generation process of RTS systems. It offers guidance in the design cycle of high-precision, angle simulating RTS systems and supports the placement and distribution of the RTS FEs based on the desired angle accuracy and the performance parameters of the utilized RF components. In addition, the model allows to estimate the number of FEs and their spacing required given the RTS channel imbalances and the angular error tolerable. It could be shown that due to the coherent characteristic of the superposition of adjacent radar echoes, the spacing of the FEs may exceed the intuitively assumed limit of the angular resolution of the RuT and still create a superimposed virtual target at an arbitrary AoA. Moreover, a calibration process has been developed that helps to reduce phase and amplitude mismatches among the RTS channels utilizing only a commercial radar sensor and its output. It circumvents the need for a raw data extraction which makes it suitable for the validation of sealed sensors in-place and as-is.

The simulation of the range of a virtual target is controlled by the delay that is applied to the radar signal. In the classical approach, the smallest delay increment determines the rasterization at which the range of a target can be adjusted, and thus the range accuracy of the RTS. It must satisfy not only

the range resolution capability of modern radars, that are on the verge to be improved using greater bandwidths, but also the even finer range accuracy of the sensors. A new technique presented in this work enables a stepless adjustment of the delay so that virtual targets can be created at arbitrary range without the restrictions of a rasterization. This also bears the potential to simulate the movement of virtual targets within the measurement cycle of a RuT allowing to create non-ideal targets that feature realistic characteristics such as range and Doppler migration. This is achieved by using fractional delay filters which enable the continuous, stepless adjustment of the delay applied to the radar signal by controlling the filter coefficients. A signal model was developed that introduces a method to generate virtual targets that exhibit both range and Doppler migration characteristics by solely fine-tuning the simulated range at a specific update rate.

In the course of this work, a digital RTS system has been designed and implemented that enabled the verification and analysis of the techniques mentioned above. It consists of modular front ends that operate in the automotive frequency band of $76 - 81\,\mathrm{GHz}$ and a digital back end based on an FPGA with integrated analog-to-digital (ADCs) and digital-to-analog converters (DACs) on which the superposition of adjacent radar echoes and the fractional delay filters have been realized. With this, the test setup allowed the generation of virtual radar targets at arbitrary lateral and longitudinal positions and with range Doppler migration characteristics. The obtained measurement results are in good agreement with those of the signal models, which verifies not only the applicability of the techniques, but also the estimation capabilities of the models.

Both concepts presented in this work operate independently of the modulation scheme of the RuT employed, as they are both based on true time delay and phase shifting methods that mimic the signal propagation in the real world. They do not require access to raw data and can therefore be implemented for commercially available automotive radar sensors. Moreover, the concepts are not limited in regards of the methodology of the RTS, as they are applicable to both analog and digital systems.

Bibliography

[ABB+21] M. E. Asghar, S. Buddappagari, F. Baumgärtner, S. Graf, F. Kreutz, A. Löffler, J. Nagel, T. Reichmann, R. Stephan, and M. A. Hein. Radar Target Simulator and Antenna Positioner for Real-Time Over-the-air Stimulation of Automotive Radar Systems. In *European Radar Conference (EuRAD)*, pages 95–98, 2021.

[AHHD20] Natalya Ahn, Andreas Höfer, Martin Herrmann, and Christian Donn. Echtzeitfähige Simulation von physikalischen Multi-Sensor-Setups. *ATZelektronik*, 15(6):16–21, Jun 2020.

[ALP+17] F. Arzur, M. Le Roy, A. Pérennec, G. Tanné, and N. Bordais. Hybrid architecture of a compact, low-cost and gain compensated delay line switchable from 1 m to 250 m for automotive radar target simulator. In *2017 European Radar Conference (EURAD)*, pages 239–242, 2017.

[ALRP+17] Fabien Arzur, Marc Le Roy, André Pérennec, Gérad Tanné, and Nicolas Bordais. Hybrid architecture of a compact, low-cost and gain compensated delay line switchable from 1 m to 250 m for automotive radar target simulator. In *2017 European Radar Conference (EURAD)*, pages 239–242, 2017.

[AOHH21] Viktor Adler, Petr Ourednik, Premysl Hudec, and Karel Hoffmann. Broadband Target Simulator for FMCW Radar Sensors With Mirror Target Suppression. In *2021 20th International Conference on Microwave Techniques (COMITE)*, pages 1–5, 2021.

[AVL22] AVL List GmbH. AVL DrivingCube. `https://www.avl.com/documents/10138/3898705/solutionsheet_Driving+Cube_210x279_WEB_R3.pdf`, 2022. Accessed: 2022-08-15.

[BAB+21] S. Buddappagari, M.E. Asghar, F. Baumgärtner, S. Graf, F. Kreutz, A. Löffler, J. Nagel, T. Reichmann, R. Stephan, and

Matthias A. Hein. Over-the-Air Vehicle-in-the-Loop Test System for Installed-Performance Evaluation of Automotive Radar Systems in a Virtual Environment. In *2020 17th European Radar Conference (EuRAD)*, pages 278–281, 2021.

[Bal15] C.A. Balanis. *Antenna Theory: Analysis and Design*. Wiley, 2015.

[Bri74] E.O. Brigham. *The Fast Fourier Transform*. Prentice-Hall signal processing series. Prentice-Hall, 1974.

[BSMM01] I. N. Bronstein, K. A. Semendjajew, G. Musiol, and H. Mühlig. *Taschenbuch der Mathematik*. Harri Deutsch, Frankfurt am Main, 2001.

[Con21] Continental Automotive. Advanced Radar Sensor ARS540. `https://www.continental-automotive.com/en-gl/Passenger-Cars/Autonomous-Mobility/Enablers/Radars/Long-Range-Radar/ARS540`, 2021. Accessed: 2022-03-24.

[DAN+21] Axel Diewald, Theresa Antes, Benjamin Nuss, Mario Pauli, and Thomas Zwick. Range Doppler Migration Synthesis for Realistic Radar Target Simulation. In *IEEE Topical Conference Wireless Sensors and Sensor Networks (WiSNeT)*, pages 56–58, 2021.

[DANZ21] Axel Diewald, Theresa Antes, Benjamin Nuss, and Thomas Zwick. Implementation of Range Doppler Migration Synthesis for Radar Target Simulation. In *2021 IEEE 93rd Vehicular Technology Conference (VTC2021-Spring)*, 2021.

[DCD11] Javier Diaz-Carmona and Gordana Jovanovic Dolecek. Fractional Delay Digital Filters. In *Applications of MATLAB in Science and Engineering*. IntechOpen, 2011.

[dDP09] Florent de Dinechin and Bogdan Pasca. Large multipliers with fewer DSP blocks. In *2009 International Conference on Field Programmable Logic and Applications*, pages 250–255, 2009.

[DF03] D.S. Dummit and R.M. Foote. *Abstract Algebra*. Wiley, 2003.

[DKK+21] Axel Diewald, Clemens Kurz, Prasanna Venkatesan Kannan, Martin Gießler, Mario Pauli, Benjamin Göttel, Thorsten Kayser, Frank Gauterin, and Thomas Zwick. Radar Target Simulation for Vehicle-in-the-Loop Testing. *Vehicles*, 3(2):257–271, 2021.

[DMW18] Thomas Dallmann, Jens-Kristian Mende, and Stefan Wald. ATRIUM: A Radar Target Simulator for Complex Traffic Scenarios. In *2018 IEEE MTT-S International Conference on Microwaves for Intelligent Mobility (ICMIM)*, pages 1–4, 2018.

[DNGZ22] Axel Diewald, Benjamin Nuss, Johannes Galinsky, and Thomas Zwick. Two-Dimensional Arbitrary Angle of Arrival in Radar Target Simulation. In *International Radar Symposium (IRS)*, pages 25–29, 2022.

[DNPZ22] Axel Diewald, Benjamin Nuss, Mario Pauli, and Thomas Zwick. Arbitrary Angle of Arrival in Radar Target Simulation. *IEEE Transactions on Microwave Theory and Techniques*, 70(1):513–520, 2022.

[DNZ22] Axel Diewald, Benjamin Nuss, and Thomas Zwick. Quasi-Monostatic Antenna Displacement in Radar Target Simulation. In *European Radar Conference (EuRAD)*, pages 385–388, 2022.

[dSP20] dSPACE GmbH. DARTS 9040-G, The First True 5 GHz Bandwidth Radar Target Simulator. `https://www.dspace.com/shared/data/pdf/2020/DARTS_9040-G_Product_information_201002_E.pdf`, 2020. Accessed: 2022-07-26.

[dSP21] dSPACE GmbH. Radar Test Bench – Compact 3D. `https://www.dspace.com/shared/data/pdf/2021/dSPACE-Radar-Testbench-Compact-3D_TwoPager_2021-12_E.pdf`, 2021. Accessed: 2022-07-26.

[dSP22] dSPACE GmbH. End-of-Line Test System for Radar Sensors. `https://www.dspace.com/en/pub/home/products/hw/darts/eol_catr_system.cfm`, 2022. Accessed: 2022-04-16.

[DWCP21] Dean Deter, Chieh Wang, Adian Cook, and Nolan Kyle Perry. Simulating the Autonomous Future: A Look at Virtual Vehicle Environments and How to Validate Simulation Using Public Data Sets. *IEEE Signal Processing Magazine*, 38(1):111–121, 2021.

[EPB16] M. Engelhardt, F. Pfeiffer, and E. Biebl. A high bandwidth radar target simulator for automotive radar sensors. In *2016 European Radar Conference (EuRAD)*, pages 245–248, 2016.

[Eur08] European Telecommunications Standards Institute. *Short Range Radar equipment operating in the 77 GHz to 81 GHz band*, 2008.

[FFFG20] Nicolas Fraikin, Kilian Funk, Michael Frey, and Frank Gauterin. Efficient Simulation Based Calibration of Automated Driving Functions Based on Sensitivity Based Optimization. *IEEE Open Journal of Intelligent Transportation Systems*, 1:63–79, 2020.

[FKJ+19] András Fábián, Krisztián Kovács, Szabolcs Jánky, Christian Gutenkunst, and Aakash Sehgal. Testing Method for ADAS/AD Systems using an Open and Consistent Toolchain. Technical report, AImotive and AVL Deutschland GmbH, 2019.

[Gö11] Jürgen Göbel. *Radartechnik : Grundlagen und Anwendungen*. VDE-Verlag, Berlin, 2011.

[GdONA+22] Lucas Giroto de Oliveira, Benjamin Nuss, Mohamad Basim Alabd, Axel Diewald, Mario Pauli, and Thomas Zwick. Joint Radar-Communication Systems: Modulation Schemes and System Design. *IEEE Transactions on Microwave Theory and Techniques*, 70(3):1521–1551, 2022.

[GGS+17] A. Gruber, M. Gadringer, H. Schreiber, D. Amschl, W. Bösch, S. Metzner, and H. Pflügl. Highly scalable radar target simulator for autonomous driving test beds. In *European Radar Conference (EuRAD)*, pages 147–150, 2017.

[GMS+18] M. E. Gadringer, F. M. Maier, H. Schreiber, V. P. Makkapati, A. Gruber, M. Vorderderfler, D. Amschl, S. Metzner, H. Pflügl, W. Bösch, M. Horn, and M. Paulweber. Radar target stimulation for automotive applications. *IET Radar, Sonar Navigation*, 12(10):1096–1103, 2018.

[GR17] S. Graf and M. Rožmann. OTA radar test for autonomous driving based on a 77 GHz radar signal simulator. In *European Radar Conference (EuRAD), Workshop: Automotive Radar Measurement Solutions*, pages 1–19, 2017.

[GSG+18] M. Gadringer, H. Schreiber, A. Gruber, M. Vorderderfler, D. Amschl, W. Bösch, S. Metzner, H. Pflügl, and M. Paulweber. Virtual reality for automotive radars. *e & i Elektrotechnik und Informationstechnik*, 135, 06 2018.

[Har14] Marlene Harter. *Dreidimensional bildgebendes Radarsystem mit digitaler Strahlformung für industrielle Anwendungen*. Karl-

sruher Forschungsberichte aus dem Institut für Hochfrequenztechnik und Elektronik ; Band 75. KIT Scientific Publishing, Karlsruhe, 2014.

[Hec12] E. Hecht. *Optics*. Pearson, New York, 2012.

[Hol74] Melvin G. Holland. Surface acoustic wave phase control device, Oct 1974. US Patent 3845420A.

[HTS+12] J. Hasch, E. Topak, R. Schnabel, T. Zwick, R. Weigel, and C. Waldschmidt. Millimeter-Wave Technology for Automotive Radar Sensors in the 77 GHz Frequency Band. *IEEE Transactions on Microwave Theory and Techniques*, 60(3):845–860, 2012.

[IMSW19] Johannes Iberle, Marc. A. Mutschler, Philipp A. Scharf, and Thomas Walter. A Radar Target Simulator for Generating Micro-Doppler-Signatures of Vulnerable Road Users. In *2019 16th European Radar Conference (EuRAD)*, pages 17–20, 2019.

[IRW20] Johannes Iberle, Patrick Rippl, and Thomas Walter. A Near-Range Radar Target Simulator for Automotive Radar Generating Targets of Vulnerable Road Users. *IEEE Microwave and Wireless Components Letters*, 30(12):1213–1216, 2020.

[IRW21] Johannes Iberle, Patrick Rippl, and Thomas Walter. A Radar Target Simulator for Generating Synthesised and Measured micro-Doppler-Signatures of Vulnerable Road Users. In *2020 17th European Radar Conference (EuRAD)*, pages 218–221, 2021.

[JLH21] Jun Jiang, Fu Liu, and Cong Hu. Design and Realization of FPGA-based DRFM with High Instantaneous Bandwidth. In *2021 IEEE 15th International Conference on Electronic Measurement & Instruments (ICEMI)*, pages 233–239, 2021.

[KBS+22] Georg Körner, Christoph Birkenhauer, Patrick Stief, Christian Carlowitz, and Martin Vossiek. Frequency Extension Method for Multirate Radar Target Simulation Systems. In *2022 14th German Microwave Conference (GeMiC)*, pages 116–119, 2022.

[KEY] KEYCOM Corp. Active Radar Target Simulator for Collision Avoidance Radar (long range). `http://www.keycom.co.jp/eproducts/rat/rat11/page.html`. Accessed: 2021-07-01.

[Key17] Keysight Technologies. E8707A Radar Target Simulator 76 GHz to 77 GHz. `https://www.keysight.com/us/en/assets/`

7018-05310/brochures/5992-1648.pdf, 2017. Accessed: 2022-07-26.

[Key22] Keysight Technologies. Radar Scene Emulator. https://www.keysight.com/de/de/assets/7121-1260/data-sheets/Radar-Scene-Emulator.pdf, 2022. Accessed: 2022-07-26.

[KHN+21] Georg Körner, Marcel Hoffmann, Steffen Neidhardt, Matthias Beer, Christian Carlowitz, and Martin Vossiek. Multirate Universal Radar Target Simulator for an Accurate Moving Target Simulation. *IEEE Transactions on Microwave Theory and Techniques*, 69(5):2730–2740, 2021.

[Kön13] K. Königsberger. *Analysis 1*. Springer-Lehrbuch. Springer Berlin Heidelberg, 2013.

[Kon17a] Konrad Technologies. A Test Solution for ADAS Virtual Test Drive. https://www.konrad-technologies.com/en/products/software/konrad-automotive-radar-test-system.html, 2017. Accessed: 2022-07-26.

[Kon17b] Konrad Technologies. ADAS Automotive Radar Target Simulator. https://www.konrad-technologies.com/files/konrad/media/datasheet/2021/KT_ADAS_Automotive%20Radar_Target%20Simulator.pdf, 2017. Accessed: 2022-07-26.

[Kon21] Konrad Technologies. Automotive Radar Production Test System (KT-RPTS). https://www.konrad-technologies.com/en/expertise-and-innovation/technologies/adas-test-solutions/sensor-production-test.html, 2021. Accessed: 2022-04-16.

[KP16] Nidhi Kalra and Susan M. Paddock. Driving to safety: How many miles of driving would it take to demonstrate autonomous vehicle reliability? *Transportation Research Part A: Policy and Practice*, 94:182–193, 2016.

[KW16] P. Koopman and M. Wagner. Challenges in Autonomous Vehicle Testing and Validation. *SAE International Journal of Transportation Safety*, pages 15–24, 2016.

[LEWW14] S. Lutz, C. Erhart, T. Walte, and R. Weigel. Target simulator concept for chirp modulated 77 GHz automotive radar sensors.

In *2014 11th European Radar Conference (EuRAD)*, pages 65–68, 2014.

[LS09] J. Li and P. Stoica. *MIMO Radar Signal Processing*. IEEE Press. Wiley, 2009.

[Lud13] A.K. Ludloff. *Praxiswissen Radar und Radarsignalverarbeitung*. Vieweg+Teubner Verlag, 2013.

[MGLW15] M. Maurer, J.C. Gerdes, B. Lenz, and H. Winner. *Autonomes Fahren - Technische, rechtliche und gesellschaftliche Aspekte*. Springer Vieweg, Wiesbaden, 2015.

[MRP07] D Meena, Taniza Roy, and LGM Prakasam. Design of Multilevel Radar Target Simulator. In *2007 IEEE Radar Conference*, pages 203–208, 2007.

[NHK19] Herman Jalli Ng, Raqibul Hasan, and Dietmar Kissinger. A Scalable Four-Channel Frequency-Division Multiplexing MIMO Radar Utilizing Single-Sideband Delta–Sigma Modulation. *IEEE Transactions on Microwave Theory and Techniques*, 67(11):4578–4590, 2019.

[Nus21] Benjamin Nuss. *Frequenzkamm-basiertes breitbandiges MIMO-OFDM-Radar*. Karlsruher Institut für Technologie (KIT) - KIT-Bibliothek, Karlsruhe, 2021.

[NXP20] NXP Semiconductors. *TEF82xx 77 GHz Automotive Radar Transceiver*, November 2020. Rev. 0.

[Pan21] Panasonic. High speed material for millimeter wave radar - Laminate R-5515. `https://industrial.panasonic.com/content/data/EM/PDF/ipcdatasheet_R-5515.pdf`, 2021. Accessed: 2022-07-01.

[PDF99] R.P. Perry, R.C. DiPietro, and R.L. Fante. SAR imaging of moving targets. *IEEE Transactions on Aerospace and Electronic Systems*, 1999.

[PL15] Fernando Puente León. *Messtechnik : Systemtheorie für Ingenieure und Informatiker*. Springer Vieweg, 10. Aufl. 2015 edition, 2015.

[RH20] Fahimeh Rafieinia and Kasra Haghighi. ASGARDI: A Novel Frequency-based Automotive Radar Target Simulator. In *2020 IEEE MTT-S International Conference on Microwaves for Intelligent Mobility (ICMIM)*, pages 1–4, 2020.

[RISW22] Patrick Rippl, Johannes Iberle, Philipp A. Scharf, and Thomas Walter. Radar Scenario Generation for Automotive Applications in the E Band. *IEEE Journal of Microwaves*, 2(2):253–261, 2022.

[Rob21] Robert Bosch GmbH. Front radar. https://www.bosch-mobility-solutions.com/media/global/products-and-services/passenger-cars-and-light-commercial-vehicles/driver-assistance-systems/multi-camera-system/front-radar-plus/onepager_front-radar_en_200608.pdf, 2021. Accessed: 2022-03-24.

[Rob22] Robert Bosch GmbH. Front radar premium. https://www.bosch-mobility-solutions.com/media/global/products-and-services/passenger-cars-and-light-commercial-vehicles/driver-assistance-systems/multi-camera-system/front-radar-plus/onepager_front-radar_en-premium.pdf, 2022. Accessed: 2022-08-08.

[Roh21a] Rohde & Schwarz. Better than real life: radar echoes from a target simulator. https://cdn.rohde-schwarz.com/pws/dl_downloads/dl_common_library/dl_news_from_rs/213/NEWS_213_ARTS9510_english.pdf, 2021. Accessed: 2022-04-16.

[Roh21b] Rohde & Schwarz. R&S AREG800A: Automotive Radar Echo Generator. https://scdn.rohde-schwarz.com/ur/pws/dl_downloads/pdm/cl_brochures_and_datasheets/specifications/3609_8015_22/AREG800A_dat-sw_en_3609-8015-22_v0400.pdf, 2021. Accessed: 2022-07-26.

[Roh22] Rohde & Schwarz. R&S QAT100 Adavanced Antenna Array. https://scdn.rohde-schwarz.com/ur/pws/dl_downloads/dl_common_library/dl_brochures_and_datasheets/pdf_1/QAT_dat-sw_en_3609-5380-22_v0301.pdf, 2022. Accessed: 2022-04-16.

[Ros16] Pawel Roszkowski. Carrier- and Doppler-tunable FPGA-based active reflector for radar calibration. In *2016 17th International Radar Symposium (IRS)*, pages 1–6, 2016.

[RSSH10] M.A. Richards, J.A. Scheer, J. Scheer, and W.A. Holm. *Principles of Modern Radar: Basic Principles, Volume 1*. Electromagnetics and Radar. Institution of Engineering and Technology, 2010.

[Sch17a] S. Scherr. *FMCW-Radarsignalverarbeitung zur Entfernungsmessung mit hoher Genauigkeit*. Karlsruher Forschungsberichte aus dem Institut für Hochfrequenztechnik und Elektronik; Band 83. KIT Scientific Publishing, Karlsruhe, 2017.

[Sch17b] S. Schneider. How to Measure/Calculate Radar System MTBF? In *Europ. Microw. Conf. (EuMC)*, 2017.

[Sei21] Seiger, Caius. Digitaler Zwilling. `https://www.dspace.com/shared/data/pdf/2021/dSPACE-Magazin-2021-01_SRS_Digitaler_Zwilling_210507_D.pdf`, 2021. Accessed: 2022-08-15.

[SGR+21] Benedikt Schweizer, Alexander Grathwohl, Gilberto Rossi, Philipp Hinz, Christina Knill, Simon Stephany, Herman Jalli Ng, and Christian Waldschmidt. The Fairy Tale of Simple All-Digital Radars: How to Deal With 100 Gbit/s of a Digital Millimeter-Wave MIMO Radar on an FPGA [Application Notes]. *IEEE Microwave Magazine*, 22(7):66–76, 2021.

[Sha84] C.E. Shannon. Communication in the presence of noise. *Proceedings of the IEEE*, 1984.

[Sit17] Yoke Leen Sit. *MIMO OFDM radar-communication system with mutual interference cancellation*. Karlsruher Forschungsberichte aus dem Institut für Hochfrequenztechnik und Elektronik ; Band 82. KIT Scientific Publishing, Karlsruhe, 2017.

[SJM+21] Pirmin Schoeder, Vinzenz Janoudi, Benedikt Meinecke, David Werbunat, and Christian Waldschmidt. Flexible Direction-of-Arrival Simulation for Automotive Radar Target Simulators. *IEEE Journal of Microwaves*, 1(4):930–940, 2021.

[Sko90] Merrill I. Skolnik, editor. *Radar handbook*. McGraw Hill reference books of interestElectronics electrical engineering. McGraw-Hill, New York, 2. ed. edition, 1990.

[Smi10] Julius O. Smith. *Physical Audio Signal Processing*. W3K Publishing, 2010.

[SN20] Jan Sobotka and Jiri Novak. Digital Vehicle Radar Sensor Target Simulation. In *2020 IEEE International Instrumentation and Measurement Technology Conference (I2MTC)*, 2020.

[SP21] Andrey V. Smolyakov and Alexey S. Podstrigaev. Design of DRFM-based Several Radar Targets Simulator Using FPGA. In *2021 IEEE Conference of Russian Young Researchers in Electrical and Electronic Engineering (ElConRus)*, pages 1694–1699, 2021.

[SRGD21] Christoph Stadler, Kevin Rauner, Reinhard German, and Anatoli Djanatliev. Simulation-Based Parameter Identification for Accuracy Definitions in Virtual Environment Models for Validation of Automated Driving. In *2021 IEEE Intelligent Vehicles Symposium (IV)*, pages 1138–1143, 2021.

[SSGW21] Pirmin Schoeder, Benedikt Schweizer, Alexander Grathwohl, and Christian Waldschmidt. Multitarget Simulator for Automotive Radar Sensors With Unknown Chirp-Sequence Modulation. *IEEE Microwave and Wireless Components Letters*, 31(9):1086–1089, 2021.

[Sys21] System Plus Consulting. Automotive Radar Comparison 2021 - Detailed analysis of technologies and cost of the main radar systems and their chipsets, including radar from Continental, Bosch, Denso, and others. `https://s3.i-micronews.com/uploads/2021/10/SPR21529-Automotive-Radar-Comparison-2021-Sample.pdf`, 2021. Accessed: 2022-08-15.

[TMH+03] Guan-Leng Tan, R.E. Mihailovich, J.B. Hacker, J.F. DeNatale, and G.M. Rebeiz. Low-loss 2- and 4-bit TTD MEMS phase shifters based on SP4T switches. *IEEE Transactions on Microwave Theory and Techniques*, 51(1):297–304, 2003.

[VGS+21] Michael Vorderderfler, Michael E. Gadringer, Helmut Schreiber, Wolfgang Bösch, and Herman Jalli Ng. Generating synthetic radar targets using azimuthal distributed scatterer for automotive applications. In *2021 IEEE International Workshop on Metrology for Automotive (MetroAutomotive)*, 2021.

[Way11] David Wayne. RF Target and Decoy Simulator. Technical report, MI Technologies, 2011.

[Whi15] E. T. Whittaker. XVIII.—On the Functions which are represented by the Expansions of the Interpolation-Theory, January 1915.

[WHLS19] Hermann Winner, Stephan Hakuli, Felix Lotz, and Christina Singer, editors. *Handbook of Driver Assistance Systems : Basic Information, Components and Systems for Active Safety and Comfort*. Springer Nature Living ReferenceSpringer eBook Collection. Springer, Cham, 2019.

[WMN+20] Stefan Wald, Torsten Mathy, Sreejith Nair, Carlos Moreno Leon, and Thomas Dallmann. ATRIUM: Test Environment for Automotive Radars. In *2020 IEEE MTT-S International Conference on Microwaves for Intelligent Mobility (ICMIM)*, pages 1–4, 2020.

[Woo53] P.M. Woodward. *Probability and Information Theory: With Applications to Radar*. Number Bd. 3 in International series of monographs on electronics and instrumentation. McGraw-Hill, 1953.

[WS14] Werner Wiesbeck and Leen Sit. Radar 2020: The future of radar systems. In *2014 International Radar Conference*, pages 1–6, 2014.

[XBP19] Zhihuo Xu, Chris J. Baker, and Sukhjit Pooni. Range and Doppler Cell Migration in Wideband Automotive Radar. *IEEE Transactions on Vehicular Technology*, 2019.

[Xil18] Xilinx, Inc. ZCU111 Evaluation Board. `https://www.xilinx.com/content/dam/xilinx/support/documents/boards_and_kits/zcu111/ug1271-zcu111-eval-bd.pdf`, 2018. Accessed: 2022-07-01.

[Xil22] Xilinx, Inc. UltraFast Design Methodology Guide for Xilinx FPGAs and SoCs. `https://docs.xilinx.com/viewer/book-attachment/Yoc5d1VaPFc9I9aESP_z9Q/8oqHBiylo6atAHn~CkV7GQ`, 2022. Accessed: 2022-07-19.